Studies of Interstellar Matter on Scales from 10 AU to 10 kpc

Keith Thomas Smith

Thesis submitted to
The University of Nottingham

for the degree of
Doctor of Philosophy

June 2010

Abstract

This thesis presents four optical spectroscopic studies of absorption by matter in the diffuse interstellar medium on scales ranging from 10 AU to 10 kpc. The observations investigate two current problems in interstellar medium (ISM) research: small-scale structure (SSS), and the diffuse interstellar bands (DIBs).

Very high spectral resolution observations of interstellar Na I, Ca I, Ca II, K I and CH absorption towards κ Vel are presented. Combined with observations over the last 15 years taken from the literature, the small-scale structure in front of this star is probed on scales of ∼10 AU. The high resolution and signal-to-noise of the new observations allow detailed modelling of the absorption profiles and the identification of multiple absorption components. For the two narrowest components, the line profile models are used to constrain the temperature, depletion, electron density and total number density within the structures.

Diffuse interstellar bands are used as probes of SSS in long-slit observations of lines-of-sight towards three binary/multiple star systems: HD 168075/6, HD 176269/70 and four members of the μ Sgr system, one of which is identified as a member for the first time. The results show clear variations in DIB absorption in the HD 168075/6 and μ Sgr systems over scales of ∼50,000–200,000 AU, and demonstrate the efficacy of medium-resolution observations of DIBs for identification of small-scale structure in the ISM. Multi-object spectroscopy of 452 stars in the ω Cen globular cluster is also presented, which probes interstellar absorption by Na I, Ca II and DIBs in two dimensions, on scales of ∼1 pc.

The first detections of diffuse interstellar bands in the M33 galaxy are reported. Multi-object spectroscopy of 43 stars is used to derive spectral types and reddenings, and measure DIB absorption across the disk of the galaxy (∼10 kpc). Very strong DIB absorption per unit $E_{(B-V)}$ is found for one star in the sample, towards which a total of seven DIBs are detected.

It is vital to remember that information – in the sense of raw data – is not knowledge, that knowledge is not wisdom, and that wisdom is not foresight. But information is the first essential step to all of these.

Arthur C. Clarke

Acknowledgements

Thanks first of all to my supervisor, Professor Peter J. Sarre, for his enthusiasm, guidance, scientific acumen and for introducing me to the problem of the diffuse interstellar bands. This research would have been impossible without the knowledge and advice of my collaborators, amongst whom Martin Cordiner, Steve Fossey and Jacco van Loon deserve special mention. Thanks to all those who have shared telescope domes with me, and particularly to Tom Lloyd Evans for imparting some of his vast experience of practical observing. Els van Aarle has shown me the way forwards, for which I am eternally grateful.

My fellow denizens of A41 – Ale Candian, Markus Hammonds and Amit Pathak – have provided invaluable advice and second opinions. Thanks too to Arfon Smith for getting me up and running with Linux and IRAF. I have thoroughly enjoyed discussions on all things astronomical with the various members of the Astronomy group – who are too numerous to name – particularly those accompanied by coffee and cake! The Photoelectron Spectroscopy group kindly adopted me in my first year and helped make tea breaks last far too long. My thanks to Marianne Baker for helping to keep me sane. My parents, family and friends have all provided much appreciated moral support.

This research has been made possible by a Doctoral Training Grant from the Engineering and Physical Sciences Research Council. The University of Nottingham provided funds for my time at SALT through the award of a Business Engineering and Science Travel Scholarship. Funding for conferences and visits was provided by The University of Nottingham, the Astrophysical Chemistry Group and the Faculty of the European Space Astronomy Centre. My thesis examiners – Omar Almaini and Serena Viti – made numerous suggestions which have improved the quality of this thesis. Finally, my life has been made immeasurably easier by the utterly indispensable NASA ADS and CDS SIMBAD & VizieR databases.

Declaration

The candidate hereby declares that the work presented in this thesis is entirely their own, and was performed whilst enrolled as a PhD student at The University of Nottingham, with the following exceptions:

- Where results have been obtained by analysis of observations performed by others, those persons are identified in the text.
- Figure 4.31 and the backgrounds of figures 4.1 & 4.2 were produced by the European Southern Observatory, and are reproduced under license.
- The research presented in section 4.2 was conducted as part of a collaborative project. Data reduction and analysis were performed by J van Loon (Keele); the candidate contributed to the interpretation of the results, along with the other co-authors of van Loon et al. (2009). Figures 4.32 and 4.33 were kindly provided by J van Loon.
- In chapter 5, stellar classifications were performed by C Evans (UK ATC), with the exception of star 19 which was classified by the candidate. Figure 5.3 was kindly provided by M Cordiner (NASA GSFC), who also measured the equivalent widths of the $\lambda\lambda$5705, 5797, 6196, 6203, 6269, 6283 and 6613 DIBs towards star 31. All other measurements were performed by the candidate.

Contents

Chapter 1

Introduction

Mankind has an endless fascination with the night sky – the motions of the stars have been recorded for at least 5,000 years*. The simple pleasure of staring up at the stars from dark sites (which are sadly disappearing from many countries) has captivated billions of people, whilst astronomical discoveries are regularly featured in the media. The intellectual and social impacts have been immense: challenging our ideas of how we fit into the universe, driving technological innovation and inspiring generations of scientists.

Great advances in astronomy became possible in 1609 when Thomas Harriot and Galileo Galilei independently turned the newly-invented telescope towards the heavens and discovered a wealth of detail invisible to the naked eye†. The resulting studies led to a scientific revolution. In 1687 Isaac Newton published his *Principia Mathematica*, which contained the key observation that "the force by which the moon is retained in its orbit is that very same force which we commonly call gravity" (Newton 1687, Book III). Thus it was realised that objects in the heavens are governed by the same scientific laws as those on Earth.

A second revolution in astronomy occurred in 1814 when Fraunhofer used a prism to disperse sunlight, and noted the presence of dark bands in the resulting spectrum. When combined with Kirchoff's realisation that these lines were caused by the presence of chemical species in the surface of the Sun, it then became possible to determine the composition of the stars. Spectroscopy rapidly became the most powerful observa-

*The oldest known archaeo-astronomical site is the tomb at Newgrange, Ireland, which dates from c. 3,000 BC (Ray 1989).

†In celebration of the 400$^{\text{th}}$ anniversary of these events, the United Nations declared 2009 to be the International Year of Astronomy.

tional technique available to astronomers, and remains so to this day (for a history of astronomical spectroscopy, see Hearnshaw 1986).

At first glance, it may be difficult to believe that much chemistry occurs in space. Stars are extremely hot balls of plasma, within which not even atoms survive intact. The voids between the stars are either similarly hot and bombarded by ultraviolet light, or extremely cold and dark; in both cases the density is so low that particles' mean-free-paths are hundreds of kilometres or more. It is difficult to see how conventional chemistry can occur in these situations. Nevertheless, simple hydrides and oxides have been observed in the atmospheres of cool stars and over 100 molecules have been identified in the interstellar medium*.

1.1 The interstellar medium

The space between the stars is not empty – it is pervaded by the 'interstellar medium' (ISM), which is a tenuous collection of material which exists throughout the Milky Way and other galaxies†, making up 5–10% of their (baryonic) mass (Lequeux 2005). The ISM consists of gas, plasma and 'dust', which is an ensemble of silicate and carbonaceous grains. By mass, dust makes up about 1% of the ISM, with the vast majority of material in the gas phase.

1.1.1 The cosmic matter cycle

According to the current cosmological understanding, the universe began with the Big Bang some 13.7 billion years ago (Hinshaw et al. 2009). The extremely hot and dense universe then began to expand and cool, a process which continues to this day. After about one second, the universe had cooled sufficiently for protons and neutrons to form. Over the next three minutes these combined via nuclear fusion to form various chemical elements in a process known as 'Big Bang nucleosynthesis', until the universe cooled to the point where nuclear fusion was no longer possible. The nuclear physics behind this process is well understood, and predicts that nuclei should form in the proportion of 75% ${}^{1}_{1}\mathrm{H}$ and 25% ${}^{4}_{2}\mathrm{He}$ by mass, with trace amounts of ${}^{2}_{1}\mathrm{D}$, ${}^{3}_{1}\mathrm{T}$ (which then decays with a half-life of 12 years), ${}^{3}_{2}\mathrm{He}$ and ${}^{7}_{3}\mathrm{Li}$, the predicted abundances of which are all in

*Databases of molecules which have been detected in the interstellar medium are maintained at `www.astrochymist.org/astrochymist_ism` and `www.astrochemistry.net`

†The material which exists *between* galaxies is termed the 'intergalactic medium' (IGM).

agreement with current observations. No heavier elements are formed in the process due to the absence of stable nuclei with 5 or 8 nucleons, and the short time period during which nucleosynthesis occurred (for an introduction to Big Bang nucleosynthesis, see Burles et al. 2001, and references therein).

Three hundred thousand years later, the universe had cooled sufficiently for these light nuclei to combine with electrons to form atoms, during a period confusingly named the 'era of recombination'. As matter began to dominate the universe, the force of gravity began to take over, amplifying small variations in density caused by quantum fluctuations in the early universe. These overdensities grew until the temperature and pressure of the gas reached sufficient levels to restart fusion, and the first stars were born (Bromm and Larson 2004).

Stars are powered by the energy released by nuclear fusion in their cores, which provides both support against the great weight of the star and heats the star to the point where it shines. Most stars (those on the 'main sequence') are powered by the fusion of hydrogen to form helium. However, towards the ends of their lives all but the lightest stars begin to produce heavier elements; the more massive the star, the heavier the elements eventually produced, up to the limit of iron beyond which nucleosynthesis becomes endothermic. Much of this material, now enriched with heavy elements, is then lost from the star and ejected into the ISM by a variety of processes – stellar winds, supernova explosions of massive stars, and the formation of protoplanetary and planetary nebulae from less massive stars (Tielens 2005, chapter 1).

In this way the ISM was gradually enriched with metals*, from which a new generation of stars could be formed. The additional elements allowed the formation of molecules in the ISM, giving rise to new cooling pathways (see section 1.1.2.1) which profoundly altered the process of star formation. After sufficient enrichment, the quantity of metals is high enough that planets may form around the new generation of stars. The molecules existing in the ISM from which the planets formed, together with those which form on the surface of the planets, provide the building blocks from which life may evolve.

The ISM therefore performs a key role in the universe, providing the raw materials from which all astronomical objects are formed. The cosmic matter cycle is summarised in figure 1.1. Understanding the composition, structure and evolution of the ISM is vital to any complete understanding of the universe and our place within it.

*In astronomical parlance, all elements other than hydrogen and helium are referred to as 'metals', and the relative proportion of heavy elements to H and He is termed the 'metallicity'.

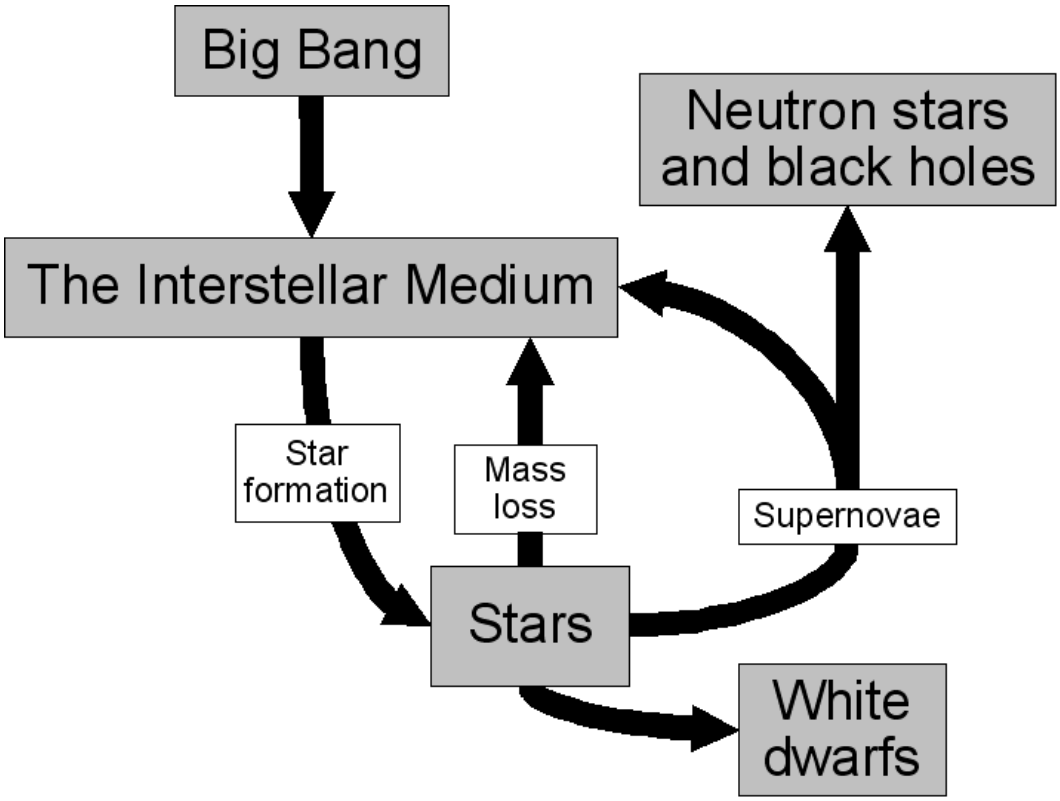

Figure 1.1 – Summary of the cosmic matter cycle. The matter created during the Big Bang is converted into stars, which return material to the ISM at the ends of their lives. In the process, the metallicity of the ISM is gradually enhanced.

1.1.2 Phases of the ISM

The most basic properties of the ISM are its composition, temperature and density. The composition depends on a complex interplay of Big Bang nucleosynthesis, stellar feedback, condensation of dust grains (see section 1.1.3.1) and numerous other factors. On the other hand, the temperature and density are sufficiently simple properties that their behaviour can be modelled analytically. McKee and Ostriker (1977) extended the earlier model of Field et al. (1969) to develop a simple 'three-phase' model of the ISM which describes many of the observed properties. In their model (described in section 1.1.2.2), the ISM consists of matter in three distinct 'phases', governed by the balance between heating and cooling processes.

1.1.2.1 Heating and cooling processes

Heating in the ISM is driven by the energy input from starlight, particularly UV photons produced by the most massive stars, and by energy deposited by cosmic rays. Cosmic

rays are high energy particles, mostly protons and alpha particles, which have been accelerated to relativistic energies. At relatively low energies, most cosmic rays are generated as part of stellar winds. Precisely which processes produce the high-energy cosmic rays is not well understood, but they are thought to include acceleration by strong electromagnetic fields present in supernova remnants, active galactic nuclei and other extreme astrophysical objects.

As they pass through the ISM, cosmic rays collide with the atoms and molecules they encounter, ionising these species and ejecting an electron. A single cosmic ray can interact many times, depositing a small fraction of its energy into the ISM at each step. The electrons ejected during the ionisation then collide with other particles in the ISM before combining with a cation, thermalising the energy and raising the local temperature. UV photons interact with gas-phase species in much the same manner, although each photon is capable of ionising far fewer atoms or molecules (UV photons have energies of $\lesssim 20\,\mathrm{eV}$, whilst cosmic rays may have energies of many MeV).

The ISM cools by the emission of radiation, which carries energy away through space. Whilst grains may cool through black-body radiation, in the gas phase the dominant cooling mechanisms are through line emission. An atom or molecule can become excited through collisions in the gas phase; it may subsequently relax through the emission of a photon. Provided that the photon is not quickly re-absorbed close to the site of emission, energy is carried away and the gas is cooled. How quickly cooling may occur is set by the availability of species with possible emission from excited states which may easily be accessed in collisions, i.e. the excitation energy is not much greater than the energy available in collisions, which depends on the kinetic temperature.

In ionised regions, cooling is dominated by forbidden transitions of atoms, particularly oxygen, nitrogen, and sulphur. In diffuse clouds, the dominant cooling mechanisms are via fine structure lines of atoms, particularly the 158 μm line of C II. In denser molecular clouds, the formation of molecules allows cooling via vibrational and rotational lines in the infrared and radio. For more detailed treatments of heating and cooling processes in the ISM, see Tielens (2005, chapters 2 & 3) and Lequeux (2005, chapter 8).

1.1.2.2 The three-phase model

Analytical examination of the heating and cooling curves of the ISM shows that at the pressures typically encountered in the ISM, there are two possible stable states with the

same pressure (Field et al. 1969, see Wolfire et al. 1995 for a treatment with updated heating and cooling processes). The two states consist of one at high temperature but low density ($\sim 8{,}000$ K, $\sim 2.5\times10^{-3}$ cm^{-3}) and another at low temperature and relatively high density (~ 80 K, ~ 40 cm^{-3}). These two 'phases' can then exist in equilibrium with each other, with the relative proportion of ISM in each phase dependent on the overall density and pressure in any particular region of space. Cool dense material tends to form discrete structures, whereas the warmer phase tends to fill space (Cox 2005).

McKee and Ostriker (1977) introduced a third phase into their model, which consists of superheated gas at $\gtrsim 10^6$ K, which has been raised away from equilibrium by localised heating from hot stars and supernovae. This phase is at a much higher pressure and expands into the surrounding medium, forming bubbles of low density material. The Sun is currently passing through such a region, called the Local Bubble, which is several hundred parsecs* in size (Lallement et al. 2003). The bubble is thought to have been formed by supernovae from the nearby Sco-Cen association over the last few million years (Fuchs et al. 2009), although the precise nature of the gas within the bubble remains the subject of debate (Welsh and Shelton 2009). Eventually such bubbles either cool to the point where they merge into the surrounding warm medium, or break out of the plane of the host galaxy altogether, ejecting material several kiloparsecs above the galactic plane before raining back down in a 'galactic fountain' (Melioli et al. 2008).

1.1.2.3 Other phases

Whether the well-defined phases of the three-phase model really exist remains a subject of debate (see e.g. Vazquez-Semadeni 2009; Kalberla and Kerp 2009), but they remain a useful approximation which can aid discussion and understanding of the ISM. There are, however, a number of regions of the ISM which the model clearly does not describe, such as molecular clouds and H II regions.

H II regions are hot but dense ionised regions which surround massive stars. They are formed by the recent formation of massive stars, which emit intense UV radiation, ionising and heating the surrounding ISM. Since the stars originally formed within dense molecular clouds, the clouds are gradually destroyed from within. The ISM in these regions has been locally heated far from equilibrium, and gradually expands into the surrounding medium. This process takes longer than the lifetime of the massive stars,

*The parsec (pc) is the distance at which a source would have an observed annual parallax of one arcsecond, and is equal to 3.0857×10^{16} m.

Phase	n (cm^{-3})	T (K)	State of H	State of C
H II region	1–10^5	10^4	H II	-
Hot intercloud	3×10^{-3}	10^6	H II	-
Warm ionised	0.5	8×10^3	H II	-
Warm neutral	0.1	8×10^3	H I	-
Diffuse atomic	50	80	H I	C^+
Diffuse molecular	200	80	H I & H_2	C^+
Translucent	2,000	30	H_2	C^+ & CO
Dense molecular	$> 10^4$	20	H_2	CO

Table 1.1 – Approximate temperature T and number density n for various phases of the ISM and the dominant state of hydrogen and carbon within them. The classical three phases of McKee and Ostriker (1977) roughly correspond to the hot intercloud, warm (both ionised and neutral) and diffuse (both atomic and molecular) media. Data are from Tielens (2005, chapter 1) for the hot and warm phases and Snow and McCall (2006) otherwise.

which explode as core-collapse supernovae, so the contents of the H II region are eventually swept up as part of a supernova remnant.

Molecular clouds are cold, dense regions in which most of the hydrogen is in the form of H_2. The concentration of dust in such regions is such that the centres of the clouds are extremely well shielded from the harsh interstellar radiation field, and consequently a large number of molecules may form. Perhaps the most important of these is CO, which is thought to be the second most abundant molecule in the universe after H_2.

There appears to exist a continuum of interstellar conditions between the cold neutral and dense molecular media, with variations in temperature, radiation field and molecular content. Snow and McCall (2006) have developed a classification scheme for such clouds, which relates many of their properties to the H_2 fraction and degree of incorporation of carbon into molecules. The transition between these 'phases' is thought to be driven by the density of the cloud and its shielding from the ISRF by dust extinction. Snow and McCall (2006) also review the current understanding of these diffuse interstellar media, particularly their molecular content.

1.1.3 Observing the interstellar medium

The ISM has been studied using observations across the electromagnetic spectrum, from radio to X-ray wavelengths. Both emission and absorption by matter in the ISM are observed, both in the spectral continuum and in spectral lines. By combining observations using a wide range of diagnostic techniques, a range of interstellar conditions may be probed and a detailed understanding developed.

Most of the electromagnetic energy in the universe was generated via black-body radiation. The surfaces of stars are, to a first approximation, black bodies which radiate according to the temperature to which they have been heated by transfer of heat from fusion reactions in the stellar core. The cosmic microwave background consists of redshifted* black-body radiation from the early universe.

Despite the high temperatures present in some regions of the ISM, the low density means the gas does not radiate as a black body. However, interstellar dust particles (see section 1.1.3.1) do emit a significant quantity of black-body radiation. Dust grains are destroyed at high temperatures, so most emission occurs in the cooler phases of the ISM. Unfortunately, this places the peak emission in the far-infrared or submillimetre regions (depending on the temperature). Observations at these wavelengths are extremely challenging due to the effects of the atmosphere, detector technology, and interfering thermal emission from the telescope, instrument and atmosphere. Nevertheless, great advances in this field have occurred over the last decade, driven by technological innovation. Astronomers can now measure the emission of dust in external galaxies, and trace the distribution of warm dust in our own galaxy which appears as 'infrared cirrus'. Dust grains are also responsible for interstellar continuum absorption and scattering, which are discussed in section 1.1.3.1.

Information on the interstellar gas is derived from spectral lines, in both emission and absorption. Line emission from the ISM itself is caused by a variety of processes, including recombination and de-excitation. As it is the most common constituent of the ISM, the most widely utilised emission lines are those due to atomic hydrogen. When ionised hydrogen recombines with an electron via the process

$$\mathrm{H\,II} + \mathrm{e}^- \rightarrow \mathrm{H\,I} + n\mathrm{h}\nu, \tag{1.1}$$

a total of 13.6 eV of energy is released. This energy is radiated by one or more recombi-

*The spectra of cosmically distant objects are Doppler-shifted to longer wavelengths by the expansion of the universe – essentially the wavelength of the photons is stretched by the expansion – which is referred to as 'redshift'.

nation line photons hν, with wavelengths ranging from the ultraviolet to radio regions. The branching ratios for this process are such that a significant fraction of recombinations result in the emission of a photon of the H α line at 6562 Å. Regions in which there is a dynamic equilibrium between H I and H II, such as H II regions, thus glow brightly in H α.

There are very few emission lines from the cold neutral medium, and those are limited to submillimetre wavelengths, which are difficult to observe. Therefore, most of our knowledge of these regions is derived from absorption lines. This requires the study of a background light source, and the identification of interstellar absorption lines in its spectrum. By far the most common choice of background object is an early-type star (usually of O or B type), which are optically bright, have simple spectra with clean continua, and the few lines which are present may usually be easily disentangled from the interstellar absorption because of their much greater line widths.

1.1.3.1 Interstellar dust

The dust grains within the ISM are formed by the condensation of some elements from the gas phase into solid particles. Absorption and scattering by these dust grains then causes interstellar extinction, which is the reduction in the brightness of background sources from that which would be observed were the dust not present. Extinction is measured in magnitudes, and defined by the relation:

$$m_\lambda = m_{\lambda_0} + A_\lambda, \tag{1.2}$$

where m_λ is the observed magnitude, m_{λ_0} is the unattenuated magnitude of the source and A_λ is the extinction, all at wavelength λ. The intrinsic brightness and extinction are degenerate quantities, and the wavelength dependence of A is not known *a priori*, so it is usual to measure the difference in extinction between two wavelengths $E_{(\lambda_1-\lambda_2)}$. The most common technique is to measure between the Johnson B and V filters (λ_{eff} = 4400 Å and 5500 Å respectively), which yields:

$$E_{(B-V)} = A_B - A_V. \tag{1.3}$$

Because the extinction due to dust is stronger at shorter wavelengths, the background sources appear redder than they would were the dust not present. Therefore, $E_{(B-V)}$ is referred to as the 'reddening'.

The typical interstellar extinction curve is shown in figure 1.2, as calculated for typical diffuse ISM lines-of-sight (Cardelli et al. 1989). Extinction is stronger in the

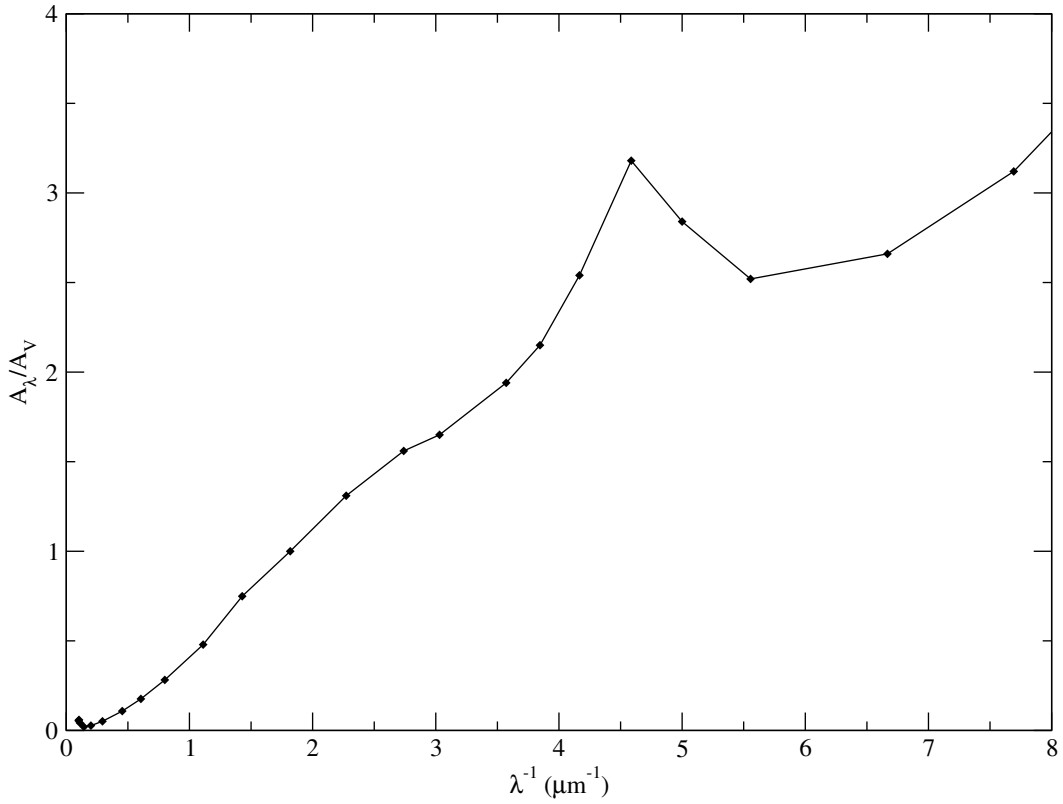

Figure 1.2 – Average interstellar extinction curve, for $R_V = 3.1$, which is typical for the diffuse ISM. The extinction A_λ has been normalised to the extinction in the V band, A_V, and is plotted against the inverse of the wavelength in microns. The extinction curve is approximately linear in the optical wavelength region ($\lambda^{-1} = 1.5$–$3\ \mu m^{-1}$); the large increase in extinction around $\lambda^{-1} = 4.5\ \mu m^{-1}$ is the 2275 Å 'bump'. Data are from Cox (2000), calculated from the models of Cardelli et al. (1989).

UV, and there is a prominent peak at around 2275 Å. The precise origin of this feature – called the '2275 Å bump' – is debated, but is generally thought to be caused by carbonaceous dust absorption i.e. not scattering (see Draine 2003, for a review of interstellar dust properties). Although there are variations in the extinction curve, in the optical it is smooth and approximately linear (cf. figure 1.2), so the reddening and extinction are related by the simple equation:

$$A_V = R_V \times E_{(B-V)} \tag{1.4}$$

where the parameter R_V is referred to as the ratio of visual to selective (or differential) extinction. For most diffuse sightlines $R_V \approx 3.1$, whilst for denser molecular material it can rise to 5 or more (Cardelli et al. 1989). In the absence of directly measured extinction curves, it is usual to simply assume $R_V = 3.1$ and use $E_{(B-V)}$ as a direct measure of

the extinction.

1.1.4 Chemistry in the diffuse ISM

Typical conditions in the diffuse interstellar medium are so cold and at such low density (see table 1.1) that conventional chemistry cannot occur. Species may go months between collisions, but are constantly bathed in the harsh interstellar radiation field and bombarded by cosmic rays. Nevertheless, simple di- and tri-atomic molecules are widely observed in the diffuse ISM. Low rates of reactions may be offset by the thousands to millions of years which may be available without significant changes to local conditions.

Unlike the chemistry occurring in dense molecular clouds, the majority of molecules in diffuse clouds are thought to be formed in gas-phase reactions. Because of the low temperature, only reactions with little or no activation energy barrier may occur. The low density makes three-body collisions vanishingly improbable, so all energy released in a reaction must be carried off by the products. Factors which increase reaction cross-section, such as ion-neutral reactions, provide enhanced rates. Whilst these factors preclude conventional laboratory chemistry, species which are too reactive to exist for long in a laboratory may persist for many years in the ISM.

The most common molecule in the universe, H_2, is an exception to the usual gas-phase chemistry occurring in diffuse clouds, because gas-phase processes are incapable of explaining the large abundances of molecular hydrogen (up to 50% of hydrogen nuclei) in some diffuse clouds. It is thought that most H_2 is formed on grain surfaces, where hydrogen atoms may stick to the surface, and yet have some mobility such that they can move around until they encounter one another. The energy released in the formation of H_2 may then be imparted into the dust grain and the kinetic energy of the H_2 molecule as it leaves the surface. The dust grain essentially acts as a catalyst for the reaction

$$H + H \overset{\text{dust grain}}{\rightarrow} H_2. \tag{1.5}$$

Because atomic hydrogen has an ionisation energy of 13.60 eV, the majority of photons with higher energy than this either do not escape from the photospheres of stars or, in the case of early type stars with little neutral hydrogen in their atmospheres, are absorbed by neutral atomic hydrogen in the interstellar medium. Photons with energies below this threshold are relatively unattenuated in the diffuse ISM, so those species which are both abundant in the ISM and have ionisation energies less than 13.60 eV

may easily be ionised by the ISRF. In diffuse clouds, the most common such species is neutral atomic carbon, which is easily ionised:

$$\mathrm{C} + \mathrm{h}\nu\,(> 11.26\,\mathrm{eV}) \rightarrow \mathrm{C}^+ + \mathrm{e}^-. \tag{1.6}$$

This reaction provides the source of most of the free electrons in the diffuse ISM, and in diffuse clouds C^+ is the dominant form of gas-phase carbon (Snow and McCall 2006). Unlike the neutral atom, ionised carbon can react via ion-neutral reactions such as radiative association with H_2:

$$\mathrm{C}^+ + \mathrm{H}_2 \rightarrow \mathrm{CH}_2{}^+ + \mathrm{h}\nu. \tag{1.7}$$

However, the rate of this reaction is very low ($k = 4 \times 10^{-16}\,\mathrm{cm}^3\,\mathrm{s}^{-1}$ at 300 K). The large column densities of CH^+ observed along many diffuse sightlines indicates that C^+ must instead react with H_2 via the reaction

$$\mathrm{C}^+ + \mathrm{H}_2 \rightarrow \mathrm{CH}^+ + \mathrm{H}, \tag{1.8}$$

forming CH^+. Unfortunately this reaction is endothermic by $E/k_B = 4640$ K, so cannot proceed in typical diffuse cloud temperatures of 80–100 K. For this reason, explaining the abundance of CH^+ (along with H_3^+) is the largest unsolved problem for models of diffuse cloud chemistry. The additional energy input may be provided by shocks (though Crawford 1995 has argued against shocks on observational grounds), magnetic acceleration of ions, Alfvén waves or turbulent dissipation. See Indriolo et al. (2010) for a discussion of the CH^+ problem and a description of simple carbon chemistry in the diffuse ISM.

Once CH^+ has been formed, it can then react with further molecular hydrogen:

$$\mathrm{CH}^+ + \mathrm{H}_2 \rightarrow \mathrm{CH}_2^+ + \mathrm{H}. \tag{1.9}$$

CH_2^+ may then react with further H_2 to form CH_3^+, or recombine with an electron (which most likely originated from equation 1.6) to form CH:

$$\mathrm{CH}_2^+ + \mathrm{e}^- \rightarrow \mathrm{CH} + \mathrm{H}. \tag{1.10}$$

Direct recombination of CH^+ with electrons does not produce CH, because the energy released is above the dissociation limit of the molecule and instead dissociative recombination occurs:

$$\mathrm{CH}^+ + \mathrm{e}^- \rightarrow \mathrm{C} + \mathrm{H}. \tag{1.11}$$

The methalydine radical CH serves as the basis of more complex carbon chemistry through the formation of C_2 (van Dishoeck and Black 1989):

$$\begin{aligned} CH + C^+ &\rightarrow {C_2}^+ + H, \\ {C_2}^+ + e^- &\rightarrow C_2 + h\nu. \end{aligned} \tag{1.12}$$

Further reactions with C^+ and H_2 lead to larger molecules such as C_3, C_2H_2 etc. Analogous oxygen-based pathways lead to the formation of OH, HCO^+ and CO, though in smaller quantities than those found in dense molecular clouds. See Flower (2007, chapters 1&2) for a more detailed description of chemistry in the diffuse interstellar medium.

All of the molecules discussed above are destroyed by cosmic rays and UV photons from the ISRF, either through photoionisation or photodissociation. Positive molecular ions may also be destroyed through dissociative recombination. Simple di- and tri-atomic molecules exist in significant quantities because their formation mechanisms are sufficiently rapid to keep up with their destruction. Larger polyatomic molecules (those with 5–20 atoms) are generally absent because of the improbability of navigating through many stages of the chemical reaction network without destruction. Sufficiently large molecules such as polycyclic aromatic hydrocarbons (PAHs, see section 1.2.2) may be capable of surviving in the diffuse ISM because their many bonds mean the excess energy of an incident UV photon may be redistributed throughout the molecule then later radiated away, rather than leading to dissociation. Reactions on grain surfaces or in other regions such as circumstellar envelopes must be invoked to explain the initial formation of such large molecules.

1.2 The diffuse interstellar bands

As long ago as 1922, Mary Lea Heger of Lick Observatory noticed absorption features at 5780 and 5797 Å in the spectra of several B-type stars, including ζ Per (Heger 1922)*. Subsequently, Merrill (1930) serendipitously noted a set of five absorption lines centred at 5780, 5796, 5944, 6283 and 6613 Å towards HD 183143. The lines were first systematically investigated by Merrill (1934), who suggested that they were probably of

*The author has recently noted that Heger (1922) mentions earlier work by Cannon and Pickering (1901, their table 27), who apparently also saw these lines towards γ Vel. Further investigation to confirm whether this is indeed the first reported observation of DIBs is ongoing.

interstellar origin and noted that "instead of being narrow and sharp, however, as interstellar lines should be, they are somewhat widened and have rather diffuse edges". Merrill (1936) then used observations of the fast-orbiting binary star HD 224151 to conclusively demonstrate that the 5780 and 6283 Å features were of interstellar origin.

These lines became known as the 'diffuse interstellar bands' (DIBs, or informally 'diffuse bands'), because of their interstellar nature and Merrill's description of the lines as "diffuse". At the time of writing, over 400 of these bands are now known (Hobbs et al. 2008, 2009), but despite decades of work none of the carriers* have been identified. The identification of the carriers has been described as "the longest standing unsolved problem in all of spectroscopy" (Krełowski et al. 1993). Comprehensive reviews on the subject have been given by Herbig (1995) and Sarre (2006).

Because the carriers of the lines are not yet known, DIBs are referred to by the wavelength at which they appear. The standard nomenclature is e.g. λ5780, where 5780 is the central wavelength of the band in Å. The wavelength is usually rounded *down* to the nearest Å (Herbig 1975). Improved data on the central wavelength and inconsistent usage has however resulted in some DIBs being referred to by more than one name: λ6613 and λ6614 actually refer to the same band. Other bands which are affected by this ambiguity are λ5849/λ5850, λ6283/λ6284 and λ4428/λ4430.

1.2.1 Correlations and families

One of the properties of DIBs which must be taken into account for assigning the carriers is that the individual DIBs do not behave proportionally to each other. Whilst the DIBs generally come and go together, strict relations between the bands are absent. Considerable intrinsic variations in the relative strengths of the DIBs between sightlines exist. For example, although many DIB strengths display a reasonable correlation with $E_{(B-V)}$, plots of the equivalent widths of pairs of DIBs against each other exhibit considerable scatter (e.g. Herbig 1975, 1993). This is generally interpreted as indicating that each DIB is caused by absorption from a different carrier, or at least a differing level of excitation of a given carrier. One exception may be the λ6196/λ6613 pair, which have been found to be very well correlated with each other (Moutou et al. 1999; McCall et al. 2010); this may be considered to be good evidence for a single carrier for this pair of DIBs.

Despite this difficulty, a number of correlations of DIB strength with other interstel-

*The 'carrier' of a line is the chemical species whose transitions are responsible for the line.

lar properties are observed. The first study of this type was performed by Merrill and Wilson (1938), whilst more recent extensive studies have been performed by Herbig (1993) and Thorburn et al. (2003). As a result, a number of relations are known, some of which are strong whereas others are weak at best. For example, Munari et al. (2008) found an extremely tight correlation between the equivalent width of λ8620 and $E_{(B-V)}$; the correlation is accurate to within about 2% and may even be limited by uncertainties in the observations rather than instrinsic scatter*. Conversely, the correlation between λ5780 and $E_{(B-V)}$ is widely used (see chapter 5) but for a given value of $E_{(B-V)}$ there is intrinsic scatter by a factor of about 2 in the relation.

The correlation of DIBs with known atomic and molecular lines is generally rather poor, and may reflect nothing more than the general quantity of interstellar material along the line-of-sight, regardless of the chemical composition. For example, Herbig (1993) found correlations between the EWs of DIBs and the atomic species Na I and K I, but with considerable real scatter. No correlation was found with H_2, CH^+ or the shape of the extinction curve. The lack of correlation with CH^+ indicates that DIB carriers are probably not formed in the shocks thought to be responsible for CH^+ formation (Herbig 1993; Krełowski et al. 1999) (see section 1.1.4). Thorburn et al. (2003) recently found a set of weak DIBs whose absorption correlates well with that of the C_2 molecule.

Although most investigations have concentrated on correlations with $E_{(B-V)}$, the evidence for a gas-phase carrier (see section 1.2.2) suggests that there may be better correlations with tracers of gas rather than dust. Herbig (1993) found that the strength of λ5780 varied in proportion to N(H I). However, the correlation is no stronger than that with $E_{(B-V)}$, though there may be a number of observational reasons for this. Firstly, N(H I) is relatively difficult to determine directly, usually relying upon measurement of the heavily-saturated Lyman α line in the ultraviolet. Secondly, in diffuse interstellar clouds where the DIBs are observed, a significant proportion of the hydrogen is in the form of H_2, so N(H I) may not accurately trace the amount of gas-phase material along the line-of-sight.

Krełowski and Walker (1987) identified three 'families' of DIBs whose members are better correlated with each other than with the members of other families. The groupings (with updated memberships) are:

1. Very broad DIBs with Lorentzian profiles: λ4428, λ6180;

*The GAIA satellite, currently planned to launch in 2012, will utilise this relation to determine $E_{(B-V)}$ for thousands of stars.

2. DIBs with smooth profiles, but a range of shapes and widths: λλ5780, 6203, 6269, 6283;

3. Narrow DIBs with complex asymmetric profiles: λλ5797, 5850, 6376, 6379 and 6613;

and are hereafter referred to as KW group 1 etc. In general, KW group 2 DIBs have the tightest relation with $E_{(B-V)}$. KW group 3 is particularly interesting because all of the diffuse bands with observed fine structure (see section 1.2.2) are members of this group, and they are strongest along lines-of-sight with the relatively dense material traced by diatomic molecules.*

Krełowski et al. (1992) identified two classes of diffuse interstellar cloud, referred to as σ- and ζ-type clouds after the prototypical sightlines towards σ Sco and ζ Per. A σ-type cloud is characterised by the presence of interstellar atomic lines and DIBs, but absorption due to diatomic molecules is weak or absent. ζ-type clouds are characterised by strong absorption due to diatomic molecules in addition to DIBs and atomic lines. The extinction curves of the two cloud types also vary, with $R_V \approx 3.1$ in ζ-type clouds but $R_V \approx 4.5$ in σ-type clouds (Krełowski and Sneden 1995). The key difference between the two types is thought to be a combination of density and UV irradiation by the ISRF, with σ-type clouds being those with low density and/or high UV radiation. Interestingly, the DIBs of KW group 3 are strongly dependant on the σ/ζ type, with strong KW group 3 DIBs present in ζ-type lines-of-sight. Krełowski and Sneden (1995) also noted the presence of additional weak DIBs in ζ-type clouds.

DIBs have been detected in emission in just two objects. The first is the Red Rectangle (RR), a carbon-rich protoplanetary nebula with an extraordinarily rich spectrum over both optical and infrared wavelengths. The correspondence between several broad emission features in the RR with some of the DIBs was first noted by Sarre (1991). Although the wavelengths of the emission features are several angstroms redward of the diffuse band wavelengths at the centre of the nebula, they are observed to shift towards the DIB wavelengths as the distance from the central star increases (Sarre et al. 1995b; van Winckel et al. 2002). Only a subset of DIBs are seen in emission, limited to the DIBs of KW group 3. The other object with DIBs in emission is the RCB star†

*The tight correlations between the 'C_2' DIBs identified by Thorburn et al. (2003) were unknown at the time, and these DIBs may constitute a fourth grouping.

†R Coronae Borealis-type (RCB) stars are a class of extremely hydrogen deficient carbon stars, which undergo dimming by 2–7 magnitudes in V at unpredictable intervals, usually lasting several weeks or months. The dimming is thought to be caused by sudden formation of dust around the star.

V854 Cen, which shows emission at wavelengths close to those of the RR when at minimum light (Rao and Lambert 1993). The logistical difficulties imposed by time-dependent emission has hampered the study of these bands; only a single spectrum of DIB emission features in this object has been published in the literature.

1.2.2 Identifying the carriers

The possibility that the DIBs might be due to transitions in gas-phase atoms was ruled out by Merrill and Wilson (1938), on the grounds that interstellar absorption must occur in resonance lines*. These were well known in the laboratory and no known process existed to broaden them to the observed widths of the DIBs.

The correlation of at least some DIBs with $E_{(B-V)}$ led to the suggestion that DIBs might be related to dust grains. The absorption could be directly by dust grains, perhaps those containing impurities, or alternatively by a species adsorbed onto the surface of a grain. However, the advent of ultra-high resolution spectrographs in the 1990s revealed that a subset of DIBs have spectral structure resembling that of the rotational bands of gas-phase molecules (Sarre et al. 1995a; Kerr et al. 1996, 1998; Galazutdinov et al. 2002, 2008; Słyk et al. 2006). Those DIBs which have been found to show this behaviour are all narrow DIBs of KW group 3; this may be a unique property of the group or might simply indicate that the additional broadening present in the other groups 'washes out' the effect. There is an additional selection effect: studying broad DIBs at ultra-high resolution is difficult because the definition of the continuum level becomes uncertain, and the DIB may not fit into the wavelength region covered by a single observation (or echelle order within an observation).

The expected shifts in wavelength for a carrier adsorbed on the surface of a dust grain have been advocated by some authors as a method for broadening transitions to those seen for the DIBs (e.g. Herbig 1963). However, the constancy of the DIB wavelengths and widths constitutes strong evidence for gas-phase carriers because these quantities would be expected to vary depending on the surrounding material in a solid-state carrier. A review of the evidence for, and constraints on, gas-phase molecular carriers has been presented by Fulara and Krełowski (2000). More recently, Cox et al. (2007a) used spectropolarimetry to search for polarisation in DIB absorption profiles, which would be expected if the carriers were dust grains (or adsorbed on their surfaces), but no additional polarisation was found.

*Resonance lines are those to/from the atom in its ground electronic state.

If the DIB carriers exist in the gas phase, a new mechanism must be found to account for the width of the bands. Several possible mechanisms exist, including unresolved rotational lines, rapid molecular internal conversion in the upper state of the transition, or an ensemble of different carriers each of which contribute absorption at similar but not identical wavelengths. Each of these possibilities points towards large molecules as the carriers. For enough large molecules to be present in the ISM without violating the known abundances of elements, they must predominantly consist of relatively common elements such as H, He, C, N, and O*. Other elements may be incorporated, but cannot make up the bulk of a gas-phase carrier. Because carbon easily forms a vast range of molecules, most proposals for gas-phase carriers have concentrated on organic molecules.

One of the most popular suggestions for carbon-based carrier molecules are the fullerenes†. For example, in their initial paper announcing the discovery of the first fullerene Kroto et al. (1985) suggested that C_{60} might be a DIB carrier, but the absorption spectrum measured subsequently showed no agreement with any of the DIBs. Fossey (1991) argued against the idea discussed by Sarre (1991) that C_{60} might be responsible for diffuse bands seen in emission in the Red Rectangle nebula, on the grounds that the rotational constant did not fit with the observations. Kroto and Jura (1992) discussed the possibility that DIBs might be carried by fullerene complexes with metal atoms, both inside and outside the carbon skeleton. The buckminsterfullerene cation C_{60}^+ has been proposed as the carrier of the λ9577 and λ9632 DIBs (Foing and Ehrenfreund 1994), but this identification has not yet gained widespread consensus and is still the subject of debate (Maier 1994; Jenniskens et al. 1997; Galazutdinov et al. 2000; Misawa et al. 2009). More recently, Iglesias-Groth (2007) suggested a specific subset of fullerenes might be responsible for the λ4428 DIB.

Short carbon chains such as C_2 and C_3 have been detected in the ISM, which has lead to the suggestion that longer carbon chains might be responsible for some DIBs. Tulej et al. (1998) proposed that the C_7^- chain might be responsible for several DIBs, but further observational data has specifically ruled out this possibility (e.g. McCall et al. 2001). Maier et al. (2004) have examined carbon chains in detail, and were able to rule

*The relative abundances of the elements in the ISM are generally assumed to be similar to those in the Sun, which is in agreement with the considerably more uncertain abundances derived from nearby H II regions and B-type stars (see Asplund et al. 2009 for a review of abundance issues).

†Fullerenes are hollow three-dimensional molecules consisting entirely of carbon, the simplest of which is the spherical buckminsterfullerene molecule C_{60}.

out many as DIB carriers. However, bare chains with odd numbers of carbon atoms in the range C_{15}–C_{31} were identified as possible carriers. No gas phase laboratory data for these chains is available, so the proposal cannot yet be tested, though matrix data seem promising (Jochnowitz and Maier 2008). Short sections of carbon nanotubes have also been suggested as DIB carriers by Zhou et al. (2006). Ball et al. (2000) detected absorption at 4429 Å in a cold plasma consisting of fragments of the benzene molecule, but further investigation by Araki et al. (2004) ruled this out as the origin of the λ4428 DIB, despite identifying the C_5H_5 fragment responsible for the absorption. Linnartz et al. (2010) recently detected absorption with the same wavelength and band profile as the λ5450 DIB in a laboratory hydrocarbon plasma, but were unable to identify the species responsible.

In the vast majority of cases specific proposals of carriers for particular DIBs have been hampered by the lack of laboratory data, particularly in the gas phase. Theoretical calculations have been utilised, but these suffer from systematic uncertainties in wavelength and so can only serve to guide laboratory investigations, rather than provide definitive assignments. Sarre (2000) suggested that transitions to dipole-bound states in negatively charged molecules might be responsible for some DIBs. Cordiner and Sarre (2007) used computational techniques to investigate the specific proposal that a transition to a dipole-bound state in the cyanomethyl anion CH_2CN^- might be responsible for the λ8037 DIB, but this identification remains highly uncertain.

The most widely supported theory for the carriers of the diffuse interstellar bands is that of the class of polycyclic aromatic hydrocarbons (PAHs). These are planar molecules consisting of multiple aromatic carbon rings, with hydrogen terminators at the edges of the molecule. The simplest PAH is naphthalene, which consists of two fused aromatic rings, whilst the largest may consist of hundreds of linked rings. There are several reasons why PAHs are the currently preferred candidate carriers of DIBs, but two of the most supportive are that PAHs are known to be both abundant and stable in the ISM.

During the 1970s, a set of broad emission features in the mid infrared were discovered which always appeared together. The strongest of these were located at 3.3, 6.6, 7.7, 8.6, 11.2 and 12.7 μm, which become known as the unidentified infrared (UIR) bands. These bands appeared in a wide variety of sources including H II regions, planetary and protoplanetary nebulae, reflection nebulae, evolved stars and young stellar objects. These are all locations in which dense interstellar or circumstellar material is exposed to ultraviolet radiation. The bands are so intense in such objects that they make

a significant contribution to the spectral energy distribution of entire galaxies.

The identification of the carrier of these features was achieved by Léger and Puget (1984), who noted that these bands correspond to various vibrational modes of PAH molecules*. The mechanism for the emission is excitation by a UV photon, followed by internal conversion of the energy into the various vibrational modes of the molecule which then gradually relax by emission of mid-IR photons. Although the features are indicative of PAHs as a class, they do not uniquely identify any particular PAH. Indeed, modelling of any particular source requires a range of PAHs, including their cations, to explain the observed intensities of the bands. Roughly 1% of the interstellar carbon budget is thought to be in the form of PAHs. A review of the evidence for – and properties of – PAHs in the ISM has been given by Tielens (2008) (see also Tielens 2005, chapter 6).

Because the PAH molecules are not destroyed by UV radiation, they are expected to survive distribution into the diffuse ISM. In the absence of strong UV irradiation, the mid-IR emission becomes undetectable but the molecules may then be responsible for various absorption features. This was quickly realised by Léger and d'Hendecourt (1985), who suggested that PAHs might be DIB carriers. Although neutral PAHs generally absorb most strongly in the UV, cationic and protonated varieties are expected to exhibit strong absorption features in the optical region (Hirata et al. 2003; Pathak and Sarre 2008). Theoretical modelling of the charge state of PAHs in the ISM suggests that significant fractions should be in such cationic or protonated states (Le Page et al. 2003). Optical transitions may also be the result of impurities in the PAH, such as nitrogen substitution or the attachment of side chains.

The 'PAH-DIB hypothesis' has a number of other useful characteristics. The large number of possible PAHs, particularly when multiple protonation/substitution sites are considered, may account for the large number of observed DIBs. If protonated or cationic species are indeed the carriers, regions of higher electron density (such as in dense clouds) would be expected to host fewer of these carriers, possibly explaining the relative weakness of DIBs in these locations. The widths and central wavelengths of PAH absorptions have been shown to be relatively insensitive to a range of interstellar conditions, including radiation field and isotopic substitution , in agreement with the observed constancy of these DIB properties (Malloci et al. 2003). The widths of the bands could be provided by unresolved rotational broadening, with different sized PAHs resulting

*As the bands are no longer 'unidentified', they are sometimes referred to as aromatic infrared bands (AIBs) or as 'PAH features'.

in a range of widths roughly coincident with the observed DIB widths. Alternatively, the width could be caused by rapid intra-molecular internal conversion, which reduces the lifetime of the upper state in the transition. Finally, the hypothesis is consistent with the presence of DIBs in emission from the Red Rectangle, which is one of the brightest UIR sources on the sky.

Despite these properties, the PAH-DIB hypothesis has not yet resulted in the positive identification of the carrier of any single band, and makes a number of predictions which have not yet been confirmed. In particular, the presence of PAHs throughout the ISM should result in observable *absorption* in the UIR features, which has not yet been definitively detected. Neutral PAHs should cause strong interstellar absorption bands in the UV, which have not been identified. However, this may be due to the difficulty of observation at these wavelengths, which are restricted to nearby lightly-reddened sources, frequently suffer from confusion effects, and the bands themselves may be broad enough to escape detection. Perhaps most seriously, background sources lying behind regions in which PAHs are known to be present via their mid-IR emission should show increased DIB absorption, but no such increase has been found despite sensitive searches (e.g. Le Bertre and Lequeux 1992; Mauron and Kendall 2004).

1.3 Small-scale structure in the ISM

The three-phase model discussed in section 1.1.2.2 has been extremely successful in explaining the gross properties of the diffuse ISM (i.e. excluding the regions discussed in section 1.1.2.3) (Heiles and Troland 2003; Cox 2005). However, over the last 20 years a body of evidence has accumulated that indicates that the ISM is highly structured on scales of tens to thousands of AU*, and that such small-scale structure (SSS) implies pressures in contradiction with the three-phase model.

1.3.1 Observational evidence

It has long been known that the ISM is far from homogeneous. The largest interstellar structures are the galactic spiral arms, which are seen to extend coherently over at least 10 kpc. The arms are generated by spiral density waves which concentrate material in a rotating pattern. This enhances the local star formation rate within the arms and leads to

*The astronomical unit (AU) was originally defined as the mean distance between the Earth and the Sun, and is equal to 1.4960×10^{11} m; 1 pc $\approx 206,265$ AU.

the presence of many bright (and short-lived) stars within the arms. Some short 'spur' arms, such as the Orion-Cygnus arm within which the Sun currently resides, are only a few kpc long.

The next largest interstellar structures are superbubbles such as the Local Bubble and Loop I Bubble (see section 1.1.2.2), which can reach diameters of ~ 1 kpc (Dickey and Lockman 1990; Welsh and Shelton 2009). Other large-scale structures include supernova remnants, H II regions and molecular cloud complexes. Star forming regions and individual molecular clouds are complex places where structures on very small scales (at least down to the size of a star) are known to exist. However, the diffuse ISM which exists between these objects was – until the observations discussed below – thought to be well described by the three-phase model of McKee and Ostriker (1977). In this model the smallest structures are clouds of cold neutral medium (CNM) of diameter ~ 1 pc; there was thought to be no significant variation *within* CNM clouds. Indeed, observations designed to probe this length scale suggested an apparent cut-off size for variations of any kind at around 0.2 pc (Crovisier et al. 1985).

The first observation of structure in the diffuse ISM on scales smaller than a parsec actually slightly pre-dated the three-phase model. Dieter et al. (1976) used the high angular resolution available in very-long baseline interferometry (VLBI) to map H I 21 cm absorption towards the quasar 3C 147, and found significant variations on scales down to the instrumental limit of 70 AU. Over a decade passed before Diamond et al. (1989) provided the first confirmatory observations, and extended the results to two other sources (3C 138 and 3C 380). Towards 3C 138, the inferred structure in the diffuse ISM was clouds of size $\lesssim 25$ AU with densities of 10^4-10^5 cm^{-3}, which is several orders of magnitude higher than that in 'typical' CNM (c.f. table 1.1). More recent observations at even higher spatial resolution have pushed the scale down to 10 AU, again limited by the instrumental resolution (Lazio et al. 2009).

Observations were extended to the electronic transitions of atoms by Meyer (1990) who examined interstellar line absorption towards several nearby binary stars using UV and optical spectroscopy. Some species were found to vary by up to 50% between the two stars of κ CrA, which has a projected separation of 2,800 AU. Meyer and Blades (1996) detected similar variations towards the binary pair μ Cru, separated by 6,600 AU. Watson and Meyer (1996) conducted optical observations towards 17 binary systems, and identified variable interstellar absorption in every system, over separations of 480–29,000 AU. Optical binary studies accumulated quickly; almost all sightlines studied showed variation in at least some species. An extension into two dimensions can be

achieved by observing towards a star cluster; these studies are described in section 4.2.

An alternative to the spatially-resolved observations described above is to take multiple observations towards an object with high transverse velocity (as determined from its proper motion). As the line-of-sight sweeps across the intervening ISM, repeat observations reveal column densities along various lines of sight through a cloud. This technique can reach down to very small scales, but at the cost of greater systematic uncertainties due to the possible motion or time-evolution of the cloud itself. The earliest observations of this type were performed by Frail et al. (1991), who found temporal variations in H I 21 cm absorption towards the pulsar PSR 1821 +05. Further studies by Deshpande et al. (1992) and Frail et al. (1994) extended this to a sample of nine pulsars, every one of which showed variations over scales of 5–110 AU.

The first temporally resolved optical observations were presented by Hobbs et al. (1982), who detected a previously absent component of Ca II K absorption towards the star HD 72127 A and an increase of 25% in the total equivalent width of the Ca II K line. Further study showed variations of up to 45% over a time span of five years (Hobbs et al. 1991). Unfortunately the distance scale over which these variations occurred was not well constrained because this star lies behind the Vela supernova remnant, within which the absorbing material was assumed to lie. Nevertheless, a reasonable upper limit on the transverse velocity of the gas ($\lesssim 100\,\mathrm{km\,s^{-1}}$) resulted in an upper limit on the distance scale of 300 AU.

As ultra-high resolution optical spectrographs became operational during the 1990s, the number of known temporally varying interstellar lines-of-sight expanded. Very high spectral resolution is a major advantage for such observations because it allows the individual absorbing clouds to be distinguished, which enhances the detectability of a single varying component amongst several static components. Optical studies of time-varying interstellar absorption were reviewed by Crawford (2003); at the time thirteen such lines-of-sight were known.

Over the last decade, studies in the UV, optical and radio have continued to accrue, but many of the key observational questions remain unanswered. These include information on how widespread SSS is, the distribution it takes up, and what the typical physical and chemical conditions are within the structures. Details on these challenges, and the existing observational constraints, are discussed by Heiles and Stinebring (2007), whilst a review of the UV and optical observations is given by Lauroesch (2007).

1.3.2 Formation and implications

The observational evidence for small-scale structure in the diffuse ISM generated theoretical interest in the processes responsible for its formation and the implications such structures may have for the physics and chemistry of the ISM. The first comprehensive attempt to develop a self-consistent model for SSS was made by Heiles (1997), who considered possible scenarios to explain large variations in interstellar column density without grossly violating interstellar pressure equilibrium. Heiles' preferred model consisted of a population of cold dense structures in the form of sheets or filaments. The variations could then be due to such a filament aligned along the line-of-sight; this allows large variations in column density without the necessity for extreme volume density.

The model of Heiles (1997) requires a very low temperature ($\sim$ 15 K), because it imposes the constraint that the small-scale structures must be in pressure equilibrium with the surrounding ISM. However, evidence for such a low temperature has not been observationally forthcoming, and theoretical attention has shifted towards solutions which are not in dynamical equilibrium and thus do not require such pressure balance. Such clouds are expected to evaporate quickly, though exactly how quickly depends sensitively on the exact conditions assumed – estimates have ranged from 50 to 10^6 years. A revision of the Heiles (1997) model which incorporates more recent observational evidence and the possibility of non-equilibrium dynamics has been presented by Heiles (2007). Some process must be found which replenishes the population of SSS on similar timescales; perhaps the most promising suggestion has been the passage of magnetohydrodynamic waves (e.g. Hartquist et al. 2003).

The existence of a population of small-scale dense clouds within the CNM has important implications for interstellar chemistry. Although the ISRF is expected to be essentially unattenuated within such small structures (at least in the transverse direction), the high density can result in enhancement of the molecular content (Bell et al. 2005). This provides both a potential method for obtaining new information on the physical conditions, and may offer a solution to some of the challenges which exist in reproducing the abundances of molecules observed in the CNM (Cecchi-Pestellini et al. 2009). It is vital that a comprehensive understanding of the physical conditions with the SSS is developed, so that it may be fed into such chemical models.

1.4 Thesis overview

This thesis presents research which seeks to address the following questions:

- How is matter in the ISM distributed on scales from the size of the solar system to the size of a galaxy? What does this distribution imply for the formation of molecules?
- How do the properties of DIBs compare between the local ISM and the ISM in other galaxies?
- Can DIBs be utilised as probes of the ISM, despite our incomplete knowledge of their nature and carriers?

The techniques which have been used are described in chapter 2. High spectral resolution studies of temporally-resolved small-scale structure are presented in chapter 3. In chapter 4, results are presented of two studies of spatially-resolved SSS, using diffuse bands as probes. Finally, the first detections of DIBs in the M33 galaxy are described in chapter 5 and the thesis is summarised in chapter 6.

Chapter 2

Data collection and analysis

Great advances in our understanding of the physics and chemistry of the interstellar medium have been made through laboratory experiments and theoretical modelling. These techniques require input from astronomical observations of the ISM, which motivate the direction these studies should explore and test the predictions they make. All the data presented in this thesis are observational in nature, utilising some of the world's largest telescopes.

2.1 Telescopes

The most common astronomical observation is to simply look at the sky with the naked eye. However, the human eye imposes severe limitations on the study of the heavens. The most important of these limitations are the impossibility of accurately recording what is seen, low sensitivity to faint objects, and poor angular resolution. The use of a telescope, together with an attached instrument, allows these problems to be mitigated or circumvented. The importance of the telescope to the astronomer cannot be overstated; the two are inextricably linked in the public imagination.

2.1.1 Characteristics

The basic function of a telescope is to collect light from a region of the sky then concentrate and focus the light to form an image. That image may then be viewed with an eyepiece, or fed to an instrument mounted on the telescope for further optical processing and recording on a detector. The earliest telescopes consisted of refracting lenses,

but these are limited in size by the twin problems of chromatic aberration* and accurately maintaining the shape of a lens which can only be supported around its edges. Large telescopes are now universally reflecting telescopes, which use mirrors formed from a thin layer of metal (usually aluminium) deposited on glass or a low thermal expansion substrate, which can then be supported from behind. Even these are limited to a maximum of about 8 m by the manufacturing process, transportation to the telescope site and the need for observatory facilities to periodically re-coat the mirror. The latest generation of large telescopes therefore use a segmented mirror, in which a large number of small mirrors are held in precise alignment in order to mimic the surface of a larger single mirror. A history of the development of the telescope is given by Kitchin (2009, §1.1.17).

By collecting light from a much larger area than the pupil of the human eye, a telescope collects more photons from any given source, and hence allows the observation of fainter objects. Because the area increases with the square of the radius for a circular mirror (the most common shape), large telescopes become vital for work on faint objects. The light-gathering power of a telescope is generally (and rather roughly) indicated by the diameter of its primary mirror, which is commonly quoted when referring to a telescope. The largest single telescope in operation at the time of writing is the 10.4 m Gran Telescopio Canarias (GTC), located on the island of La Palma, Canary Islands.

The second advantage of the telescope over naked eye observations is that of angular resolution. The pupil of the human eye or the primary mirror of a telescope act as apertures which cause the incoming light to diffract. This diffraction limits the angular displacement of two objects which may be separated on the final image. By applying the Rayleigh criterion, which requires that the two sources must appear in the final image separated by at least the FWHM of the resulting diffraction pattern, the angular resolution $\Delta\theta$ is given by:

$$\sin \Delta\theta = 1.220 \frac{\lambda}{D} \tag{2.1}$$

where λ is the wavelength of the light and D is the diameter of the aperture. For the dark-adapted human eye working at visible wavelengths, $\Delta\theta$ is about $20''$†, whilst for a 1 m telescope $\Delta\theta \approx 0.1''$.

*Because the refractive index of glass changes with wavelength, the focal point of a lens varies with the colour of the incoming light, which is called 'chromatic aberration'

†Due to the coarseness of the cells in the retina, the resolution of the human eye is actually limited to about $1'$

Unfortunately the advantages in angular resolution offered by the telescope are rarely achieved in practice, because of the effect of the Earth's atmosphere. Turbulent motion within the various atmospheric layers results in the blurring of the image of the sky by an amount referred to as the 'seeing'. The precise value of the seeing varies with a range of factors, the strongest of which are the geographic location of the telescope and the weather. For a good astronomical site in clear weather, a value of $1''$ is typical.

2.1.2 Instruments and focal stations

The third main advantage of the telescope over the human eye is that the signal may be recorded using a detector. In almost all cases, some further optical processing – such as filtering or dispersion – is also performed. The functions beyond the formation of the initial image are performed by a separate piece of equipment, referred to as the 'instrument', which is attached to the telescope. Depending on the design of the telescope, the image may be formed at a variety of different points, referred to as focal stations.

The simplest telescope design uses a single mirror which directly forms an image at its focal point, referred to as the 'prime focus'. Although the prime focus design is simple and minimises the number of reflections (and associated light losses), it suffers a number of disadvantages. Placing an instrument at prime focus blocks some of the incoming light from hitting the primary mirror. In addition, the instruments are difficult to access and require a heavy support structure. Finally, the image suffers from severe off-axis distortions. Nevertheless, the prime focus continues to be used for some applications because it provides a wide field of view, although a correcting lens must be used to reduce distortions. The problem of intercepting incoming light may be reduced by the insertion of a flat mirror to deflect the light to one side. The result is a Newtonian telescope. All the other disadvantages of prime focus remain, and the Newtonian design is rarely used on large telescopes, though it is a popular design in amateur astronomy.

The most common design for large telescopes is the Cassegrain, which inserts a small convex secondary mirror in front of the primary. The secondary reflects the light back through a hole in the primary to a focal point behind the main mirror, which is a much more convenient location for an instrument. By precise figuring of the mirrors (to form a so-called Ritchey-Chrétien system), most distortions can be eliminated or dramatically reduced. The main disadvantages of the Cassegrain layout are small field of view and the requirement for the instrument to tilt along with the telescope, which im-

poses mechanical stresses. These stresses cause the structure of the instrument to flex, which interferes in the operation of high-resolution spectrographs. These instruments require a flat, stable platform upon which to rest; in extreme cases the instrument must be contained in a temperature controlled vacuum vessel. The simplest solution to this problem is to feed the spectrograph via optical fibres mounted at one of the foci discussed above. Alternatively, additional mirror(s) may be added to a Cassegrain design to relocate the focus to a more stable position. The precise layout depends on the telescope mounting; on the common altitude-azimuth mount the solution is the Nasmyth design. A platform is built at the Nasmyth focus to the side of the main mirror, which must rotate with the telescope in azimuth, but remains flat regardless of telescope altitude. The equivalent (but more complex) solution for equatorially mounted telescopes is the Coudé focus, which requires a total of five mirrors and has a very small field of view.

Most large telescopes may be used at several of these focal stations by interchanging some parts. This allows instruments to take advantage of whichever properties they require; together with a suite of instruments this grants the telescope a great deal of flexibility in the science it can perform.

Most – though not all – instruments may be divided into two classes: imaging cameras and spectrographs. Imaging cameras directly record the image of the sky formed by the telescope onto a detector. By placing a filter in the light path (such as the broadband filters of the Johnson-Cousins *UBVRI* system), information on the spectral energy distribution of a source may be obtained. Precision measurement of sources through a variety of filters is termed 'photometry' and is a very powerful technique. However, far more information may be obtained if the light from the source is dispersed to form a spectrum, such that the spectral energy distribution may be measured at a range of wavelengths simultaneously. Instruments which record the spectrum of a source are termed spectrographs.

2.2 Spectrographs

An instrument which allows the user to view the spectrum of a source by eye is termed a 'spectroscope' (these are of course limited to visible wavelengths), whilst one which allow the spectrum to be recorded on a detector is called a 'spectrograph'. The catch-all term for any instrument which permits measurement of an electromagnetic spectrum is 'spectrometer' (Ball 2006, p2). However, these terms are generally used interchange-

ably; throughout this thesis the term ‘spectrograph’ is used.

2.2.1 The basic optical spectrograph

The three basic operations which a spectrograph must perform are: isolate the light from the object of interest, separate the wavelengths of the light to form a spectrum, and record the spectrum for later analysis. The simplest optical spectrographs consist of five main components:

- A slit or other aperture which is placed at the focal plane. By positioning the object of interest on the slit, its light is allowed to pass into the spectrograph whilst that from other objects in the field-of-view is rejected,
- A collimator, which converts the diverging beam of light behind the focal point into a parallel beam ready for dispersion. This ensures that the angular distribution of any light after dispersion is entirely dependent on its wavelength, and not the part of the primary mirror it originally impinged upon.
- A prism, grating or other dispersive element. These reflect or transmit light in such a way that monochromatic beams of different wavelengths emerge at different angles.
- A camera, which focuses the dispersed light into a new image at a new focal plane.
- A detector, which is placed at the camera’s focal plane and records the intensity of the light at each wavelength.

In the past, the detector might have been a photographic plate, photomultiplier tube or even the human eye. However, in virtually all applications the detector is now a CCD, which is described in section 2.3.2.

2.2.2 Properties of spectrographs

There are a vast number of variations on the basic spectrograph, each of which is optimised for a specific scientific task, together with practical considerations such as mass, size and cost. When selecting a spectrograph for a particular observation, a range of factors must be considered to ensure that the spectrum acquired will have the necessary

properties to achieve the science goals. The key defining properties of spectrographs are:

- The wavelength range. This refers both to the range of possible wavelengths which may be observed (the operating range), and to the wavelength coverage available in a single exposure (the spectral range). In some designs the two may be equal.

- The spectral resolution (or resolving power). This is related to the smallest wavelength difference between two discernible spectral features, and is defined as:

$$R = \frac{\lambda}{\Delta\lambda} \tag{2.2}$$

  where R is the spectral resolution, λ is the wavelength and $\Delta\lambda$ is the smallest separation between two lines which may be distinguished from each other (Kitchin 2009, §4.1.2). By analogy with the angular resolution given in equation 2.1, $\Delta\lambda$ is conventionally taken as the FWHM of the instrumental point spread function*. $\Delta\lambda$ is also referred to as the 'resolution element'.

- The dispersion of the spectrograph. The dispersion D is defined as

$$D = \frac{\mathrm{d}\lambda}{\mathrm{d}x} \tag{2.3}$$

  where x is the physical position on the detector. Intimately linked with the resolution, the dispersion must be high enough so that each resolution element falls on a separate pixel of the detector. However, too high a dispersion will limit the spectral range for a given detector size, and increase the noise by spreading the signal over many pixels. Generally spectrographs are designed such that each resolution element falls on 3–4 pixels to provide robust sampling without adverse effects.

- The throughput of the spectrograph. This is defined as the proportion of photons striking the primary mirror which are actually recorded on the detector. In all designs this depends on the wavelength, and limits the operating range. Because of the multiple optical elements in a typical telescope/spectrograph combination, the peak throughput t is less than about 20%, usually much less. Spectrographs which achieve high resolution tend to have low throughputs, with a general rule of thumb that $Rt \approx$ constant.

*The 'point spread function' is the detected wavelength distribution produced by the spectrograph for a theoretical monochromatic source'

2.3 Data reduction

The final result desired in any spectroscopic observation is a one-dimensional spectrum, giving the intensity of radiation as a function of wavelength (or a related unit such as frequency), which can then be subjected to the tools of spectral analysis. However, the output of a CCD detector is a two dimensional image which gives the the number of 'counts' in each pixel of the detector. The raw output also suffers from a number of instrumental artefacts due to imperfections in the system, and typically consists of many files generated over the course of an observation. The process of transforming the raw data into the desired final form ready for analysis is termed 'data reduction'.

The steps required during data reduction depend on the instrument set-up and the purpose to which the data are to be put. Some stages are only necessary at particularly high resolution or signal-to-noise, whilst others are critical for faint targets but not for bright ones. Some aspects require subjective decision making or may adversely effect the results which are ultimately produced from the data. For these reasons, it is usually the responsibility of the end user (i.e. the astronomer, rather than the observatory) to perform their own data reduction.

2.3.1 Software

In principle, any image manipulation software can be used to perform data reduction. However, a number of purpose-built software packages exist for data reduction. General-purpose data reduction packages such as IRAF (Image Reduction and Analysis Facility*) contain software written to perform each stage of the reduction, but with the flexibility required for application to any data. They also allow stage-by-stage data reduction with the close involvement of the user, which is important for any subjective or particularly sensitive operations.

Other software packages, referred to as 'pipelines', are designed to automate some or all of the data reduction. Generally built on top of existing data reduction packages, pipelines allow much of the time-consuming tedium of data reduction to be avoided. For particularly large datasets, such as large surveys, they may be essential for reduction to be completed on a sensible timescale. However, pipelines have a number of disadvantages. A particular pipeline is only applicable to a specific mode on a particular

*IRAF is distributed by the National Optical Astronomy Observatories, which are operated by the Association of Universities for Research in Astronomy, Inc., under cooperative agreement with the National Science Foundation.

instrument, and since they require substantial software development are only available for some modes/instruments. Because pipelines reduce or remove the involvement of the astronomer from the reduction process, they may not be suitable even when they are available. This includes cases where data requires particular care at some stage of reduction, and it is essential to ensure that the automated pipeline has performed the tasks required correctly. Subjective considerations such as continuum normalisation (see section 2.3.3) cannot be handled by pipelines and must be performed 'by hand'.

Some of the data presented in this thesis have been reduced using pipelines where appropriate, to perform a small part (e.g. section 4.1) or the majority (e.g. chapter 5) of the reduction. Further processing of pipeline data has then been performed by hand in IRAF. Other data (e.g. chapter 3) have been entirely reduced in IRAF.

2.3.2 Charge-coupled devices

The dominant detector in optical astronomy is currently the charge-coupled device (CCD), which has almost completely replaced the earlier use of photographic plates and photomultiplier tubes*. CCDs have a number of characteristics which make them excellent detectors, including high dynamic range, linear response, very high quantum efficiency, broad wavelength coverage (from $\sim$3,000–10,000 Å) and direct output of a 2-dimensional digital image. Despite these features, CCDs are not perfect detectors. A number of artefacts are introduced by the detector which must be removed during the data reduction process. In order to explain these corrections, it is useful to first examine the basic operating principles of the CCD.

A CCD consists of a wafer of doped silicon extrinsic semiconductor with a surface divided into pixels by micro-fabricated electrodes. A typical format for an optical astronomical CCD is 2048×4096 pixels, each of which is 13.5 μm square. When an incoming photon strikes a pixel, it excites an electron from the valence to the conduction band of the semiconductor, leaving behind a hole. This electron-hole pair creation is extremely efficient; science-quality CCDs typically have peak quantum efficiencies of 90% or more, which includes losses due to photons striking the electrodes. The long wavelength cutoff in sensitivity is set by the energy required to excite an electron across the band gap, and the increasing transparency of silicon at longer wavelengths. The short wavelength limit is set by the need for the photon to penetrate the surface layers

*Photomultiplier tubes still survive in some specialist applications, such as high-speed photometers and exposure meters, but are gradually being replaced with CCDs even in these roles

before being absorbed, but in practice this is actually set by the cutoff in atmospheric transmission around 3,200 Å due to the ozone layer.

Once an electron has been excited, it is trapped by a potential well generated by the electrodes. During an integration tens of thousands of electrons may accumulate within each pixel without ill effect, which provides the CCD with its high dynamic range. Once the exposure is complete, a shutter is closed over the CCD and the electrodes are then cycled in such a way that the charge is transferred from one pixel to its neighbour. An amplifier is attached to one corner of the CCD, and each pixel is 'read out' by transferring its accumulated electrons into the amplifier. Because there is generally only one amplifier, the array is read out one pixel at a time by transferring the charges across the final row until they have all been read out, at which point the remaining rows are transferred down a column and read out in turn. Some recent CCDs have two amplifiers, each of which reads out half of the array. Finally, the charges measured by the amplifier are digitised and saved onto a suitable storage medium such as a computer hard disk.

2.3.3 Stages of data reduction

Data reduction is a highly bespoke processes, which must be tailored to the instrument, detector and scientific requirements of the data. Therefore, the stages of data reduction are not universal, and may vary significantly. For example, older CCDs and those aimed at the amateur market must correct for thermal generation of electron-hole pairs, but most professional CCDs are cooled using liquid nitrogen to the point that this correction becomes unnecessary. In this section, the common stages of data reduction are described for the spectroscopic studies presented in this thesis. However, the not all stages were applied for all data, and conversely some data received additional stages of reduction; the ordering of the stages is not always the same either.

Bias and overscan subtraction

The readout amplifiers in CCDs operate with a small DC bias voltage added to the charge read out from the pixels. This optimises the linearity and readout noise of the amplifier, and allows a simpler analogue-to-digital circuit to be used as the data are guaranteed to never be negative. This 'bias' level must be subtracted from the data, and this is generally performed in two stages. A series of exposures with zero integration time are taken and averaged to provide a measure of the bias signal across the CCD, which is then subtracted. Any variation of the bias level with time (which may be caused

by e.g. fluctuations in the detector temperature) are removed using an 'overscan' region. This consists of reading out the detector over more columns than are actually present, which adds an additional overscan region to the images which consists of just the bias signal. The two techniques are used in conjunction to remove both two-dimensional and secular variations in the bias level.

Flat fielding

The quantum efficiency of any CCD is not totally uniform. The detector efficiency depends on the wavelength of the incoming photons, whilst manufacturing defects or ageing make some pixels more or less sensitive than their neighbours. At long wavelengths, the incoming light may penetrate far enough into the silicon to reflect from the back surface, which sets up interference patterns in the chip known as 'fringing'. These effects are removed by illuminating the spectrograph with a bright continuum light source, in the same setup as is to be used for the observations. Variations in pixel sensitivity and fringing are present in these 'flat fields', and may be divided out of the science data.

Cosmic ray rejection

Electron-hole pairs may be generated by the passage of a cosmic ray or other ionising radiation, as well as by photons. Cosmic rays which pass through a pixel may generate hundreds or thousands of pairs, and unless the angle of incidence is perpendicular to the CCD may do so over several neighbouring pixels. The flux of cosmic rays depends on several factors, including the observatory latitude, magnetic storms, and the state of the solar wind. Their signatures are identified through several methods including thresholding, automatic recognition of narrower-than-expected emission spikes, and comparison of multiple exposures taken in succession. The affected pixels are then rejected or are assigned a new value based on interpolation of their neighbours.

Scattered light subtraction

In spite of the best efforts of instrument designers, the interiors of spectrographs are never completely dark. Techniques such as baffles and enclosures are used to isolate the inside of the instrument as much as possible from the light in its surroundings, whilst black cloth or paint is used to absorb as much of the background light as possible. Nevertheless, scattered light is present inside the spectrograph, much of it originating from the fact that no optical components are perfect transmitters or reflectors. This scattered

light background is measured from regions of the CCD away from the spectrum of interest, and any two dimensional structure determined, before being subtracted from the data.

Spectrum extraction

At this point, the only counts remaining in the image are those from the spectrum of interest and the readout noise of the detector (which is stochastic and cannot be removed). The two-dimensional image is converted to a one-dimensional spectrum by summing the counts perpendicular to the direction of the dispersion, over the part of the image which contains the spectrum of the object of interest. Techniques such as 'optimal extraction', which weights the sum by the inverse variance of the signal in each pixel, may be used to maximise the signal-to-noise of the resulting spectrum.

Wavelength calibration

The intensity of the spectrum has now been determined as a function of detector pixels along the dispersion direction, but this must be converted to a function of wavelength. This is achieved by observing a comparison spectrum of an emission line source, usually a hollow cathode arc lamp. The choice of lamp, exposure time and any filter used are made to ensure a number of well-exposed but unsaturated emission lines are present across the entire observed wavelength region. By extracting this spectrum and identifying the lines present, the wavelength may be determined as a function of pixel number and the data converted to a wavelength scale. To compensate for any drift in wavelength during the night, several arc exposures are taken (often before and after each target) and the wavelength solutions interpolated as required.

Telluric line cancellation

The Earth's atmosphere is not a perfect transmitter, and leaves its own spectral signature on the data in the form of 'telluric' absorption lines and night-sky emission lines. Where necessary (for faint sources only) emission lines are subtracted by simultaneous observation of a blank piece of sky. Telluric lines are removed by the observation of a bright source which is known to have a clean continuum in the region of interest, which is normally a nearby unreddened fast-rotating early-type star (such as β Ori or α Vir). The telluric lines are then divided out of the science data; if the signal-to-noise of the science data is not to be compromised the telluric spectrum must have a substantially

higher signal-to-noise itself. The standard star must be observed as quickly as possible before or after the science target, and at similar airmass, such that any variations in atmospheric transmission between the two are minimised.

Continuum normalisation

In order to measure the strength of absorption lines in the final spectrum, it is necessary to normalise the spectrum to the value of the continuum in that region. This can be a particularly subjective stage of data reduction, and any errors introduced will adversely affect the measurements to be made on the absorption lines. Nearby sections of clear continuum are identified and a fitting function used to interpolate the continuum between them. This operation is particularly difficult when there is little clear continuum or the signal-to-noise of the data is low. At this stage, the data reduction is complete and the spectrum may now be subjected to the tools of spectral analysis and measurements taken.

Chapter 3

High spectral resolution studies of very small-scale structure

Very high spectral resolution is a excellent tool for the study of small-scale structure (SSS) in the interstellar medium because it allows absorption due to several clouds along a line-of-sight to be separated. Combined with observations made at multiple epochs, this allows time-variable components to be recognised even when there is significant absorption in other non-variable clouds. Furthermore, the conditions within a cloud may be determined without averaging over all clouds along the line-of-sight. However, obtaining the high signal-to-noise ratios required for SSS studies at very high resolution is challenging, and limits the application of the technique to lines-of-sight towards nearby bright stars.

In a review of known variable optical interstellar absorption lines, Crawford (2003) called particular attention to the line-of-sight towards κ Vel, because the variations observed over eight years were large ($> 40\%$), very small scale (~ 10 AU) and could not be related to any known foreground shell or bubble. In this chapter, new ultra-high resolution observations of κ Vel are presented, which probe the physical and chemical conditions in this small-scale structure on scales ~ 10 AU.

3.1 Background

κ Velorum (HD 81188) is a bright $V = 2.46$ star located at the base of the 'sail' of Vela, and forms the head of the False Cross asterism. It is a single-lined spectroscopic binary with an orbital amplitude of $46.5\,\mathrm{km\,s^{-1}}$ and period of 117 days (Pourbaix et al. 2004); the primary is a B2 IV, whilst the secondary is unknown but faint enough to have

escaped direct detection. The distance to the system obtained from its trigonometric parallax is 165 ± 13 pc (ESA 1997), whilst the reddening is $E_{(B-V)} = 0.10$ (using the intrinsic colours of Fitzgerald 1970). Early high-resolution observations of the ISM towards this star taken in 1989 and 1994 were presented by Crawford (1991) and Dunkin and Crawford (1999) respectively.

Small-scale structure towards κ Vel was first noted by Crawford et al. (2000), who serendipitously discovered that the equivalent width of the interstellar K I line had increased by ∼ 40 per cent between 1994 and 2000, with a concurrent smaller increase in the Na I equivalent width. An instrumental origin for the variations was ruled out, and the enhancement was found to be in a single narrow ($b = 0.24\,\mathrm{km\,s^{-1}}$) absorption component located near $v_{\mathrm{helio}}{}^{*} = +8.5\,\mathrm{km\,s^{-1}}$. The observations were interpreted as indicating that as the proper motion of κ Vel carried it ∼ 15 AU tangentially between 1994 and 2000, the line-of sight was gradually entering a filament of cold and/or dense material aligned along the line-of-sight, of the type proposed by Heiles (1997).

Follow-up observations by Crawford (2002) detected Ca I and CH in the same absorption component, and found a continued increase in the K I column density. Through a consideration of the Ca I/Ca II ratio, CH abundance and stellar proper motion, Crawford (2002) concluded that the absorbing material lay in a cool ($T \sim 100\,\mathrm{K}$), dense ($n_{\mathrm{H}} \gtrsim 10^3\,\mathrm{cm^{-3}}$) cloud with approximate dimensions of 100–1000 × 15 AU aligned along the line of sight.

Consideration of this cloud prompted Bell et al. (2005) to develop a chemical model of such a filament. Bell et al. calculated the column density of several atomic and molecular species within a cloud with physical extent similar to that inferred by Crawford (2002) (illustrated in figure 3.1) as a function of time, radiation field and density. The best-fitting models were for a young (∼ 50 yr), transient (lifetime < 100 yr), high density ($n_{\mathrm{H}} > 10^4\,\mathrm{cm^{-3}}$) filament immersed in a typical ambient radiation field. The models predicted detectable column densities of additional diatomic molecules could be present, including C_2 and OH.

Because C_2 is a homonuclear diatomic molecule, it does not have a permanent electric dipole moment and therefore cannot undergo electric dipole allowed pure rotational transitions. This means that there are no detectable radio lines from this molecule. However, it also prevents the rotational temperature from relaxing on timescales which are short compared to the mean time between collisions in diffuse clouds, as occurs for e.g.

*All velocities quoted in this chapter are heliocentric, and for brevity are hereafter designated in the text by *v* without subscript

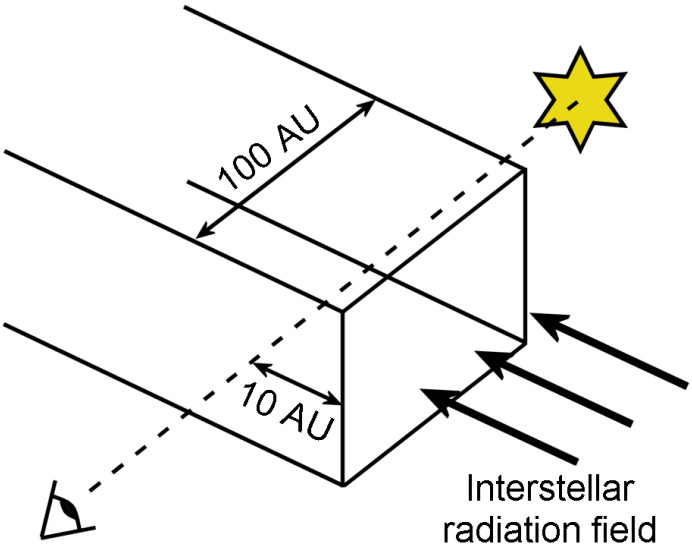

Figure 3.1 – Geometry assumed in the chemical model of Bell et al. (2005)

CN*. In the absence of an applied radiation field, the rotational temperature of C_2 is therefore equal to the local kinetic temperature, because the two equilibrate via collisions. When an external radiation field (such as the ISRF) is applied, rotational states may also be populated during absorption of a photon; if the field can be approximated by a black-body then the populations will be distributed according to the radiation temperature. The overall populations are the sum of two Boltzmann distributions at the two temperatures – the kinetic temperature dominates for low-J states, whilst the radiation temperature dominates for high-J states. If the relative populations of the C_2 rotational levels are found from rotational structure in electronic transitions, both the local kinetic and radiation temperatures may be derived.

Previous determinations of kinetic temperatures within small-scale structures have relied on line widths (which provide only an upper limit) or indirect indicators such as depletions. Observations of C_2 therefore provide the opportunity to constrain chemical models and to obtain the first direct measurement of temperature within a small-scale structure filament.

*The CN rotational temperature relaxes to that of the cosmic microwave background, which provided the earliest estimate (2.6 K) of the temperature of the CMB

Table 3.1 – Summary of the observations towards κ Vel. Exp time is the total exposure time, S/N is the resulting continuum signal-to-noise ratio and W is the measured total equivalent width. Errors are 1σ, the C_2 upper limit is 3σ in each of the five lines which fall in the observed wavelength region.

	UT date	Exp time (hrs)	S/N	W (mÅ)
Ca I	2006 March 10	4.0	360	1.11 ± 0.02
Ca II	2006 March 11	0.5	160	23.1 ± 0.1
K I	2006 March 09,10	2.75	200	7.7 ± 0.2
Na I	2006 March 11	0.67	180	60.3 ± 0.2
CH	2006 March 09,11	9.0	600	0.31 ± 0.03
C_2	2006 March 12-15	15.0	550	< 0.11

3.2 Observations & results

Observations of interstellar absorption towards κ Vel were made on the nights of 2006 March 9–15 using the Ultra-High Resolution Facility (UHRF, Diego et al. 1995) located at the Coudé focus of the 3.9 m Anglo-Australian Telescope. The observers were S Fossey (UCL), A Smith (Nottingham) and J Russell (Nottingham). Data reduction and analysis were performed by the author.

A summary of the observations is presented in table 3.1. New observations of the absorption lines of the atomic species Ca I, Ca II, K I and Na I were obtained, along with the $A^2\Delta \leftarrow X^2\Pi$ (0,0) band of the CH molecule in the $R_2(1)$ Λ-doublet (comprising the $R_{fe}(1/2)$ and $R_{ff}(1/2)$ lines). A search was performed for the C_2 molecule in several low-J lines (R(0), Q(0), Q(2), Q(4) and P(2)) of the $A^1\Pi_u \leftarrow X^1\Sigma_g^+$ (2,0) Phillips band, which were covered in a single instrument set-up.

The detector used for the atomic lines and CH was the blue-optimised EEV2 CCD (2048×4096 13.5 μm pixels). The EEV2 was operated in normal readout mode, which provides an RMS readout noise of 3.2 e^-/pixel and a total readout time of 180 seconds. Because the image slicer (see below) projects the spectrum onto ∼ 1400 unbinned pixels, the EEV2 was binned by a factor of eight perpendicular to the dispersion to reduce the readout noise and time. The EEV2 CCD suffers from severe fringing at wavelengths longwards of ∼ 6500 Å, which particularly affected the K I observations, necessitating careful flat-fielding.

For the C_2 observations the red-optimised MITTL3 CCD (2048×4096 15 μm pixels)

was used due to its higher quantum efficiency and lower fringing at long wavelengths. As the MITTL3 detector cannot be binned it was operated in slow readout mode, which provides a readout noise of 1.8 e^-/pixel and a total readout time of 300 s.

The UHRF was operated in 'R = 1E6' mode, which provides the highest resolution available on any common-user optical astronomical spectrograph, which is vital to resolve narrow interstellar lines. Wavelength calibration was achieved using a comparison Th-Ar arc lamp, whilst flat fields were obtained using the internal quartz-halogen calibration lamp. In this resolution mode the instrument resolves the lines from the arc lamp, so a stabilised He-Ne laser was used to measure the instrumental resolution. The resolving power (see section 2.2.2) was found to be $R = 845,000$ for the EEV2 and $R = 940,000$ for the MITTL3, corresponding to velocity resolutions of 0.355 and 0.319 km s^{-1} respectively.

Individual exposures were limited to 30 min to prevent degradation of the instrumental resolution by the changing heliocentric velocity correction due to the rotation of the Earth. The detector readout times therefore constituted a significant overhead, and detector readout noise made a significant contribution to the total noise level.

As is usual for the UHRF, an image slicer was used to improve the throughput of the instrument. The UHRF image slicer reformats a $1.5 \times 1.5''$ entrance aperture to a $0.06''$ slit, but has a peak throughput of only 15%. Observing conditions were clear on the nights of 9 and 15 March, but those of 10–14 March were frequently interrupted by cloud and fog. The seeing during the observations varied in the range 1–3″, and was mostly around 1.5″.

Data reduction was performed using the `noao.onedspec` routines in IRAF. Pixel-to-pixel sensitivity variations and fringing were removed via division by a normalised flat-field. The scattered light background was measured from the inter-order regions and subtracted. The Na I, Ca I, K I, CH and C_2 observations were corrected for telluric absorption by division by a well-exposed spectrum of a bright fast-rotating early-type standard star (α Vir, β Ori or α Eri); the Ca II observations were found to be free of telluric contamination. The individual exposures were converted to a heliocentric reference frame before being co-added to prevent degradation of the resolution and converted to a velocity scale. The resulting spectra are shown in figures 3.2–3.6; the measured continuum signal-to-noise ratios and equivalent widths are given in table 3.1.

The continuum signal-to-noise ratio in the region of the C_2 lines was 550, but no lines were detected, with a 3σ upper limit of 0.11 mÅ on each of the five rotational lines falling in the observed wavelength region. At the relatively high gas densities inferred

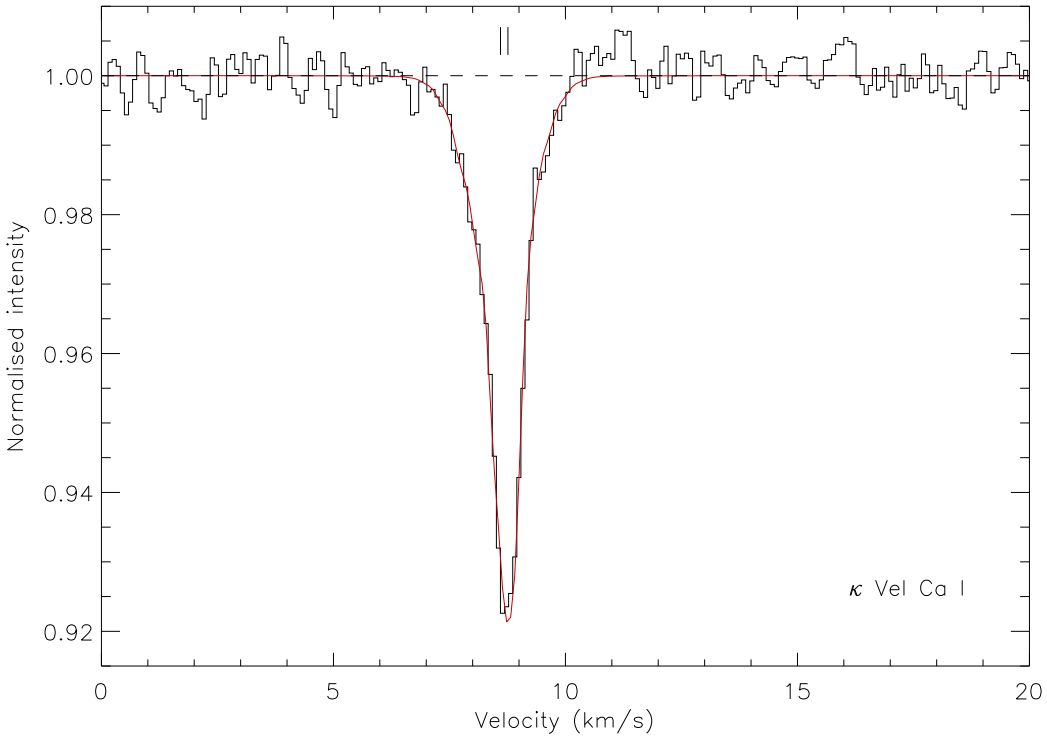

Figure 3.2 – The interstellar Ca I absorption observed towards κ Vel. The black histogram is the observed spectrum, whilst the red line is the fitted model profile. The dashed line indicates the continuum level, whilst the tick marks indicate the positions of each absorption component listed in table 3.3. The velocity scale is heliocentric.

by Crawford (2002) and Bell et al. (2005), populations of the low-J states of C_2 should follow an approximately thermal distribution. Assuming a distribution corresponding to a temperature of 100 K and integrating over all J states, an upper limit on the C_2 column density of $\lesssim 10^{12}$ cm^{-2} is obtained. This is identical to the upper limit derived by Bell et al. (2005) for observations in 2003.

3.3 Line profile analysis

The line profiles of the detected species were modelled using the VAPID interstellar line modelling program (Howarth et al. 2002), which computes the optimum column density N, velocity v and Doppler broadening parameter b^* for a given set of absorption components using a χ^2 minimisation algorithm. Individual absorption components have

*The broadening parameter is related to the FWHM of the corresponding Gaussian distribution by $b = \frac{\mathrm{FWHM}}{2\sqrt{\ln 2}}$

		Wavelength (Å)	f
Ca I		4226.728	1.77
Ca II K		3933.6614	6.267×10^{-1}
K I		7698.9586	1.248×10^{-1}
		7698.9681	2.079×10^{-1}
Na I D_1		5895.9109	1.200×10^{-1}
		5895.9322	2.001×10^{-1}
CH	$R_{ff}(1/2)$	4300.3235	2.53×10^{-3}
	$R_{fe}(1/2)$	4300.3030	2.53×10^{-3}
C_2	R(0)	8757.682	1.4×10^{-3}
	Q(2)	8761.190	1.4×10^{-3}
	Q(4)	8763.740	1.4×10^{-3}
	Q(6)	8767.750	1.4×10^{-3}
	P(2)	8766.031	1.4×10^{-3}

Table 3.2 – Adopted atomic and molecular line data. Wavelengths λ and oscillator strengths f are taken from Morton (2003, 2004) for the atomic species, Black and van Dishoeck (1988) for CH and van Dishoeck and de Zeeuw (1984) for C_2. The Na I and K I lines exhibit hyperfine structure, whilst C_2 and CH each have several observed lines; each transition is listed separately. For the hyperfine transitions, oscillator strengths have been apportioned in a 5:3 ratio according to the prescriptions of Welty et al. (1994).

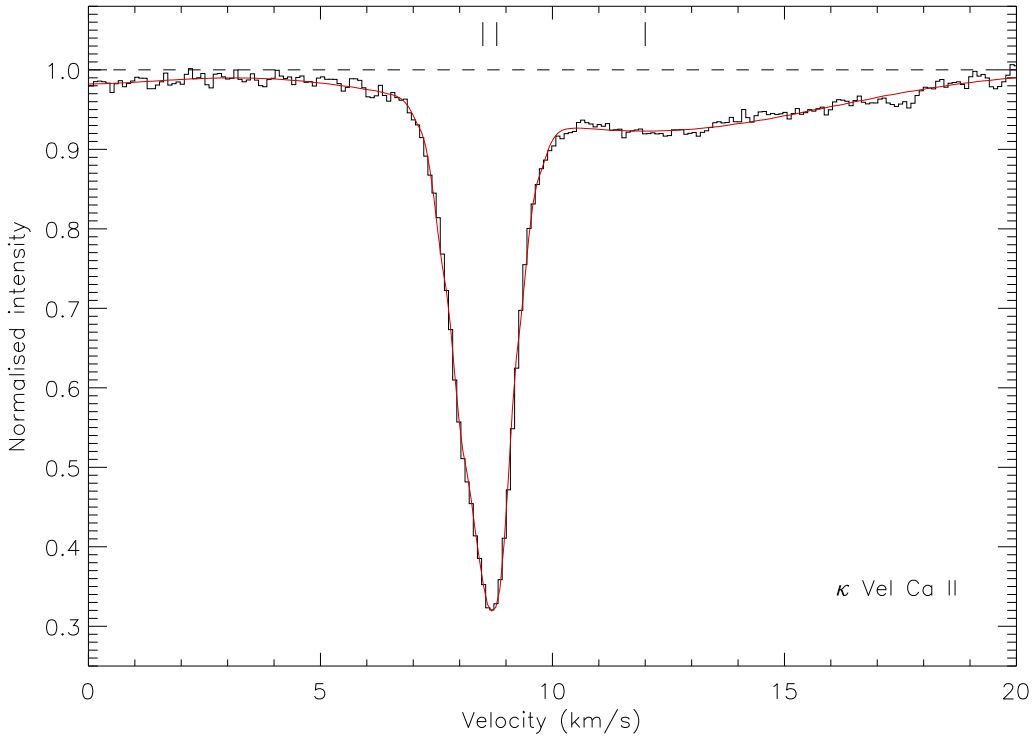

Figure 3.3 – The interstellar Ca II K absorption observed towards κ Vel. The black histogram is the observed spectrum, whilst the red line is the fitted model profile. The dashed line indicates the continuum level, whilst the tick marks indicate the positions of each absorption component listed in table 3.3. The velocity scale is heliocentric.

a Voigtian profile formed by the convolution of the Lorentzian natural line shape, the instrumental point-spread-function (here taken to be Gaussian with widths given by the velocity resolution found in section 3.2) and a Gaussian with broadening parameter *b*. Rigorous error estimates were obtained from 1,000 Monte-Carlo noise simulations, in which Gaussian noise corresponding to the measured signal-to-noise ratio was added to the data and the fits repeated. The lower signal-to-noise present in the cores of the lines due to the lower number of photons detected was taken into account during the modelling process, under the assumption of Poissonian noise statistics.

The wavelengths and oscillator strengths adopted in the analysis are given in table 3.2, and were taken from Morton (2003, 2004) for the atomic species, Black and van Dishoeck (1988) for CH and van Dishoeck and de Zeeuw (1984) for C_2. The CH rotational lines form a Λ-doublet split by $1.43\,\mathrm{km\,s^{-1}}$; the velocities output by VAPID are with respect to the bluest transition, and were converted to the weighted mean of the two lines by subtraction of $0.72\,\mathrm{km\,s^{-1}}$. Similarly, K I and Na I D_1 exhibit nuclear

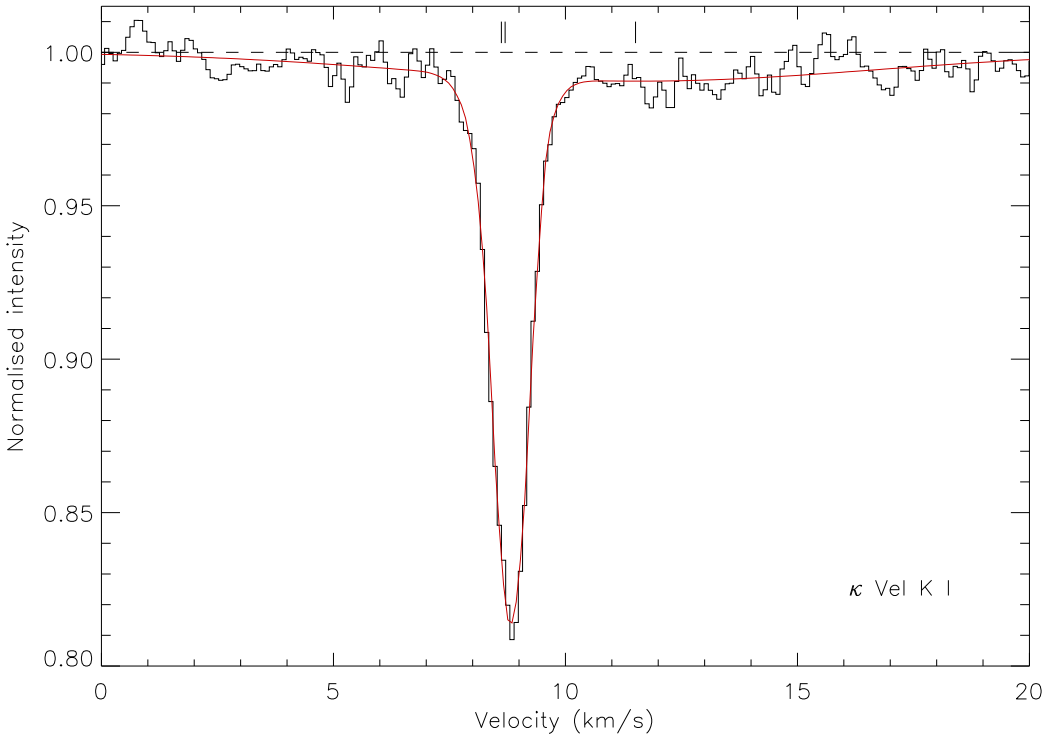

Figure 3.4 – The interstellar K I absorption observed towards κ Vel. The black histogram is the observed spectrum, whilst the red line is the fitted model profile. The dashed line indicates the continuum level, whilst the tick marks indicate the positions of each absorption component listed in table 3.3. The velocity scale is heliocentric and relates to the weighted mean transition wavelength.

hyperfine splitting, into two lines separated by 0.35 km s^{-1}and 1.04 km s^{-1} respectively. For both K I and Na I the statistical weights of the transitions (given by $2F + 1$ in the lower state, where F is the vector sum of the nuclear and electronic angular momenta) are in the ratio of 5:3, where the stronger transition is the redder of the pair (see Welty et al. 1994; Morton 2003). The VAPID output velocities were converted to the weighted mean velocity of the transitions by the subtraction of 0.22 km s^{-1} and 0.65 km s^{-1} for K I and Na I respectively. The results of the fitting are presented in table 3.3

There has been some discussion in the literature as to whether the main absorption peak toward κ Vel at around 9 km s^{-1} represents one or two separate absorption components. Dunkin and Crawford (1999) and Crawford et al. (2000) argue that their data indicate two components, whilst Crawford (2002) identifies only a single component. While modelling the atomic species, it was found that a single component did indeed give an adequate fit, but that a two-component model was significantly better in all

Species	$v_{\rm helio}$ (km s^{-1})	b (km s^{-1})	log N (cm^{-2})	$T_k^{\rm ul}$ (K)
Ca I	^{A}8.60 ± 0.03	0.86 ± 0.05	9.41 ± 0.03	1800 ± 200
	^{B}8.76 ± 0.01	0.28 ± 0.02	9.20 ± 0.05	190 ± 30
Ca II	−0.27 ± 0.18	2.80 ± 0.20	10.12 ± 0.03	-
	^{A}8.50 ± 0.01	0.75 ± 0.01	11.24 ± 0.01	1400 ± 40
	^{B}8.80 ± 0.01	0.28 ± 0.01	10.52 ± 0.02	190 ± 30
	12.00 ± 0.07	5.51 ± 0.08	11.08 ± 0.01	-
K I	^{A}8.62 ± 0.04	0.65 ± 0.05	10.09 ± 0.05	1100 ± 200
	^{B}8.70 ± 0.02	0.30 ± 0.02	10.22 ± 0.03	230 ± 30
	11.51 ± 0.43	7.14 ± 0.54	10.24 ± 0.03	-
Na I	^{A}8.49 ± 0.01	0.69 ± 0.01	11.88 ± 0.01	660 ± 20
	^{B}8.75 ± 0.01	0.29 ± 0.02	11.33 ± 0.03	120 ± 20
	12.25 ± 0.04	1.32 ± 0.10	10.93 ± 0.05	-
	13.72 ± 0.69	4.87 ± 0.52	11.01 ± 0.09	-
CH	8.77 ± 0.23	2.06 ± 0.56	11.47 ± 0.05	-

^{A} component A, ^{B} component B

Table 3.3 – Results of the line profile analysis for κ Vel. The heliocentric velocity $v_{\rm helio}$, Doppler broadening parameter b and column density N are given for each model component. The total line profiles are plotted in figures 3.2–3.6. $T_k^{\rm ul}$ is the upper limit on the kinetic temperature calculated from Equation 3.2 assuming no turbulent contribution to the b-value. Heliocentric velocities are quoted with respect to the weighted means of the individual transitions. All uncertainties are 1σ.

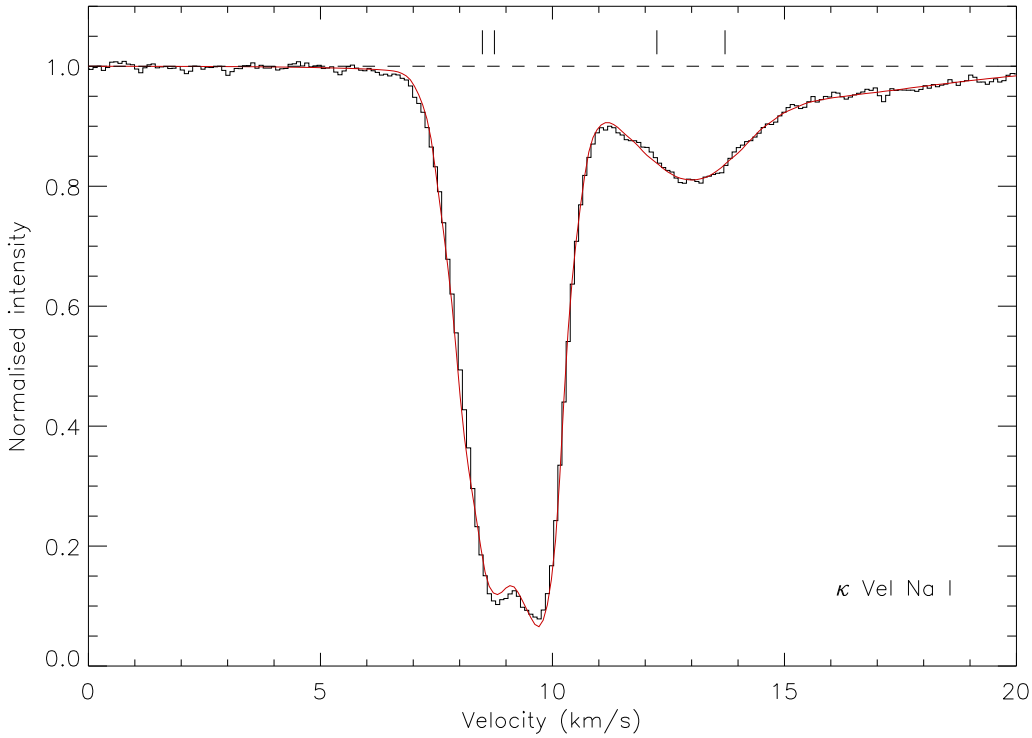

Figure 3.5 – The interstellar Na I D_1 absorption observed towards κ Vel. The black histogram is the observed spectrum, whilst the red line is the fitted model profile. The dashed line indicates the continuum level, whilst the tick marks indicate the positions of each absorption component listed in table 3.3. The velocity scale is heliocentric and relates to the weighted mean transition wavelength.

cases. This was confirmed via a statistical F-test, which compares the goodness-of-fit (here measured by χ^2) for models with varying numbers of degrees of freedom.

For each additional cloud included in the model, an extra three degrees of freedom (N, v and b) are introduced. The F-test computes the F-statistic

$$F = \frac{\chi_1^2}{\chi_2^2}. \tag{3.1}$$

The F-statistic follows an F-distribution under the null hypothesis that the extra degrees of freedom are not producing a statistically significant improvement in χ^2. There will always be an improvement in χ^2 when more degrees of freedom are introduced, even if they are only providing a closer fit to the noise. The null hypothesis is rejected (i.e. the improvement in χ^2 is statistically significant) when the F-statistic is larger than expected given the number of degrees of freedom. 'Larger than expected' is defined as an outlier on the F-distribution to some given level of confidence, such that the F-

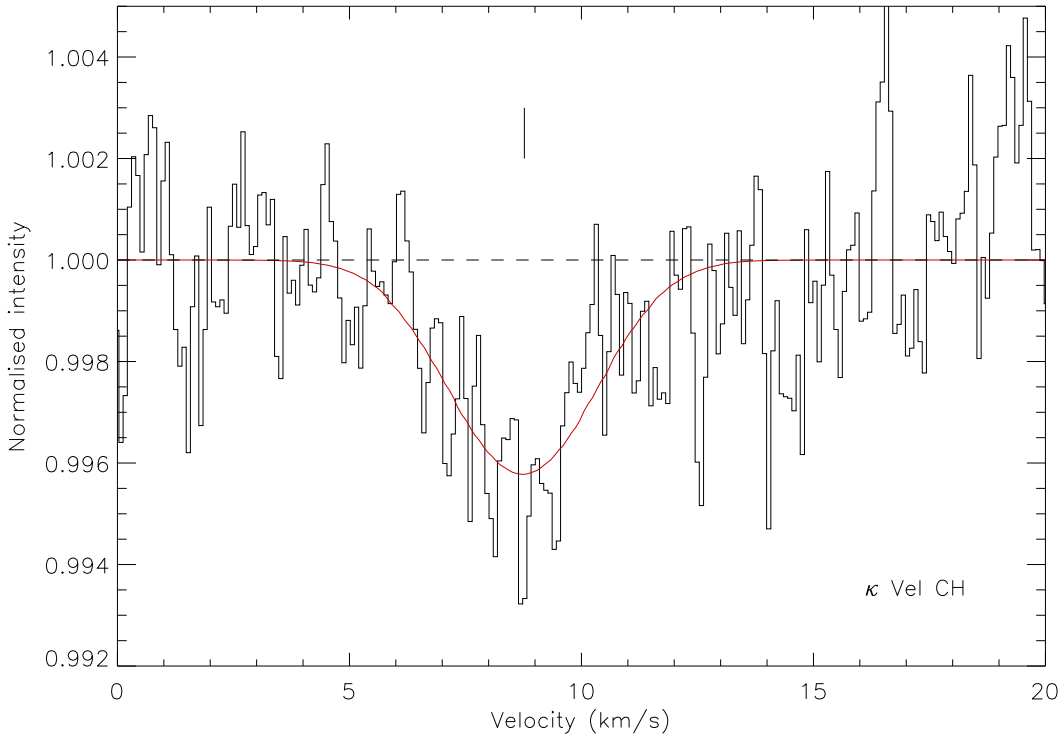

Figure 3.6 – The interstellar CH absorption observed towards κ Vel. The black histogram is the observed spectrum, whilst the red line is the fitted model profile. The dashed line indicates the continuum level, whilst the tick mark indicates the position of the absorption component listed in table 3.3. The velocity scale is heliocentric and relates to the mean transition wavelength.

statistic is greater than some critical value. Because the F-distribution is a complicated function, and the critical value depends on both numbers of degrees of freedom, critical values are tabulated in various textbooks on statistics. Here, the critical values were taken from the tables of the NIST/SEMATECH e-Handbook of Statistical Methods*.

The F-test found that the two component model was significantly better at the 95% level for all the atomic species except K I, for which the significance was still > 90%. The similarities in the v and b values obtained for each species, which were derived independently, reinforces the interpretation that a two component model is justified by the new high signal-to-noise data.

In each of the atomic species, the absorption around $9\,\mathrm{km\,s^{-1}}$ contains a narrow component at $v \sim 8.6\,\mathrm{km\,s^{-1}}$ with $b \sim 0.7\,\mathrm{km\,s^{-1}}$ (hereafter referred to as component A) and a slightly higher velocity even narrower component at $v \sim 8.8\,\mathrm{km\,s^{-1}}$ with

*`http://www.itl.nist.gov/div898/handbook/`, section 1.3.6.7.3

$b \sim 0.3\,\mathrm{km\,s^{-1}}$ (hereafter component B). These components are consistent with the previously reported two-component b values of Crawford et al. (2000), though at slightly shifted velocity. All of the atomic species except Ca I also include a broader absorption component at $\sim 12\,\mathrm{km\,s^{-1}}$; this component was seen in Ca II and K I by Crawford (2002), but only included in his Ca II model. The core of the Na I model is not a perfect fit to the data, due to the lower signal-to-noise ratio present at the centre of this almost-saturated line, though may indicate a small uncertainty in the zero absorption baseline.

Although the velocities and b values of the two main absorption components are broadly consistent between atomic species, their exact velocities and the velocity separation of the two components are not. The velocity separations between components A and B are consistent with the uncertainties for K I and Ca I, but the separations for Ca II and Na I are almost twice as large. The small wavelength coverage of the UHRF (4–9 Å) results in a small number of arc lines for wavelength calibration, which limits the absolute accuracy, particularly in the case of C_2 for which only four lines were available. The magnitude of this effect can be estimated from the RMS of the wavelength fit, which was always less than $0.01\,\mathrm{km\,s^{-1}}$. Velocity shifts *between* observations of a few tenths of a $\mathrm{km\,s^{-1}}$ have been seen in previous UHRF data (e.g. Crawford et al. 2000) and are thought to result from slight differences between the light paths of the telescope and arc lamp beams. This problem may have been exacerbated by the infrequent use of the instrument. Nevertheless, the *relative* velocities within the same observation remain secure; the varying separation between the broad and narrow components may indicate intrinsic unresolved structure within the absorbing material (see section 3.4.3). Both Na I and Ca II may be formed in warmer regions than K I and Ca I, so the differences may indicate that these species also arise from an outer warmer layer in the absorbing cloud.

Although it might be expected that the CH would follow the same distribution as the atomic species, perhaps with enhancement in the cooler (and presumably denser) component, no evidence for this has been found. There is no statistically significant evidence for more than one absorption component, though this may be due to the weakness of the absorption. The CH absorption has been fitted with a single broad ($b = 2.06\,\mathrm{km\,s^{-1}}$) absorption component, albeit with a high uncertainty ($\sigma b = 0.56\,\mathrm{km\,s^{-1}}$), as shown in figure 3.6. Visual inspection of the CH spectrum shows no sign of the expected Λ-doubling. However, Λ-doubling can be clearly seen in theoretical models with $b = 0.7\,\mathrm{km\,s^{-1}}$, even when degraded by addition of the obtained noise level, which

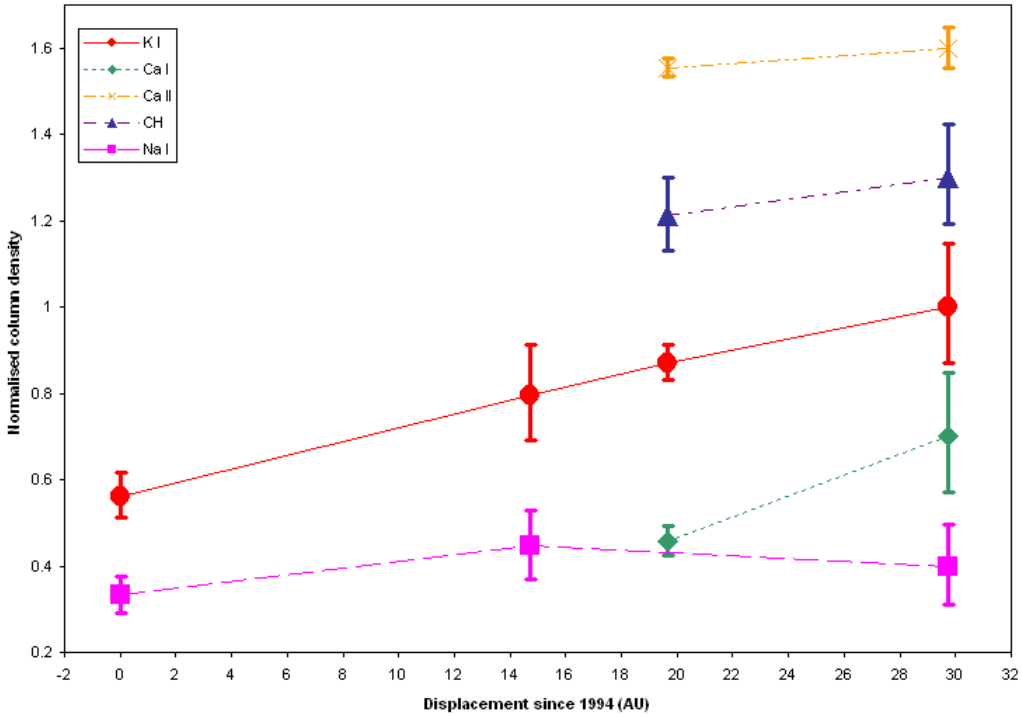

Figure 3.7 – Comparison of observed column densities of interstellar absorbers towards κ Vel since 1994. Total column densities in the one or two components located at ~9 km s^{-1} in 2006 (this work), 2002 (Crawford 2002), 2000 and 1994 (Crawford et al. 2000) are plotted. Data have been normalised with respect to the 2006 values and vertical offsets of 0.3 between species applied for display; lines have been added to guide the eye only. All species except Na I show increases over scales of < 30 AU.

implies that the profile is not as narrow as seen in the atomic lines and is not merely masked by the weak detection. Although the velocity of the absorption is closest to that of component B, the uncertainty and variations between species are large enough that an origin in component A cannot be ruled out.

3.4 Discussion

3.4.1 Comparison to previous observations

A direct comparison between the observations taken at different epochs is difficult, because the absorption has been modelled with different numbers of components. Fortunately, all the observations considered here utilised the same instrument at essentially

the same resolution (850,000–900,000). In figure 3.7, the components reported in Crawford et al. (2000), Crawford (2002) and this work are compared by summing the column densities of the one or two components which make up the absorption at $\sim 9\,\mathrm{km\,s^{-1}}$. However, the differing treatments of the higher velocity absorption may affect this comparison. For example, the K I component found at $11.51\,\mathrm{km\,s^{-1}}$ in this work overlaps the $\sim 9\,\mathrm{km\,s^{-1}}$ absorption, but was not included in the model of Crawford (2002). This has the effect of reducing the rise in column density seen in this work.

Notwithstanding these difficulties, figure 3.7 shows clear increases in all of the species except Na I, though in many cases the increases are not large compared to the uncertainties. This may be an artefact of the two component fits – the uncertainties in the total $\sim 9\,\mathrm{km\,s^{-1}}$ column densities were obtained by summing those for the two components in quadrature, but these are clearly not independent quantities. This may explain why the uncertainties for the 2002 data shown in figure 3.7 are smaller than for the present work, despite the higher signal-to-noise achieved here. It would be beneficial to re-model the earlier data using the same components as were found in this work to facilitate a more direct comparison.

3.4.2 Line widths and temperature

Although the intention of the observations was to measure the kinetic temperature from the rotational populations of C_2, the lack of a detection of this species necessitates the use of another method for determining the local kinetic temperature. In addition to the instrumental resolution and the natural line width, the two mechanisms which act to broaden interstellar lines are thermal Doppler broadening and turbulent bulk motions of the gas. These are related to the Doppler broadening parameter b by:

$$b = \sqrt{\frac{2k_B T_k}{m_A} + v_t^2} \tag{3.2}$$

where k_B is the Boltzmann constant, T_k is the kinetic temperature, m_A is the atomic (or molecular) mass of the species and v_t is the RMS turbulent velocity. By taking the limiting case of zero turbulent velocity, a rigorous upper limit on the kinetic temperature T_k^{ul} may be obtained. Such limits have been calculated for each component of each species, the results for those components with $T < 2,000\,\mathrm{K}$ are given in table 3.3. The actual kinetic temperature is likely to be somewhat lower than these limits.

In principle, it should be possible to separately determine T_k and v_t by simultaneously solving equation 3.2 for species with differing values of m_A. However, inspection

of table 3.3 shows that for component A the b values for Na I ($m_A = 23$) and Ca II ($m_A = 40$) are identical; the b-value for K I is actually lower than Ca II, however if the two are spatially coexistent the opposite should be true. For component B, the b-values increase with lower atomic mass as expected, but do so *faster* than the limiting case of zero turbulence.

Ca II is often observed to have a significantly broader profile than Ca I and Na I in many high-resolution studies of the ISM. This is usually interpreted as due to Ca II being present in a warmer and/or more turbulent part of the cloud to the neutral species, presumably in the outer regions (e.g. Price et al. 2000; Welty et al. 2003). This effect may be occurring in the cloud toward κ Vel, which would mean that the species are not entirely spatially coexistent.

3.4.3 Ca I / Ca II ratio and electron density

At the low densities prevalent in the diffuse ISM, the balance between the various ionisation states of a single atom is set by the competition between photoionisation which promotes the atom to a higher ionisation state, and recombination with an electron which demotes it to a lower one. For the neutral and first ionised state in equilibrium, this may be expressed as:

$$\Gamma(\mathrm{X\,I})\, n(\mathrm{X\,I}) = \alpha_r(\mathrm{X\,I}, T)\, n(\mathrm{X\,II})\, n_e \tag{3.3}$$

where Γ is the photoionisation rate, α_r the radiative recombination rate coefficient, n_e the electron number density and n the number density, for element X. The left hand side of equation 3.3 represents the ionisation rate and the right hand side represents the recombination rate. As observations reveal the column density N and not the number density n, it is necessary to assume a constant density along the line of sight, allowing n to be replaced by N. Under this assumption, and for the specific case of calcium, this becomes:

$$n_e = \frac{\Gamma(\mathrm{Ca\,I})}{\alpha_r(\mathrm{Ca\,I}, T)} \frac{N(\mathrm{Ca\,I})}{N(\mathrm{Ca\,II})}. \tag{3.4}$$

Calcium is an unusual case because both its first and second ionisation energies are less than the Rydberg energy (6.11, 11.87 and 13.6 eV respectively), so in diffuse clouds ionisation to Ca III is possible. There is then a second ionisation equilibrium between Ca II and Ca III, though this does not invalidate the electron densities derived from equation 3.4. Welty et al. (2003) calculated the relative populations of Ca I, Ca II

and Ca III and found that the dominant ionisation state is Ca II in any situation where Ca I is strong enough to be detected.

Equation 3.4 is however an approximation, and assumes that no other processes cause conversion between ionisation stages at significant levels. Plausible processes include cosmic ray ionisation and charge exchange with dust grains or PAHs (e.g. Liszt 2003). Welty et al. (2003) have discussed this issue at length in the context of calcium ionisation ratios, and concluded that equation 3.4 remains valid if the fractional ionisation $n_e/n_H \lesssim 2 \times 10^{-4}$, which is the level provided by complete ionisation of gas-phase atomic carbon to C II (assuming standard depletions). Those authors also conclude that the assumption of photoionisation is most valid when n_e is high. Since the SSS observations indicate a cloud which is much cooler and/or denser than usual for the diffuse ISM, and the low extinction present in the cloud* favours photoionisation, the assumptions leading to equation 3.4 seem to be valid in this case.

Under these assumptions, the electron density may then be determined straightforwardly from the column densities and the value of $\Gamma/\alpha_r = 66$ for Ca I given by Welty et al. (2003, their table 3), which assumes $T = 100\,\mathrm{K}^{\dagger}$. The values of the electron density are then found to be $n_e^A = 0.98 \pm 0.13\,\mathrm{cm}^{-3}$and $n_e^B = 3.16 \pm 0.72\,\mathrm{cm}^{-3}$ for components A and B respectively. These are very high electron densities for diffuse clouds. In comparison, Crawford (2002) found $n_e = 0.97\,\mathrm{cm}^{-3}$ using a single-component model.

3.4.4 Other line ratios

Whilst the Ca I/Ca II ratio provides a measure of the electron density (under the assumption of constant temperature), other line ratios are sensitive to other properties of the interstellar gas.

Because the depletion of potassium into dust grains is thought to be fairly constant, the Ca I/K I ratio may be used to estimate the depletion of calcium, which is typically very high at the low temperatures in the diffuse ISM due to its high condensation temperature ($T_C = 1659\,\mathrm{K}$, Lodders 2003). Adopting the same assumptions as for the calcium ionisation balance, the relative populations of Ca I and K I are given by:

$$\frac{N(\mathrm{Ca\,I})}{N(\mathrm{K\,I})} = \frac{(\Gamma/\alpha_r)_{\mathrm{Ca\,I}}}{(\Gamma/\alpha_r)_{\mathrm{K\,I}}} \frac{\delta(\mathrm{Ca})a_{\mathrm{Ca}}}{\delta(\mathrm{K})a_{\mathrm{K}}} \tag{3.5}$$

*$E_{(B-V)} = 0.10$, so $A_V = 0.16$ halfway through the line-of sight, assuming $R_V = 3.1$

†For calcium, the dependence of α_r on T is $\alpha \propto (T/100\,\mathrm{K})^{-0.683}$, which is fairly weak (Pequignot and Aldrovandi 1986)

where $\delta(X)$ are the gas-phase fractions and a_X are the cosmic abundances. Assuming $\delta(\mathrm{K\,I}) = 0.2$ and taking standard abundances, photoionisation and recombination rates from Welty et al. (2003), this becomes

$$\frac{N(\mathrm{Ca\,I})}{N(\mathrm{K\,I})} \approx 12.4\delta(\mathrm{Ca}). \tag{3.6}$$

This results in estimates of the calcium depletion in components A and B of $\delta(\mathrm{Ca})^A = 0.0168$ and $\delta(\mathrm{Ca})^B = 0.0955$ ($D(\mathrm{Ca})^A = -1.77$ and $D(\mathrm{Ca})^B = -1.02$, where D are the logarithmic depletions).

The Ca I/K I ratio is also correlated with the fraction of hydrogen in the form of H_2, though the relation is not particularly tight (Welty et al. 2003). Previous observations have resulted in upper limits only for the H I and H_2 column densities towards κ Vel (Jenkins 2009). Perhaps surprisingly, the Ca I/K I ratio is higher in component A than component B, despite the lower electron density and higher b-value. The measured ratios are $\log(N(\mathrm{Ca\,I})/N(\mathrm{K\,I}))^A = 0.42$ and $\log(N(\mathrm{Ca\,I})/N(\mathrm{K\,I}))^B = 0.19$. Comparing with figure 4 of Welty et al. (2003), these correspond to upper limits on the fraction of hydrogen in the form of H_2 of $f(H_2) \lesssim 10^{-3}$, in both components. This is a very low molecular hydrogen fraction for the diffuse ISM, let alone regions with enhanced density.

3.4.5 Physical dimensions and density

The proper motion of κ Vel is 15.5 mas yr^{-1} (ESA 1997), so at a distance of 165 pc the transverse velocity is 2.56 AU yr^{-1} (12.1 km s^{-1}). This results in a stellar displacement of 10.1 AU between the 2002 and 2006 observations, and 29.7 AU between 1994 and 2006. The size of the binary orbit has been determined to be $a_1 \sin i = 0.48$ AU, where a_1 is the semi-major axis of the orbit of the primary, and i the orbital inclination (Pourbaix et al. 2004). Since neither the inclination nor position angle of the orbital ellipse have been determined (though a fairly large i is implied by the velocity amplitude), it is impossible to include the effect of this on the transverse displacement, however the error thus introduced is likely to be quite small.

The displacement of the line-of-sight at the distance of the star provides an upper limit on the displacement at the distance of the foreground absorbing cloud. Dunkin and Crawford (1999) have argued that the cloud is likely to be located close to the star, at least 150 pc from the Sun, based on comparison with CO maps and optical absorption along other nearby lines-of-sight (see also Crawford 1991).

If the electron density is dominated by electrons released through the photoionisation of atomic carbon (this is the same assumption adopted by Crawford 2002, see equation 1.6), the electron density allows an estimate of the total number density to be obtained. Assuming a carbon depletion of 60% implies a gas-phase carbon abundance of $1.4 \times 10^{-4} n_{\rm H}$ (Sofia et al. 1997), which leads to estimates of $n^A \gtrsim 7 \times 10^3\,{\rm cm}^{-3}$ and $n^B \gtrsim 2 \times 10^4\,{\rm cm}^{-3}$. These are orders of magnitude higher than typical values for diffuse or translucent clouds (Snow and McCall 2006).

Welty (2007) has recently combined optical and UV observations (including C I and C II) of the small-scale structure towards HD 219188. It was inferred that the changing column densities reflected enhanced recombination due to a raised electron density, whose source was the ionisation of hydrogen. If this effect is also present in the line-of-sight towards κ Vel, the densities derived above will be overestimates. Since hydrogen is thousands of times more abundant than carbon (exactly how more abundant depends on the depletion and/or incorporation of C into molecules), even a small fractional ionisation of hydrogen could reduce the density estimate by an order of magnitude or more. An ionisation fraction of $\gtrsim 1\%$ would be required to reduce the density to typical levels for the diffuse ISM, which would be difficult to reconcile with the constraints on temperature from the linewidths (photoelectrons inject energy into the ISM, raising the local temperature), and require a physical cause such as instense cosmic ray bombardment.

3.4.6 Comparison with chemical model

The chemical model of Bell et al. (2005) includes predictions for column densities of CH, C_2, Ca I and Ca II (plus OH and CO) along a line of sight based on the physical parameters derived for κ Vel by Crawford (2002), as a function of cloud density and time. Because no partitioning of molecules between components A and B has been detected, for comparison with the model the observed column densities of these species are summed over both cloud components. This results in $N^{AB}({\rm CH}) = 2.95 \times 10^{11}$, $N^{AB}({\rm C_2}) \lesssim 6 \times 10^{11}$ (2σ), $N^{AB}({\rm Ca\,I}) = 4.15 \times 10^9$ and $N^{AB}({\rm Ca\,II}) = 2.07 \times 10^{11}\,{\rm cm}^{-2}$.

The column densities of Ca I and Ca II are reproduced in the models with the highest density, $n = 10^5\,{\rm cm}^{-3}$. However, these models predict column densities of both CH and C_2 of $\sim 10^{12}\,{\rm cm}^{-3}$, contrary to the observations. However, Bell et al. note that their chemical abundances are proportional to $n({\rm H_2})/n({\rm H})$, which they set equal to 0.4. Were the fraction of hydrogen in molecular form to be lower than this, the detected column densities of both atoms and molecules could be consistent with the Bell et al. model.

The model and observations would be consistent (with C_2 just below the detection limit) at a molecular fraction of $n(H_2)/n(H) = 0.1$, at $n = 10^5$ cm^{-3} and age ~ 10 yr.

The column densities of Bell et al. (2005) were calculated assuming a path length through the cloud of 100 AU, as inferred by Crawford (2002). However, Crawford calculated this path length from a simple chemical model and the then-observed CH column density, so assuming a 100 AU path length in chemical models with CH column densities which vary over of many orders of magnitude becomes a case of circular logic. The path length is thus a further free parameter which may serve to modify the predicted column densities. Compared to the values assumed by Bell et al., reducing the molecular fraction but raising the path length to compensate serves to increase the predicted column density of the atomic species whilst holding the molecular species constant. Models with density as low as 10^4 cm^{-3} (lower densities are precluded by the electron density measurements) reproduce the Ca I, Ca II and CH column densities if the path length is a factor of ten higher ($\sim$ 1,000 AU) and the molecular fraction a factor of ten lower ($\sim$0.03) than assumed by Bell et al. Such a model would predict C_2 column density over an order of magnitude below the current detection limit.

If the molecular hydrogen fraction is as low as 10^{-3} as implied by the Ca I/K I ratio, then the path length through the cloud would need to be raised by several orders of magnitude to compensate. But this would also raise the column densities of the atomic species, in gross violation of the observations. An alternative explanation might be that the local density and/or H_2 fraction are highly variable *within* each component along the line of sight. If this were true, it would be possible for CH to be formed in regions of relatively high H_2 density, but the atomic lines to trace less-dense material elsewhere. In the absence of further H_2 tracers, this contradiction in derived molecular hydrogen fractions cannot be resolved.

The chemical models do not determine the effect temperature would have on the column densities (nor do Bell et al. state the temperature they assume). This would appear to be parameter space worth exploring. The time-dependence allowed in the models is difficult to interpret, because the structure will not have formed instantaneously. However, in the absence of a known formation mechanism, it is difficult to see how this could be improved. The meaningfulness of an 'age' of ~ 10 yr is therefore questionable.

3.5 Conclusions

New ultra-high resolution observations of interstellar absorption towards κ Vel have been obtained, of the species K I, Na I, Ca I, Ca II and CH. A search for C_2 was performed, but no lines were detected. Best-fitting model line profiles were computed and two main absorption components identified. Comparison to observations taken at earlier epochs shows continued increases in interstellar absorption over a period of several years. During this time, the transverse velocity of the star has shifted the line-of-sight through the interstellar cloud by 10 AU (since the last observations in 2002).

From a consideration of the Doppler b parameter in each component, a rigorous upper limit can be placed on the kinetic temperature of each component. Combining limits from each species, the temperatures of components A and B must be $T_k^A < 660 \pm 20$ and $T_k^B < 120 \pm 20$ K. However, the temperatures may be lower if the turbulent velocity makes a significant contribution to the b values. The Ca I/K I ratio was used to derive logarithmic depletions of $D(\mathrm{Ca})^A = -1.77$ and $D(\mathrm{Ca})^B = -1.02$, which indicate that calcium is more strongly depleted in component A than component B. This in turn implies $T_k^A < T_k^B$, and thus $v_t^A \gtrsim 0.3\,\mathrm{km\,s^{-1}}$. In the absence of a C_2 detection and the direct measurement of temperature this would have provided, this scenario remains speculative.

The Ca I/Ca II ratio was used to derive estimates of the electron density in the two components. By assuming that electrons originate from photoionisation of neutral atomic carbon and assuming a value for the carbon depletion, lower limits on the density of $n^A \gtrsim 7 \times 10^3\,\mathrm{cm^{-3}}$ and $n^B \gtrsim 2 \times 10^4\,\mathrm{cm^{-3}}$were derived, far higher than typical densities in the diffuse ISM. Comparison of the observed CH abundance and C_2 upper limit with the chemical model of Bell et al. (2005) confirms the requirement for a high space density. However it is difficult to find a set of model parameters consistent with the data, particularly the low C_2 abundance, without adjusting the assumptions of Bell et al. By lowering the H_2 fraction, the observations may be reproduced, but requires a path length of $\sim$1,000 AU, ten times that inferred by Crawford (2002). Testing these hypotheses will require more observations, ideas for which are discussed in chapter 6.

Chapter 4

Diffuse interstellar bands as probes of spatial small-scale structure

The use of diffuse interstellar bands as probes of small-scale structure is a recent innovation, but one which shows great promise. The large FWHMs of DIBs compared to other interstellar lines means they can be observed at much lower resolutions (typically $R = 5,000$–$10{,}000$, rather than $R \gtrsim 100,000$) without problems of unresolved saturation. Combined with the large equivalent widths of the stronger DIBs, the reduction in the required observing time can be dramatic. In principle, it should be possible to quickly survey a large number of targets, reaching fainter magnitudes than are possible with high resolution spectrographs.

Whilst DIBs provide an opportunity to quickly identify SSS sightlines, they do not in themselves assist in the determination of the physical conditions within the structure or the processes which lead to their formation. Follow-up observations of atomic lines towards promising systems are still required. However, such studies could lead to new insights into the DIB carriers, because to a first approximation the interstellar conditions along the two (or more) lines of sight are identical. Therefore, any variations in the DIB spectrum (e.g. ratios between DIBs) can be related to the differences in conditions between lines-of-sights determined via atomic lines.

Prior to the work described in this chapter, the only DIB SSS study published in the literature was that of Cordiner et al. (2006), who used $R \sim 60,000$ spectroscopy of the ρ Oph system to demonstrate that DIB carriers share the small-scale structure seen in atomic lines. In this chapter, two studies are presented which both use intermediate-resolution observations of DIBs to measure small-scale structure, over scales from 50,000 AU to several parsecs. In section 4.1, SALT/RSS long-slit observa-

tions of DIBs towards several binary/multiple star systems are presented. In section 4.2, AAT/AAOmega observations are presented of DIBs and atomic lines towards several hundred stars in the globular cluster ω Cen.

4.1 Long-slit spectroscopy of diffuse interstellar bands towards multiple-star systems

4.1.1 Observations and data reduction

Three multiple star systems were observed using the Robert Stobie Spectrograph (RSS, Burgh et al. 2003; Kobulnicky et al. 2003) mounted at the prime focus of the 9.2 m Southern African Large Telescope (SALT). Observations were undertaken in September 2006, during the telescope and instrument commissioning period. The observers were M Cordiner (Nottingham) and Y Hashimoto (SALT); the author performed the data reduction and analysis*. The selected systems are bright, early-type visual multiple stars with component separation in the range 5-60″. The systems observed were the binary pairs HD 168075/6 and HD 176269/70, and three components of the μ Sgr system (A, D, & E); the systems are shown in figures 4.1–4.3. A fourth star also (serendipitously) fell on the slit during the μ Sgr observations; as discussed in section 4.1.3.3 it is believed that this is also a member of the system. Stellar data are presented in table 4.1.

RSS was operated in long slit mode, with the slit position angle selected to cover each of the components of the systems simultaneously. The G2300 grating was used at an angle of 47° and the camera angle was set to 91.75°, slightly displaced from the optimum Littrow configuration. This setup was selected as it provides wavelength coverage from 5760-6650 Å, allowing simultaneous observation of the λ5780 and λ6613 DIBs. Two small gaps in wavelength coverage are present around 6085 and 6385 Å due to the gaps between the three CCD detectors. Flat fields were provided by an internal quartz lamp, whilst wavelength calibration was by means of a CuAr arc lamp. The observations were performed as a poor-weather backup program; as such, conditions were poor, consisting of thin-to-moderate cloud, full moon and poor seeing ($\gtrsim$ 1.5″).

For the binary pairs the slit width was set to 0.6″, providing the highest resolving power available. This was widened to 1.0″ for the μ Sgr observations, which cov-

*The author also has observing experience on this telescope, obtained during a two month placement working at the observatory

Name	RA (J2000)	Dec (J2000)	V mag	Sp. type	Exp. time (s)	S/N @ 6000 Å	Notes
HD 168075	18:18:36.06[a]	−13:47:36.3[a]	8.73[a]	O6.5 V((f))+B0-1 V[b]	570	700	in Eagle Nebula
HD 168076	18:18:36.44[a]	−13:48:03.1[a]	8.18[a]	O4 V((f))[b]		1,000	r = 27.4″, ρ = 168°
HD 176269	19:01:03.26[c]	−37:03:39.3[c]	6.58[d]	*	1480	1,200	in R CrA cloud
HD 176270	19:01:04.30[c]	−37:03:41.6[c]	6.33[d]	*		1,400	r = 13.0″[d], ρ = 94
μ Sgr A	18:13:46.0[f]	−21:03:30[f]	3.85[d]	B8 1ae[e]	2430	400	
μ Sgr D	18:13:43.2[f]	−21:02:58[f]	9.96[d]	B3 V[e]		800	r = 48.2″[d], ρ = 312
μ Sgr E	18:13:49.2[f]	−21:03:52[f]	9.22[d]	B2 V[e]		1,200	r = 50.6″[d], ρ = 115
μ Sgr F	18:13:35.6[f]	−21:01:50[f]	10.2[f]	†		450	r = 177″, ρ = 125

* see discussion in section 4.1.3, † see discussion in section 4.1.3.3, [a]Evans et al. 2005, [b]Sana et al. 2009, [c]Ducourant et al. 2005, [d]Mason et al. 2001, [e]Lindroos 1985, [f]Dommanget and Nys 2000

Table 4.1 – Stellar data and summary of observations. Angular separations r and position angles ρ are also given.

Figure 4.1 – Location of HD 168075 and HD 168076 in the Eagle Nebula. Background image is a *BVR* colour composite, copyright European Southern Observatory, used under license.

ered μ Sgr D, E & F simultaneously; this slit position is shown in figure 4.3. Although μ Sgr A did not fall directly on the slit, its much higher brightness coupled with the seeing at the time allowed sufficient light to be collected for a good quality spectrum. Due to the VPH gratings utilised in RSS, the resolving power varies with the wavelength, in the sense of higher resolution at longer wavelength. Measurement of the FWHM of the CuAr comparison lines indicated a resolution of $R = 6,200$–$8,900$ for the $0.6''$ slit and $R = 4,400$–$6,400$ for the $1.0''$ slit over the full wavelength region.

The data were processed by the automated RSS pipeline then in operation, which performed overscan, amplifier crosstalk, bias and gain corrections, and mosaicked the output from the three CCDs. Further reduction was performed using standard IRAF tasks, primarily those in the `twodspec.longslit` package. This consisted of cosmic ray removal, flat-fielding, wavelength assignment, distortion correction, scattered light subtraction, variance weighted extraction, radial velocity correction to the heliocentric reference frame and co-addition of the separate exposures. At the time of the observations RSS was not yet equipped with its full suite of light baffles, resulting in an

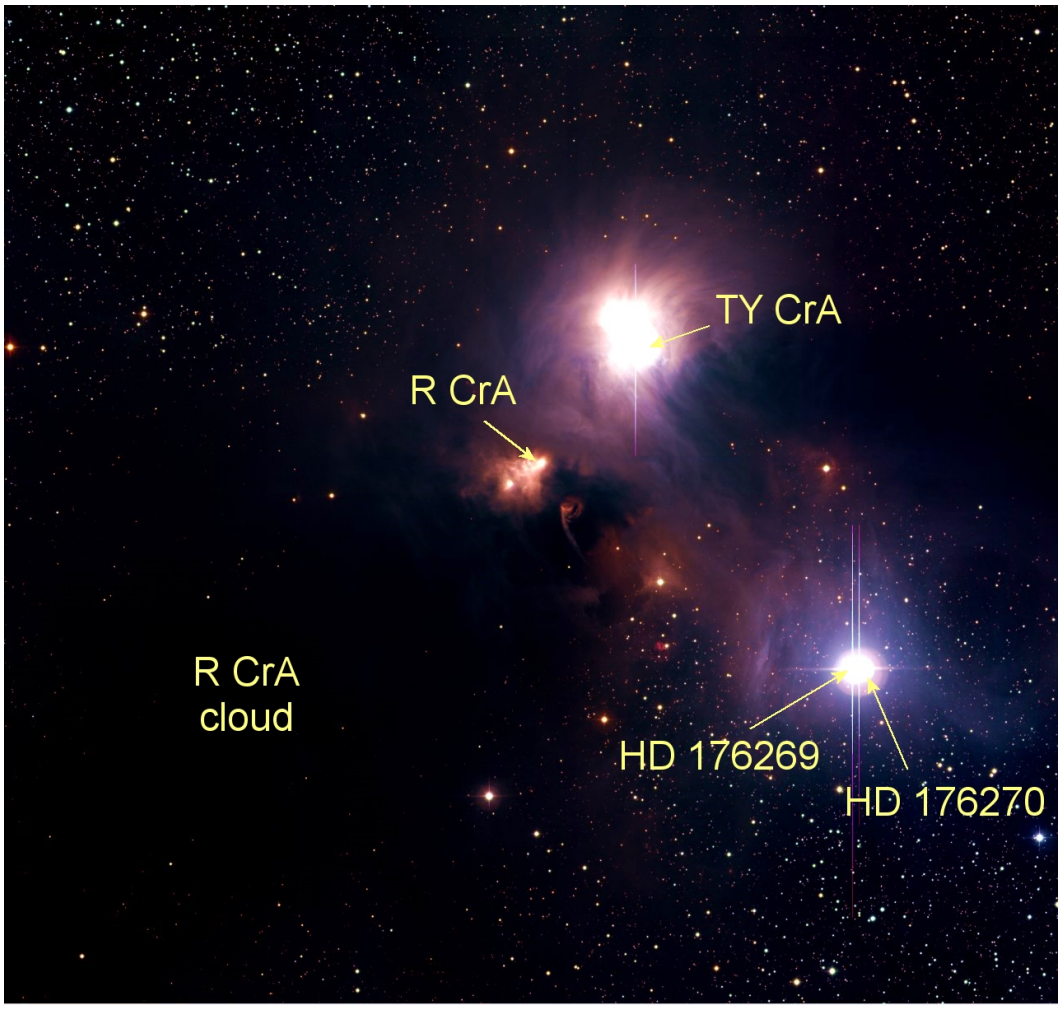

Figure 4.2 – Location of HD 176269 and HD 176270 in the R CrA star forming complex. Background image is a *BVR* colour composite, copyright European Southern Observatory, used under license. HD 176269 and HD 176270 are separated by 52,000 AU.

unusually high level of scattered light which required particular care to remove during the reductions. The final signal-to-noise ratio obtained for each star varied in the range 400–1,400 and is given in table 4.1.

4.1.2 Analysis

The the Na I D lines and the $\lambda\lambda$5780, 5797, 5850, 6196, 6203, 6269, 6283 and 6613 DIBs were selected for analysis as these were the strongest interstellar absorption features in the observed wavelength region*. The λ6376 and λ6379 DIBs were lost in one of the gaps between the CCDs. In order to measure small changes in absorption features

*A total of thirty-one DIBs with EW $\gtrsim$ 40 mÅ were detected in the spectra of HD 168075/6

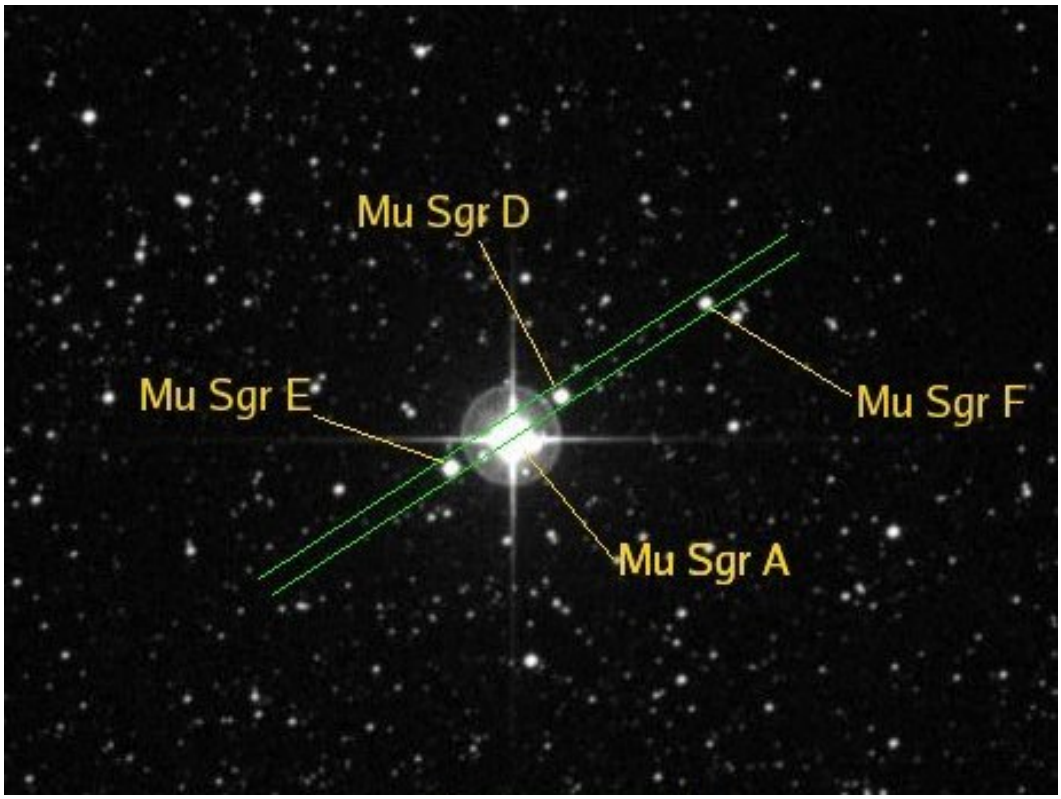

Figure 4.3 – Slit position for the μ Sgr observations, overlaid on a Digitized Sky Survey *R* band image. Components A & D are separated by 58,000 AU.

it is important to eliminate systematic effects which could artificially change the measured strengths of the features. For this reason, two different analysis techniques were employed.

The first method of analysis consisted of a conventional cancellation of telluric lines, continuum normalisation, and measurement of equivalent widths. The telluric spectrum was provided by observations of the unreddened star τ Sco immediately prior to the science targets; this spectrum has a signal-to-noise ratio of 1,800. The IRAF task `noao.onedspec.telluric` was used for this purpose; in order to minimise systematics the `shift` and `scale` task parameters were optimised for the star with the highest signal-to-noise in each system and then held constant for the other(s). Telluric cancellations were performed for the $\lambda\lambda$5780, 5797, 6269 and 6283 DIBs and the Na I D lines; the $\lambda\lambda$5850, 6196, 6203 and 6613 DIBs were found to be free of telluric contamination. The continuum fitting utilised a consistent set of wavelength regions for each interstellar feature and a low order Legendre polynomial fitting function. As examples, the operation of this procedure for the $\lambda\lambda$5780, 5797, 6269 and 6283 DIBs is shown for HD 168075 (only) in figures 4.4 and 4.5.

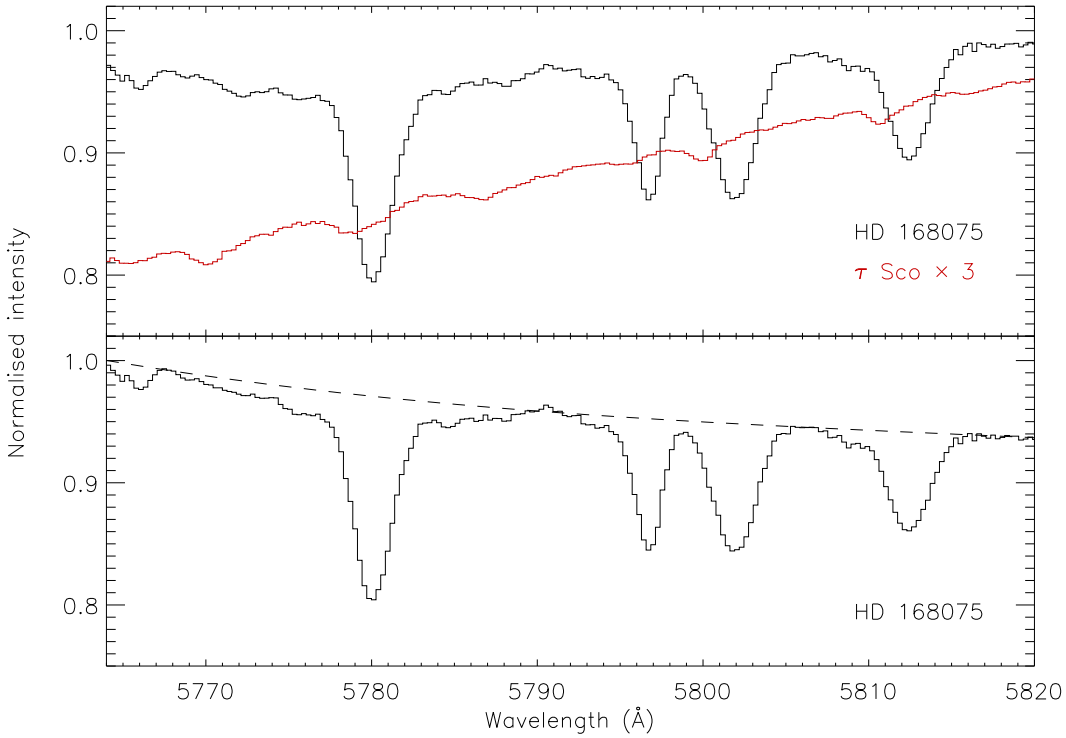

Figure 4.4 – Telluric cancellation and continuum normalisation of the region around the $\lambda\lambda$5780 and 5797 DIBs towards HD 168075. Upper panel: uncorrected spectrum and telluric standard spectrum. The telluric spectrum has been scaled by a factor of three for display. Lower panel: corrected spectrum and adopted continuum.

The second method of analysis uses the technique described by Cordiner et al. (2006). In this method, conventional telluric line cancellation and continuum normalisation are not performed. Instead, the two (or more) spectra are divided by each other, followed by a single low-order normalisation of the ratio spectrum to remove any residual slope. This method removes the possible systematic effects due to differences in the telluric cancellation and continuum normalisation of the two spectra. Telluric lines are still removed from the spectrum, because they are identical for each star observed on the same slit. Indeed, this method may actually perform better than the conventional telluric cancellation, because it eliminates the possibility of any variation in the telluric spectrum over time or position in the sky (compare the cancellation at the peak of the telluric O_2 a-band in figure 4.14 and figure 4.15). The ratio method does not directly allow the measurement of equivalent widths; instead it illustrates the percentage change between the two spectra. This provides an arguably more useful – and certainly more reliable – measure of any variations, providing confidence that the observed variations

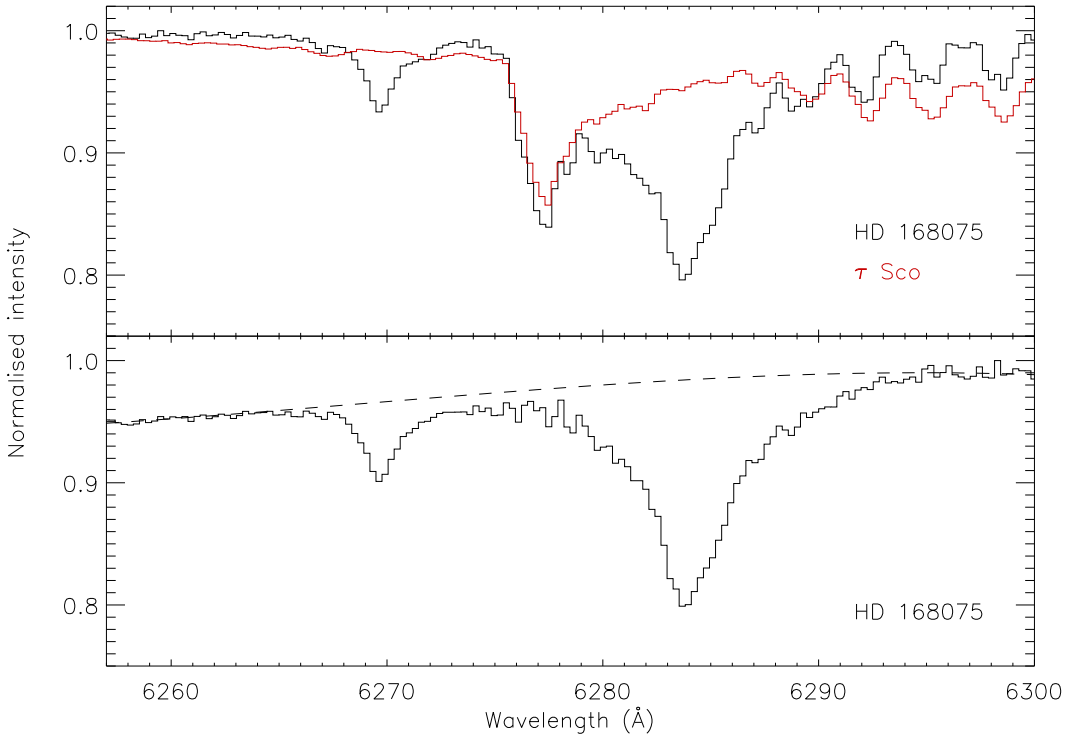

Figure 4.5 – Telluric cancellation and continuum normalisation of the region around the $\lambda\lambda$6269 and 6283 DIBs towards HD 168075. Upper panel: uncorrected spectrum and telluric standard spectrum. Lower panel: corrected spectrum and adopted continuum.

are not caused by systematic effects.

4.1.3 Results

Both the HD 168075/6 and μ Sgr systems show clear variations in interstellar absorption. Comparisons of the DIB and Na I D absorption towards each star and the corresponding ratio spectra are shown in figures 4.6–4.29 (in the figures, the DIB rest wavelengths have been taken from Hobbs et al. 2008). The measured equivalent widths are given in table 4.2; because the λ6269 and λ6283 DIBs overlap, the combined EWs for the pair of DIBs are also given.

4.1.3.1 HD 176269/70

During data reduction, it was found that interstellar absorption towards HD 176269/70 was far weaker than expected: no DIBs with a central depth greater than 1% were detected. However, strong H α emission from both stars was seen. The $E_{(B-V)}$ calculated

during target selection was based upon the spectral types quoted in the CCDM and Hipparcos catalogues (Dommanget and Nys 2000; ESA 1997), which are B7/B8 V and B9.5 IV for HD 176269 and HD 176270 respectively. In turn, these catalogues apparently took these spectral types from Houk (1982). More recent sources refer to these stars as Herbig Ae/Be stars, which is a designation that seems to have first appeared in Teixeira et al. (2000). Herbig Ae/Be stars are a type of young stellar object, and are the more massive counterparts of T Tauri stars. They consist of a star of spectral type A or B which is still enshrouded in material from the process of star formation, which results in an infrared excess and emission lines (chiefly Balmer and Ca II). Much of the measured reddening is therefore due to circumstellar rather than interstellar material; circumstellar material is well known to be deficient in DIBs (e.g. Krełowski and Sneden 1995; Kendall et al. 2002; Galazutdinov and Krełowski 2006; Luna et al. 2008). Unfortunately, this resulted in no interstellar absorption strong enough for statistically significant variations between the two stars to be determined.

4.1.3.2 HD 168075/6

The λ5797 DIB overlaps slightly with the stellar C IV 5801 Å line in HD 168075/6 (the C IV 5812 Å line is also visible; these lines are only present in O stars). Due to the difference in spectral type between the two stars, this line is stronger in HD 168075

DIB	HD 168075	HD 168076	μ Sgr A	μ Sgr D	μ Sgr E	μ Sgr F
5780	434 ± 1	467 ± 2	271 ± 4	241 ± 3	238 ± 1	265 ± 4
5797	260 ± 2	267.7 ± 1.5	124 ± 6	94 ± 3	99 ± 2	105 ± 4
5850	92 ± 3	81 ± 2	44 ± 3	49 ± 2	44 ± 2	55 ± 3
6196	63.2 ± 0.5	64.1 ± 0.5	24 ± 2	21 ± 1	29 ± 1	30 ± 3
6203	250 ± 1	254 ± 2	80 ± 4	114 ± 2	105 ± 2	123 ± 5
6269	210 ± 10	236 ± 7	105 ± 6	146 ± 8	82 ± 6	136 ± 9
6283	1, 148 ± 7	1, 127 ± 7	758 ± 10	786 ± 12	731 ± 6	691 ± 10
6269+83	1, 345 ± 12	1, 354 ± 7	873 ± 7	936 ± 4	802 ± 3	825 ± 6
6613	223 ± 4	231 ± 2	86 ± 3	95 ± 1	88 ± 3	106 ± 3

Table 4.2 – Measured equivalent widths (in mÅ) of the diffuse interstellar bands towards the HD 168075/6 and μ Sgr systems. The $\lambda\lambda$6269 and 6283 DIBs are blended, so both the individual equivalent widths and the (considerably less uncertain) total for the blend are given.

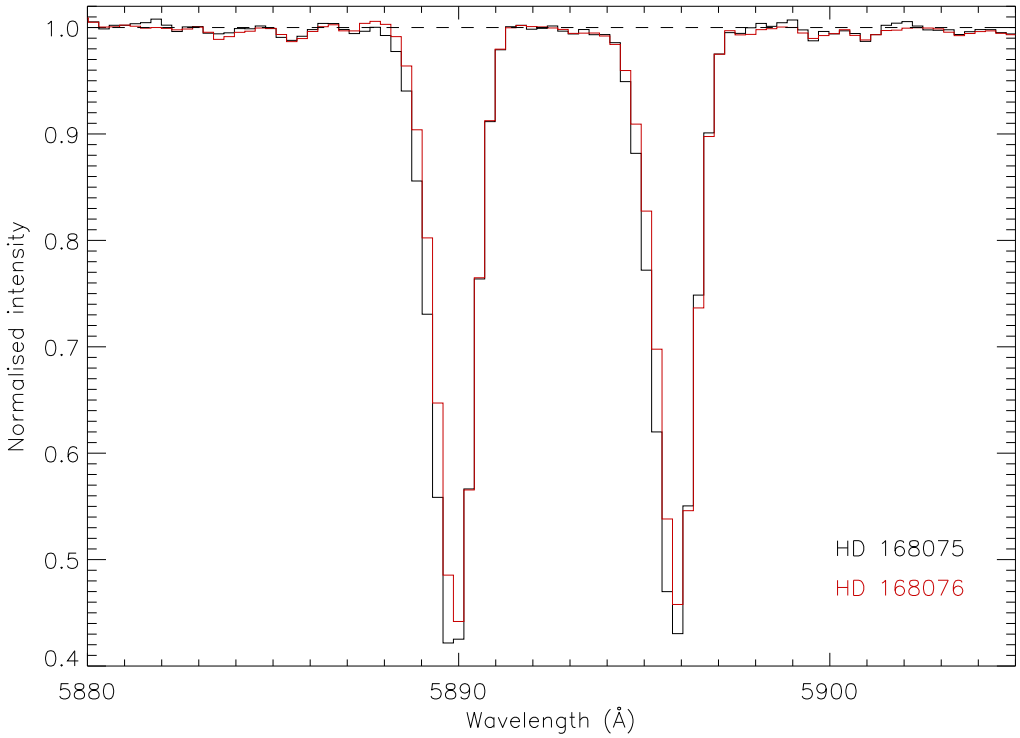

Figure 4.6 – Comparison of the sodium D lines towards HD 168075 and HD 168076. The horizontal dashed line indicates the continuum level, whilst the vertical dotted lines indicate the D_1 and D_2 rest wavelengths. The absorption is stronger towards HD 168075, and shifted to the blue.

than in HD 168076. This difference would pollute λ5797 in the ratio spectrum, so the C IV line was fit with a Gaussian profile and subtracted before the ratio was calculated. This procedure is shown in figure 4.9.

The binary pair HD 168075/6 is located in NGC 6611 at the centre of the Eagle Nebula (see figure 4.1), and are the earliest-type stars in the OB association which ionises the surrounding nebula (Evans et al. 2005). The stellar parameters have been modelled by Dufton et al. (2006), who determined $M = 50\,M_\odot$, $v_r = 17\,\mathrm{km\,s^{-1}}$, $v \sin i = 87\,\mathrm{km\,s^{-1}}$and $E_{(B-V)}$= 0.73 for HD 168075 and $M = 63\,M_\odot$, $v_r = 14\,\mathrm{km\,s^{-1}}$, $v \sin i = 102\,\mathrm{km\,s^{-1}}$and $E_{(B-V)}$= 0.71 for HD 168076 (where v_r is the stellar radial velocity, and $v \sin i$ is the projected stellar rotation speed), under the assumption that each is a single star. However, more recent evidence suggests that HD 168075 is a binary system consisting of an O6.5 V((f)) primary and a B0-1 V secondary in a 44 day orbit (Sana et al. 2009). HD 168076 is probably also a binary, of spectral types O3.5 V((f+)) and O7.5 V, separated by 0.15″ and with a "minimal orbital period of several hundreds

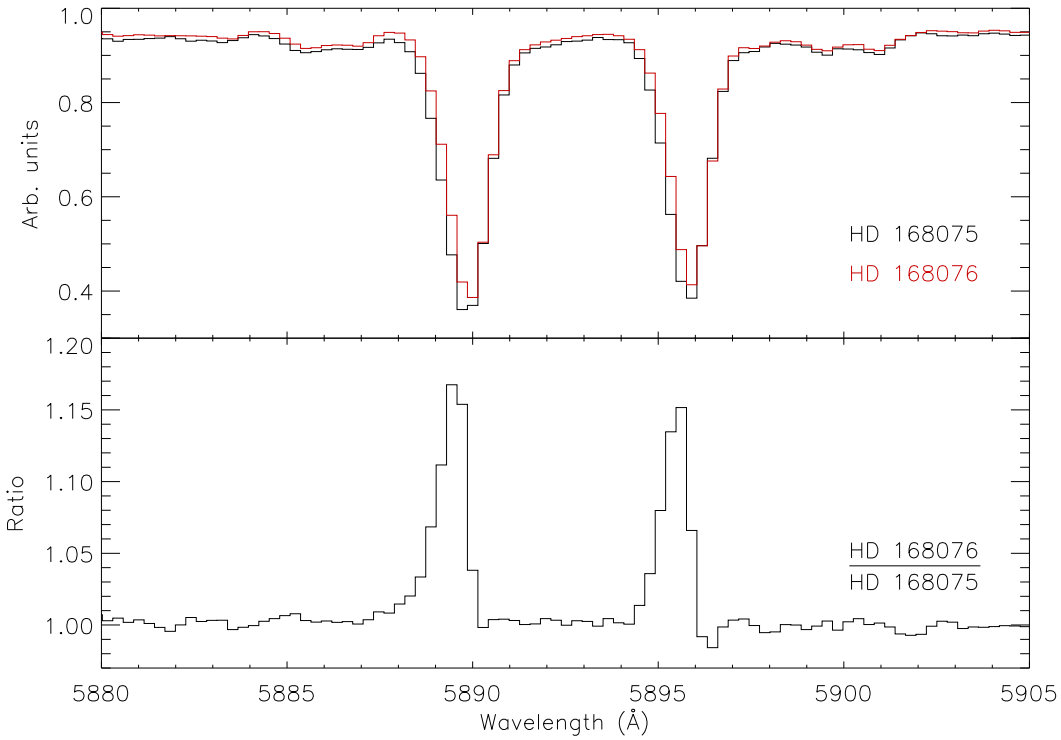

Figure 4.7 – Ratio of the region around the sodium D lines towards HD 168075 and HD 168076. Upper panel: extracted spectra. Lower panel: ratio spectrum. The vertical dotted lines indicate the D_1 and D_2 rest wavelengths. The absorption is stronger towards HD 168075, and shifted to the blue.

of years" (Sana et al. 2009). On the basis of these binary identifications and the measured $R_V = 3.75 \pm 0.2$ (Hillenbrand et al. 1993), the new reddenings were determined to be $E_{(B-V)} = 0.81 \pm 0.11$ (HD 168075) and $E_{(B-V)} = 0.71 \pm 0.10$ (HD 168076), and the distance $d = 1.9 \pm 0.1$ kpc (Sana et al. 2009). Given these uncertainties, it seems far from certain that there is any significant variation in the reddening of the two stars, though the possibility certainly exists.

The projected physical distance s between the lines of sight is given by:

$$s = d \sin r \tag{4.1}$$

where r is the angular separation. For small r, this may be expressed in convenient units as:

$$s(\mathrm{AU}) = d(\mathrm{pc}) \times r(\mathrm{arcsec}). \tag{4.2}$$

For HD 168075/6, $r = 27.4''$(calculated from the coordinates using the spherical cosine rule) and so $s = (52 \pm 5) \times 10^3$ AU. The actual separation between the two stars will

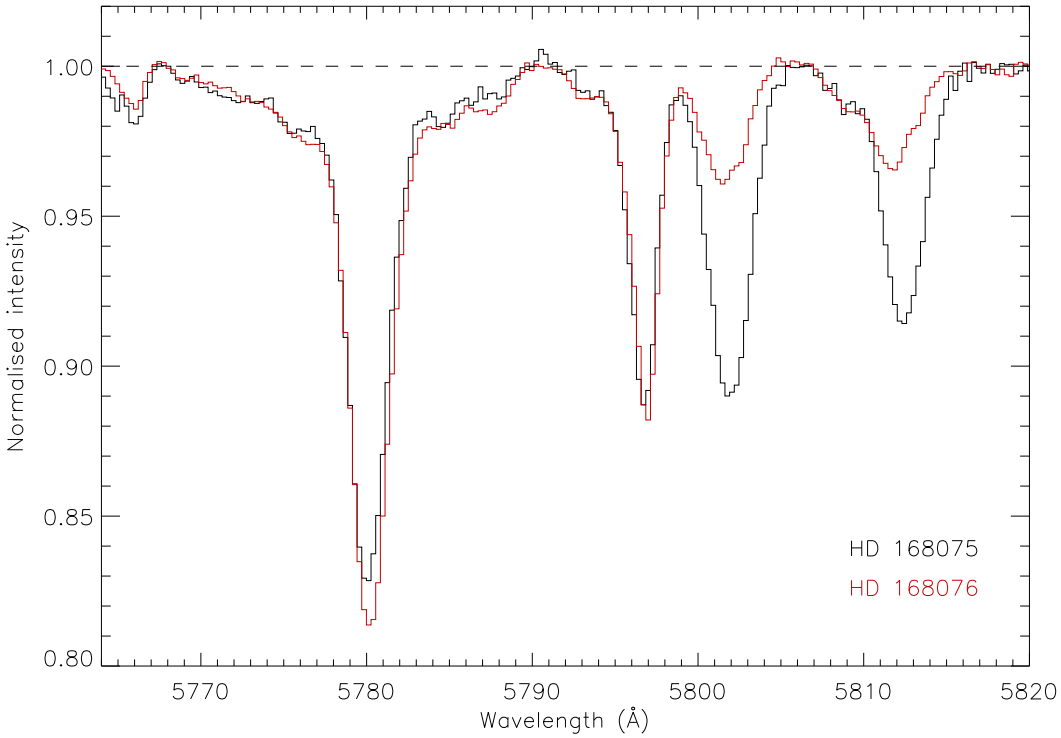

Figure 4.8 – Comparison of the $\lambda\lambda$5780 and 5797 DIBs towards HD 168075 and HD 168076. λ5780 is stronger towards HD 168076. The horizontal dashed line indicates the continuum level, whilst the vertical dotted lines indicate the DIB rest wavelengths.

be larger than this, due to displacement along the line of sight, but none of the cold neutral medium will exist close to the stars at the centre of the H II region. Because the interstellar absorption could occur at any point along the path between the stars and the Earth, s is in fact an upper limit on the distance between the absorbers. The galactic coordinates of NGC 6611 are $l = 16.9$, $b = +0.8$ which places the nebula in the Sagittarius-Carina spiral arm; Sgr-Car is the next spiral arm inwards from the Ori-Cyg arm within which the Sun is currently located. This implies that the majority of the absorbing material is likely to be located within the Sgr-Car arm and that the displacement between the absorbers is likely to be close to this upper limit.

The Na I D lines towards both stars in this system are significantly broader than the resolution element (63 km s^{-1} versus 44 km s^{-1}). As the actual linewidth of interstellar Na I should be $\lesssim 5$ km s^{-1}, this indicates the presence of multiple unresolved absorbing clouds along the line-of-sight. For optically thin absorption, the ratio between the equivalent widths of the D_1 to D_2 lines is 2, set by the differing oscillator strengths of the two transitions. Because it is expressed in equivalent width, this ratio should remain constant

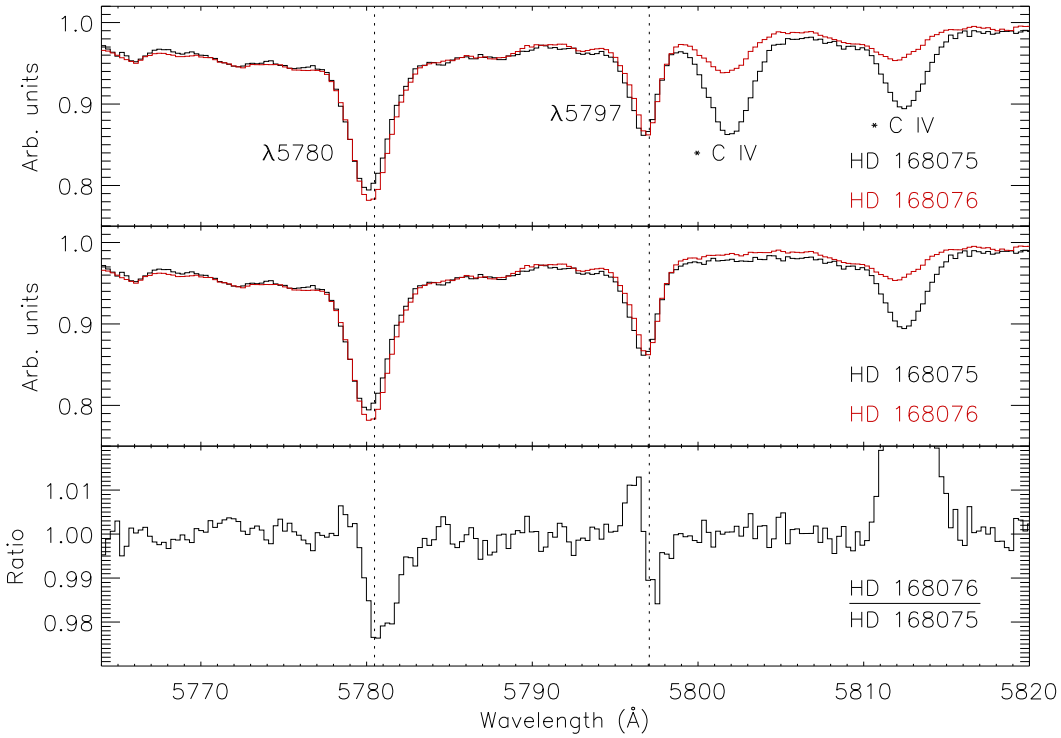

Figure 4.9 – Ratio of the region around the $\lambda\lambda$5780 and 5797 DIBs towards HD 168075 and HD 168076. Upper panel: extracted spectra. Middle panel: spectra after the subtraction of the C IV 5801 Å line. Lower panel: ratio spectrum. The vertical dotted lines indicate the DIB rest wavelengths. λ5780 is stronger towards HD 168076, whilst λ5797 exhibits a velocity shift between the two stars.

regardless of the resolution of the spectrograph and/or the number of absorbing clouds, providing each is optically thin. However, the D_1 to D_2 ratio is observed to be $\sim$ 1.2, which indicates at least one cloud has saturated absorption in these lines. This is not particularly surprising, since the D lines generally reach saturation at $E_{(B-V)} \sim 0.4$ (Munari and Zwitter 1997, cf. Na I absorption towards a star with $E_{(B-V)} = 0.10$ in figure 3.5). Due to these issues, no detailed modelling of the Na I absorption was attempted.

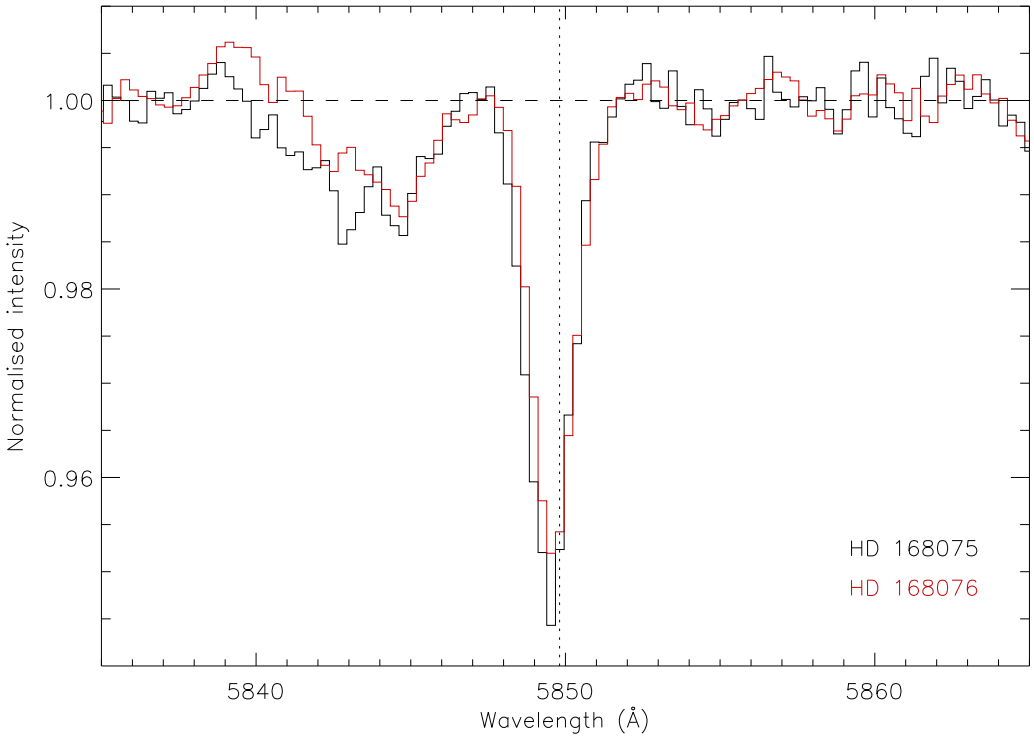

Figure 4.10 – Comparison of the λ5850 DIB towards HD 168075 and HD 168076. The horizontal dashed line indicates the continuum level, whilst the vertical dotted line indicates the DIB rest wavelength. λ5850 is stronger towards HD 168075; there is some evidence for a small velocity shift. The λ5844 DIB is also visible.

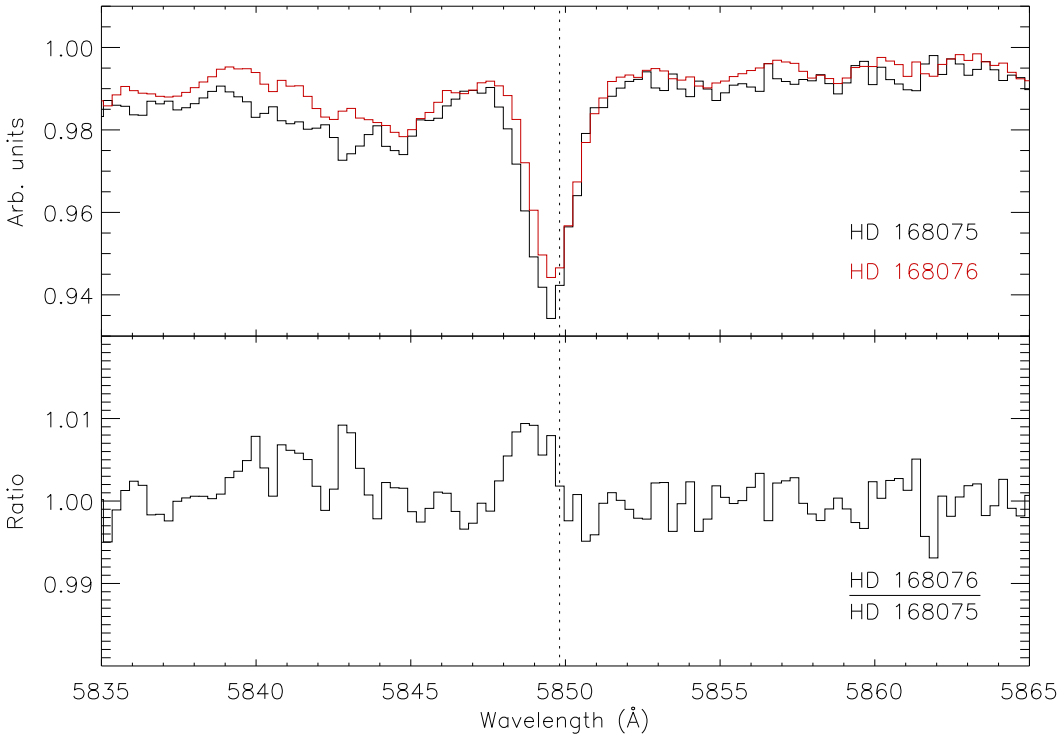

Figure 4.11 – Ratio of the region around the λ5850 DIB towards HD 168075 and HD 168076. Upper panel: extracted spectra. Lower panel: ratio spectrum. The vertical dotted line indicates the DIB rest wavelength. λ5850 is stronger towards HD 168075; there is some evidence for a velocity shift.

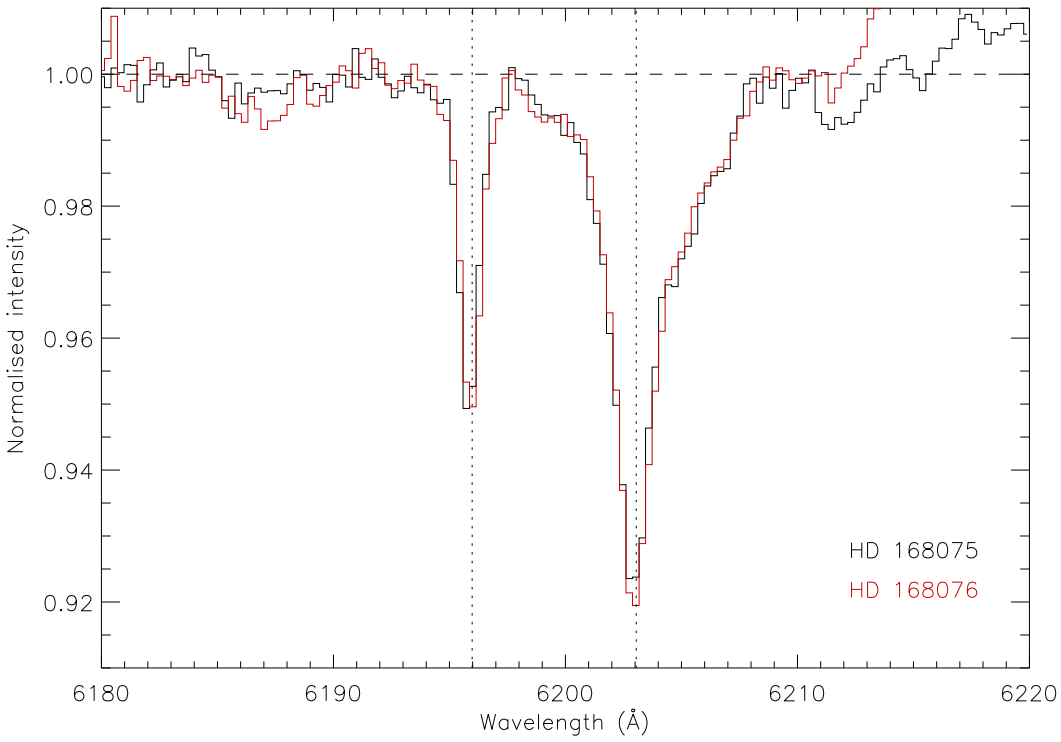

Figure 4.12 – Comparison of the $\lambda\lambda$6196 and 6203 DIBs towards HD 168075 and HD 168076. The horizontal dashed line indicates the continuum level, whilst the vertical dotted lines indicate the DIB rest wavelengths. There is some evidence that λ6203 is stronger towards HD 168076; there is no evidence for any variation in λ6196.

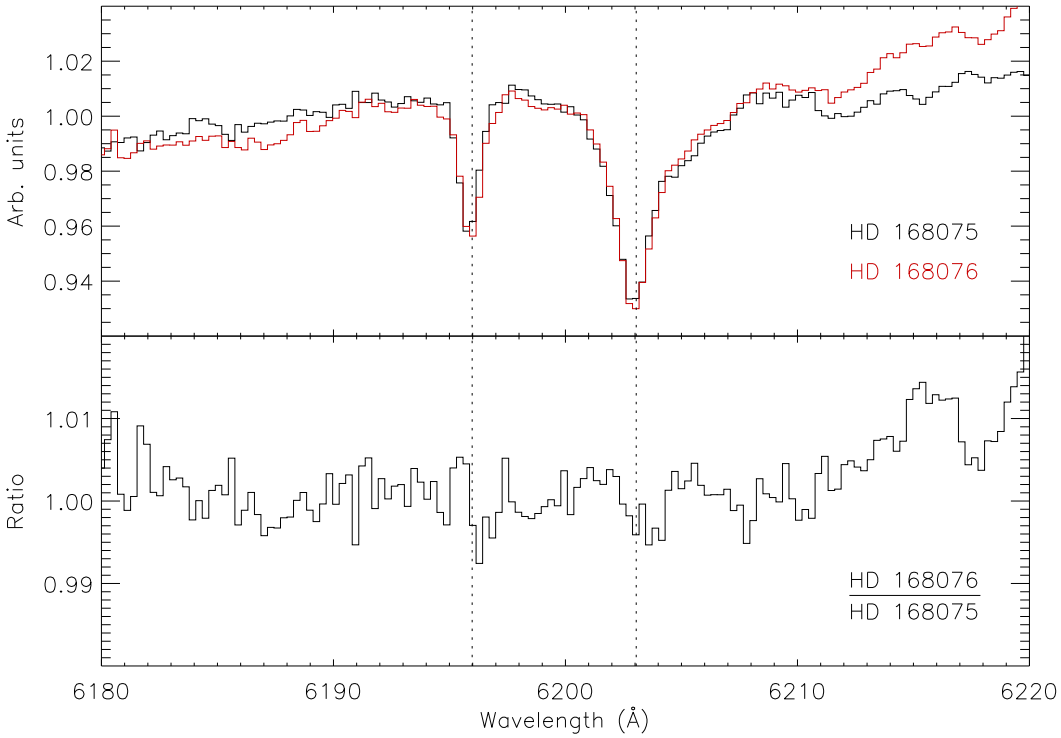

Figure 4.13 – Ratio of the region around the $\lambda\lambda$6196 and 6203 DIBs towards HD 168075 and HD 168076. Upper panel: extracted spectra. Lower panel: ratio spectrum. The vertical dotted lines indicate the DIB rest wavelengths. There is some evidence that λ6203 is stronger towards HD 168076; there is no evidence for any variation in λ6196.

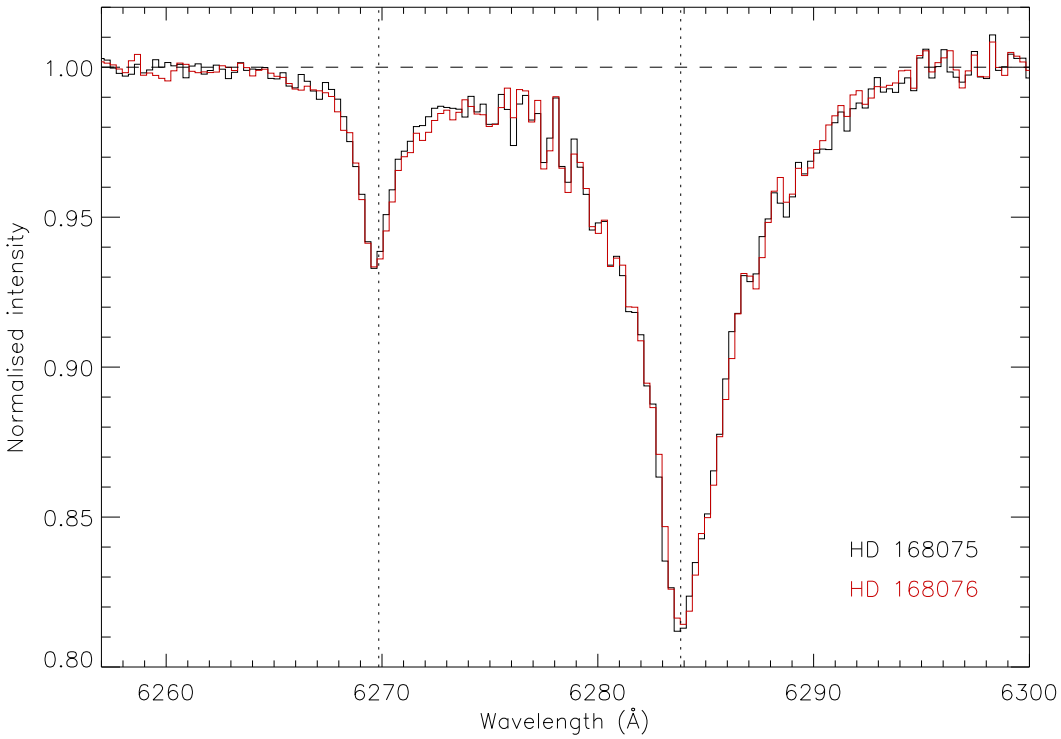

Figure 4.14 – Comparison of the $\lambda\lambda$6269 and 6283 DIBs towards HD 168075 and HD 168076. The horizontal dashed line indicates the continuum level, whilst the vertical dotted lines indicate the DIB rest wavelengths. There is no evidence for any variation.

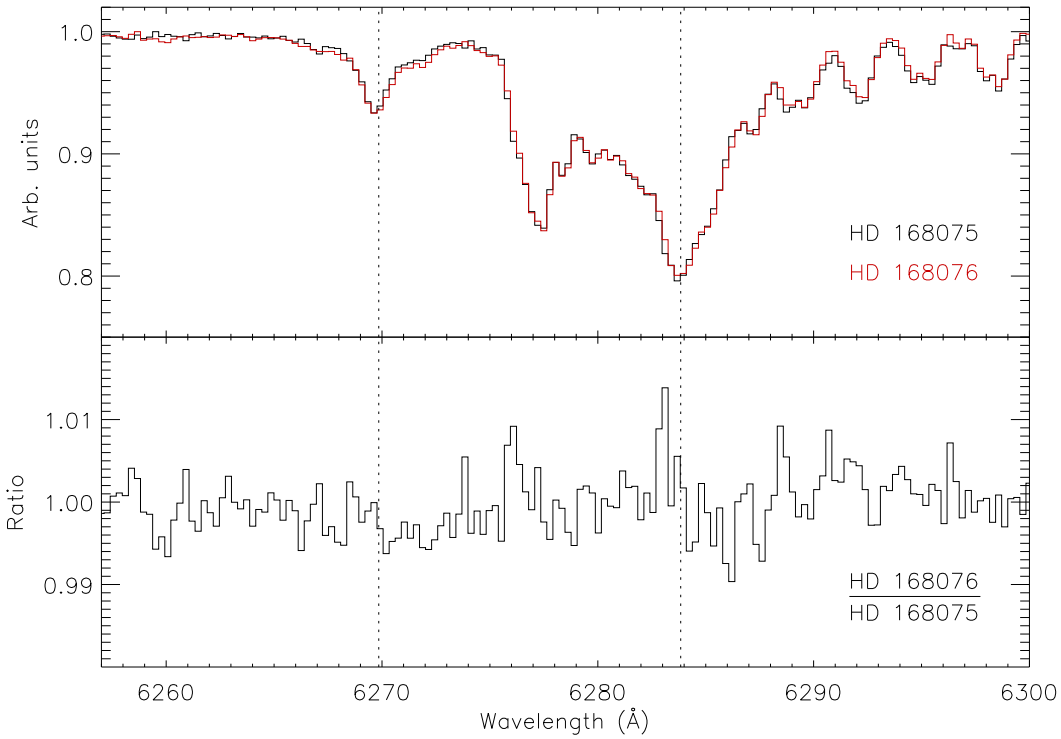

Figure 4.15 – Ratio of the region around the $\lambda\lambda$6269 and 6283 DIBs towards HD 168075 and HD 168076. Upper panel: extracted spectra. Lower panel: ratio spectrum. The vertical dotted lines indicate the DIB rest wavelengths. There is no evidence for any variation.

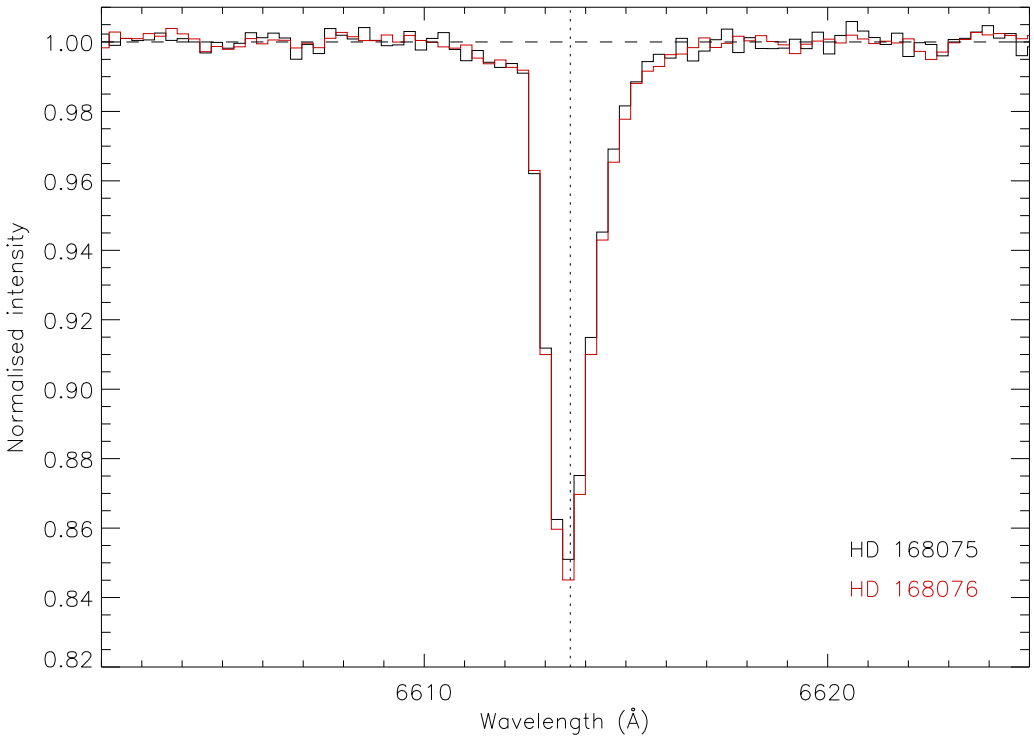

Figure 4.16 – Comparison of the λ6613 DIB towards HD 168075 and HD 168076. The horizontal dashed line indicates the continuum level, whilst the vertical dotted lines indicate the DIB rest wavelengths. There is some evidence that λ6613 is stronger towards HD 168076.

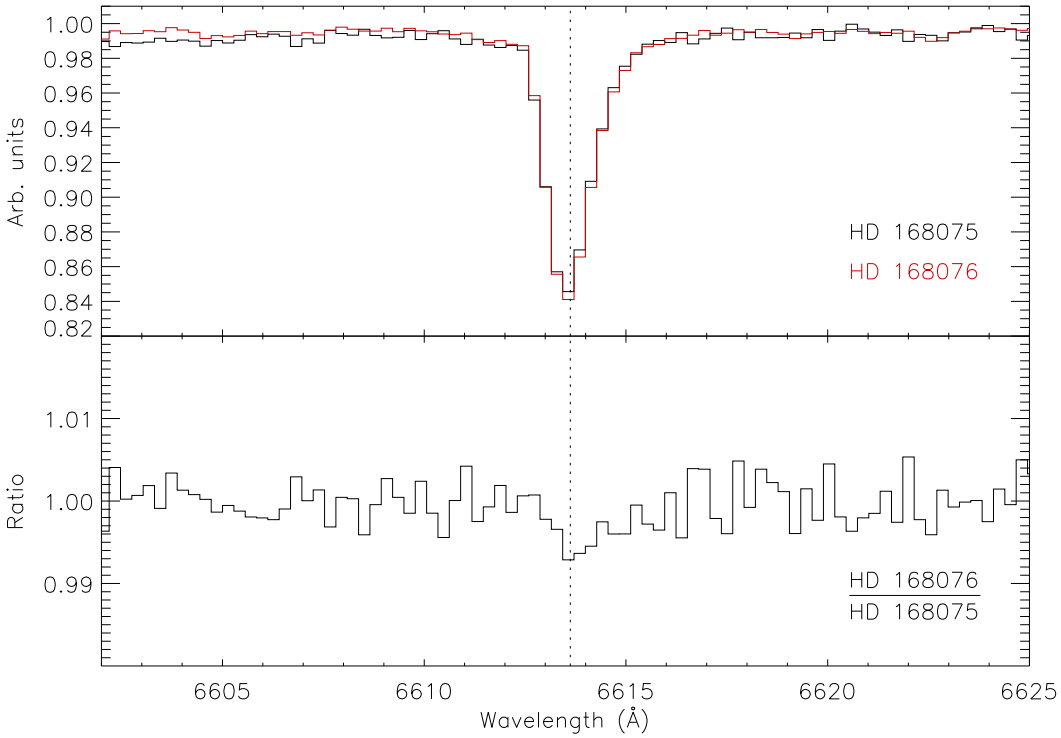

Figure 4.17 – Ratio of the region around the λ6613 DIB towards HD 168075 and HD 168076. Upper panel: extracted spectra. Lower panel: ratio spectrum. The vertical dotted line indicates the DIB rest wavelength. There is some evidence that λ6613 is stronger towards HD 168076.

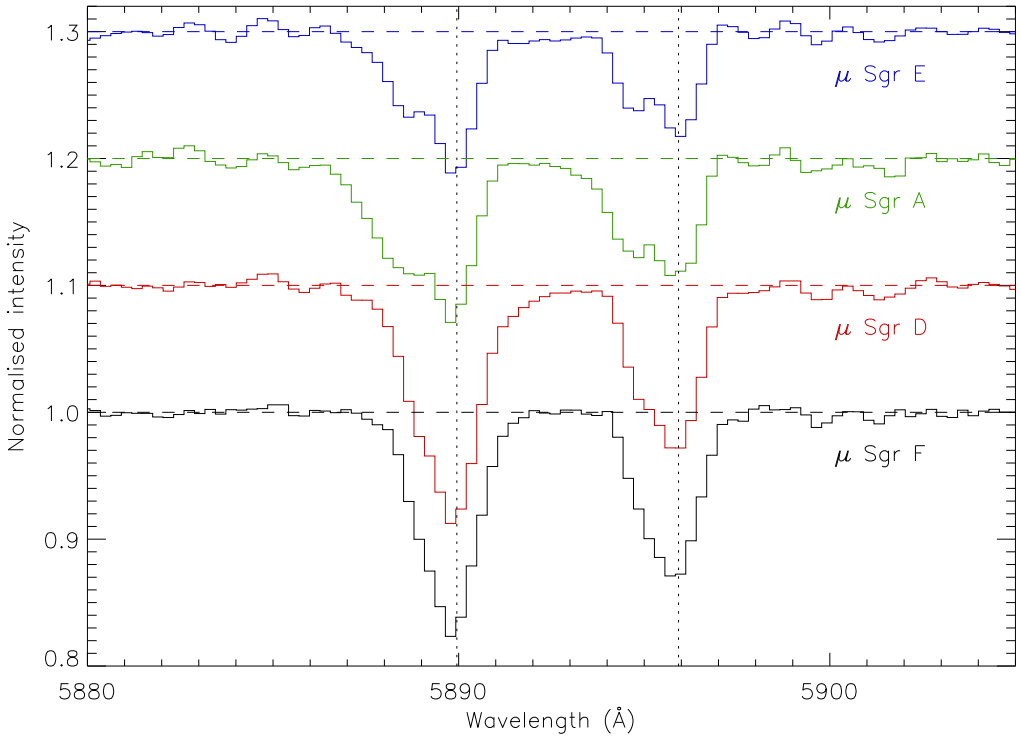

Figure 4.18 – Comparison of the sodium D lines towards μ Sgr. The horizontal dashed lines indicate the continuum levels, whilst the vertical dotted lines indicate the D_1 and D_2 rest wavelengths.

4.1.3.3 μ Sagittarii

Because there are four members of the μ Sgr system, there are six possible ratio spectra. In figures 4.19–4.29, all ratios are given with respect to μ Sgr D. Although this star has a lower signal-to-noise than μ Sgr E, the interstellar absorption is cleaner towards D, and D is located close to the centre of the four stars.

There exists some uncertainty in the distance to the μ Sagittarii system, because of difficulty in finding a consistent set of stellar spectral types, reddening, distance and photometry. μ Sgr A is a known Algol-type eclipsing binary and has H α emission, presumably from circumstellar material, which may have contributed to this uncertainty.

	μ Sgr D	μ Sgr E	μ Sgr F
μ Sgr A	58,000	61,000	212,000

Table 4.3 – Mutual separations in AU between the stars of the μ Sgr system. Errors are difficult to estimate but are at least 10%.

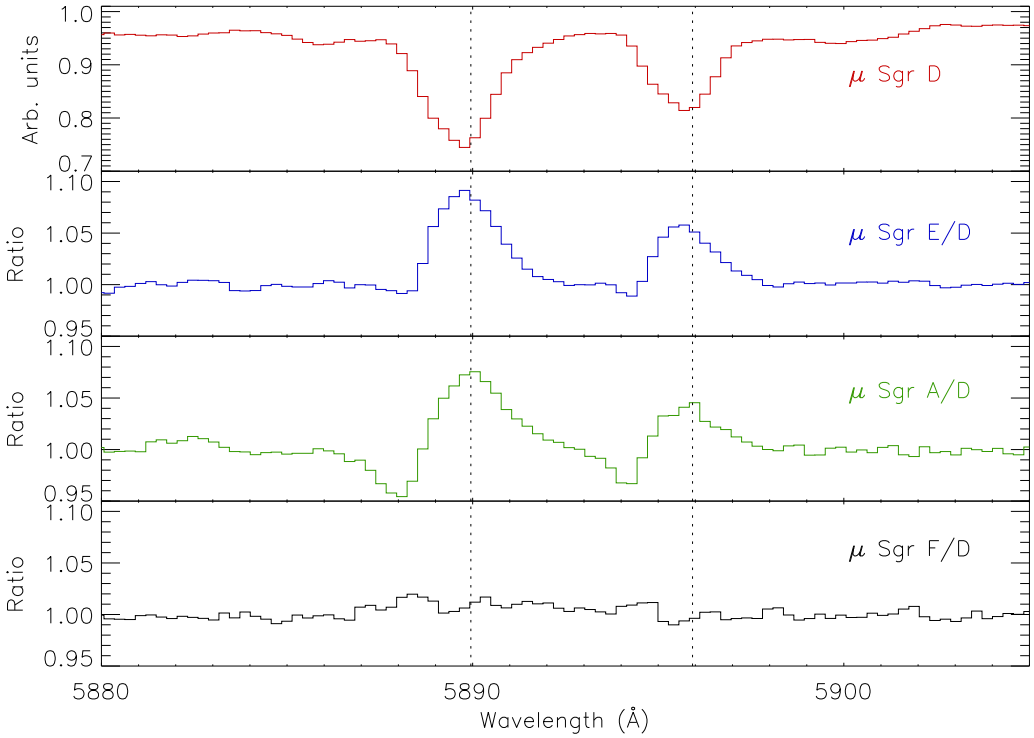

Figure 4.19 – Ratio of the region around the sodium D lines towards μ Sgr. Upper panel: Spectrum of μ Sgr D. Lower three panels: ratio spectra, with respect to μ Sgr D. The vertical dotted lines indicate the D_1 and D_2 rest wavelengths.

Spectral types as widely varying as B2 III and B9.5 Ia have been given for the primary. The Hipparcos parallax for μ Sgr A is 0.11 ± 0.98 mas* (ESA 1997) which provides a 2σ lower limit of $d > 480$ pc; the unusually high uncertainty for a star this bright is presumably due to the multiplicity of the system. Lindroos (1985) derived a distance of $d = 1.3$ kpc, whilst Abt (1986) used a completely different set of spectral types (and reddening) but nevertheless derived an almost identical distance of $d = 1.2$ kpc. These distances appear to be consistent with a location in the Sgr OB1 association. Here the spectral types and distance determined by Lindroos (1985) have been adopted, with the caveat that these remain considerably uncertain. At this distance, the projected separations between the members of the system are given in table 4.3.

The major multiple-star catalogues list five components of the μ Sgr system: A–E (ESA 1997; Dommanget and Nys 2000; Mason et al. 2001). The star BD -21°4905, which is here referred to as μ Sgr F, has previously been assigned to a separate binary system (CCDM 18136-2102, as member A) located ∼ 3′ from μ Sgr A. The Tycho-

*milliarcsecond

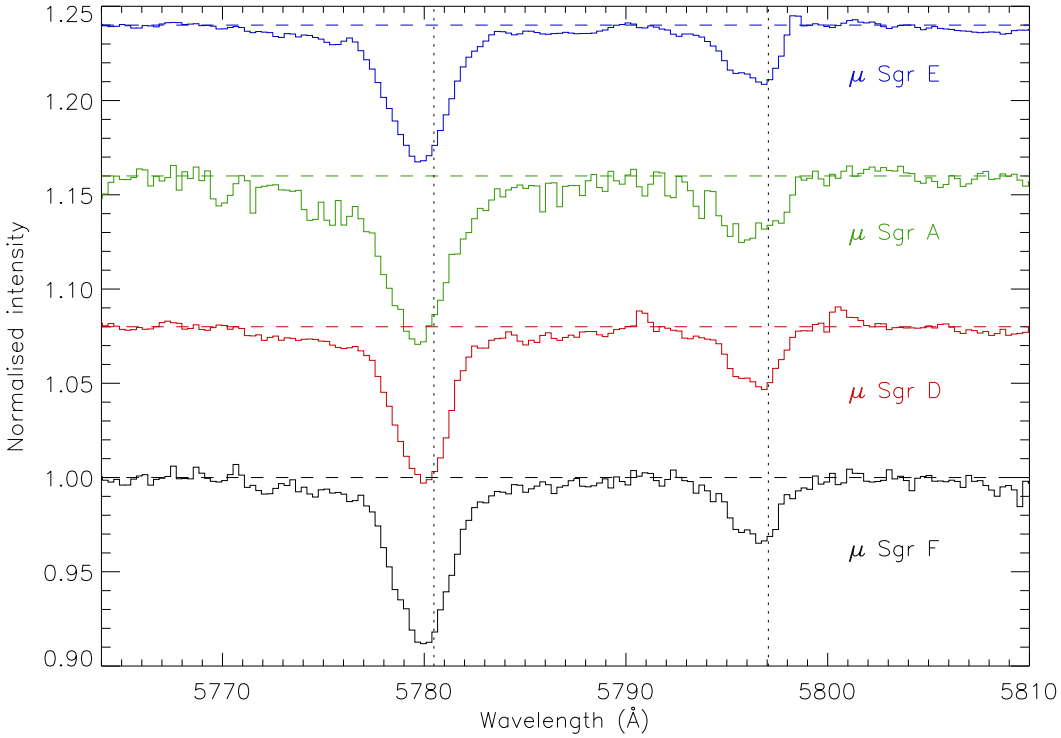

Figure 4.20 – Comparison of the $\lambda\lambda$5780 and 5797 DIBs towards μ Sgr. The horizontal dashed line indicates the continuum level, whilst the vertical dotted lines indicate the DIB rest wavelengths.

2 photometry for this star is $B = 10.87 \pm 0.06, V = 10.67 \pm 0.08$ (Høg et al. 2000). Taking $E_{(B-V)} = 0.24$ (Lindroos 1985) and the intrinsic colours of Fitzgerald (1970), this is consistent with a B7–A0 dwarf located at the distance of μ Sgr. The photometry is also consistent with background giant or supergiant at slightly earlier spectral types (B4–B8 for luminosity class Ia), but the similarity in interstellar absorption, particularly with μ Sgr D (see below), appears to rule this out. Unfortunately the RSS spectra do not cover the standard MK classification wavelength region. The only strong stellar lines observed are the He I 5876 Å and H α 6562 Å lines, however their strengths are consistent with a mid–late B-type dwarf (Leone and Lanzafame 1997, the He I lines are shown in figure 4.30). The absence of any metal lines excludes spectral types later than early A, whilst the widths of the He and H lines rule out the possibility of a background supergiant (C Evans, private communication). The spectral type is therefore probably 'late B dwarf', so BD -21°4905 is provisionally assigned to the μ Sgr system as μ Sgr F. However, accurate spectroscopic confirmation of the spectral type and the measurement of radial velocities is needed to confirm this assignment. CCDM 18136-2102B, which

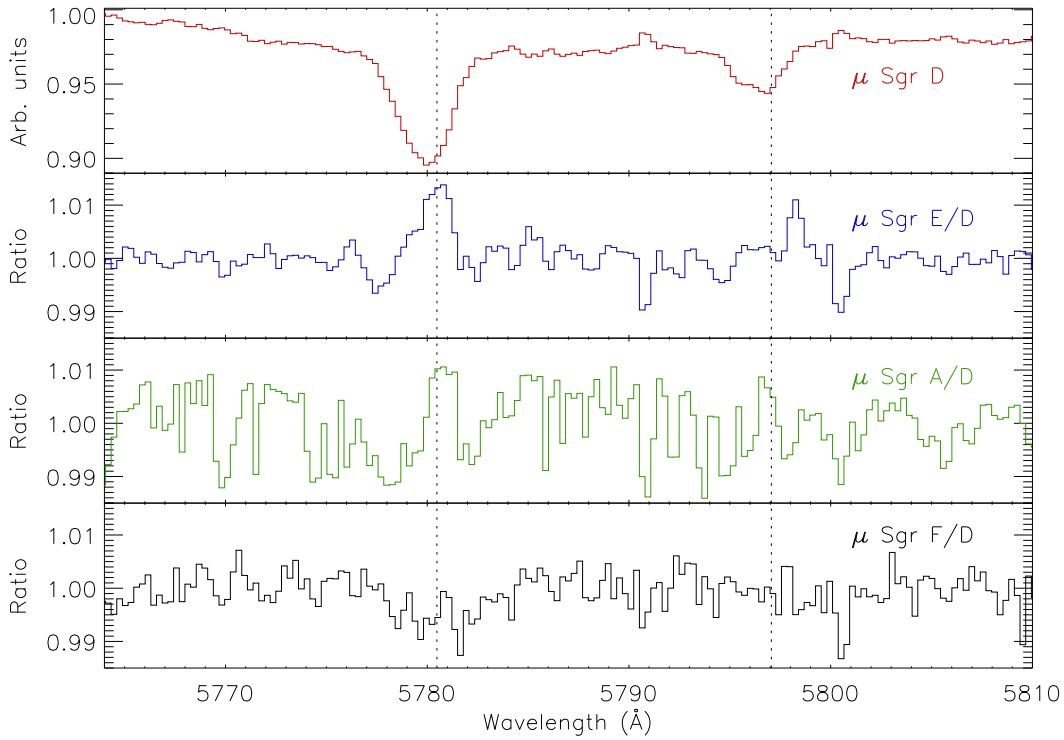

Figure 4.21 – Ratio of the region around the $\lambda\lambda$5780 and 5797 DIBs towards μ Sgr. Upper panel: Spectrum of μ Sgr D. Lower three panels: ratio spectra, with respect to μ Sgr D. The vertical dotted lines indicate the DIB rest wavelengths.

has already been assigned as a physical binary with μ Sgr F by Dommanget and Nys (2000) and Mason et al. (2001), is tentatively assigned the designation μ Sgr G, though this is highly uncertain.

The brightness of μ Sgr A has led to its inclusion in a number of very-high resolution interstellar absorption surveys. Although these studies are only available for one of the four sightlines, they may be used to illustrate the nature of the interstellar material towards the system. Kerr et al. (1996, 1998) observed fine structure within the λ5797 and λ6613 DIBs towards this star, the first such observation within any DIB. Those authors found that λ6613 was much narrower towards μ Sgr than the other stars in their sample. Crane et al. (1995) detected both CH and CH^+, in two absorption components: a main narrow absorption at $-5.7\,\mathrm{km\,s^{-1}}$, and a weaker, broader component at around $-8\,\mathrm{km\,s^{-1}}$. Lambert and Danks (1986) detected Ca I at velocities of -5.8 and $-10.6\,\mathrm{km\,s^{-1}}$. Welty and Hobbs (2001) and Welty et al. (2003) detected K I and Fe I at corresponding velocities, and found two additional weaker components around -10 and $-4\,\mathrm{km\,s^{-1}}$. Unpublished spectra from D Welty show even more clouds in Ca II and Na I,

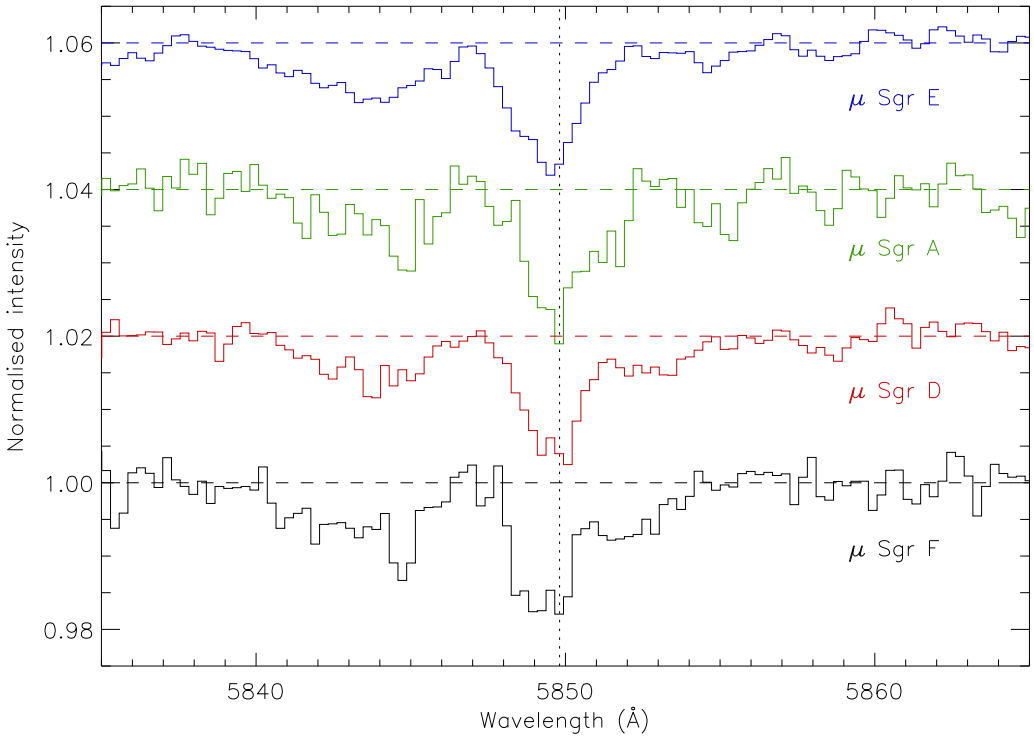

Figure 4.22 – Comparison of the λ5850 DIB towards μ Sgr. The horizontal dashed line indicates the continuum level, whilst the vertical dotted line indicates the DIB rest wavelength.. The λ5844 DIB is also visible.

extending to both more negative and more positive velocities.

The presence of high negative velocity Na I absorption seen in the RSS spectra towards μ Sgr A and E but not D and F indicates an additional cloud of material towards the south-west of the system (c.f. figure 4.3). However, none of the DIBs show any corresponding new components, although these would only be obvious for the narrower DIBs. It therefore seems likely that this cloud does not host DIB carriers. The lack of CH, CH^+ and Ca I, together with the width seen in the high-resolution Na I spectrum, suggests that this cloud consists of warmer material, perhaps a cloud of warm neutral medium.

4.1.4 Conclusions

Long-slit medium-resolution observations have been presented towards two binary and one multiple-star system. The utility of DIBs as probes of SSS is confirmed, and demonstrated at lower resolution than ever before, resulting in a large improvement in ob-

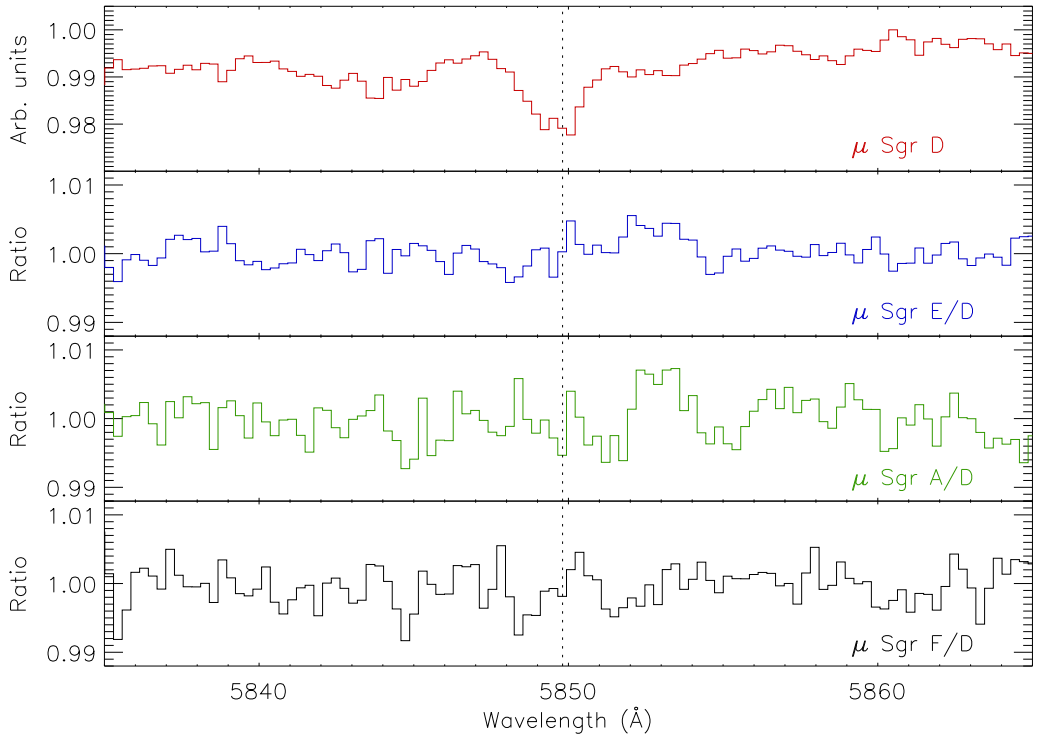

Figure 4.23 – Ratio of the region around the λ5850 DIB towards μ Sgr. Upper panel: Spectrum of μ Sgr D. Lower three panels: ratio spectra, with respect to μ Sgr D. The vertical dotted line indicates the DIB rest wavelength.

serving efficiency and therefore saving in telescope time. Towards HD 176269/70, no interstellar absorption strong enough for SSS studies was detected. However, this also indicates the advantages of using lower resolution, because less than 30 min of telescope time was required to rule out this binary as a suitable SSS target.

Significant DIB and Na I absorption was detected towards the binary HD 168075/6 and four members of the μ Sgr system, one of which was identified as a member of the system for the first time. Variations in absorption between members of each system were detected and confirmed via a ratio technique, which eliminates most of the systematic uncertainties involved in the measurement of equivalent widths. The scales probed are between ~ 50,000 and 200,000 AU. The DIB which exhibits the most variation, both in magnitude and frequency, is λ5780. Although this is one of the stronger DIBs observed, the (relatively) high variation is not simply due to the high equivalent width, because the λ6283 DIB has a far larger equivalent width in all cases but does not exhibit the same degree of variation.

Of particular interest is the discovery that some DIBs vary in opposite senses to each

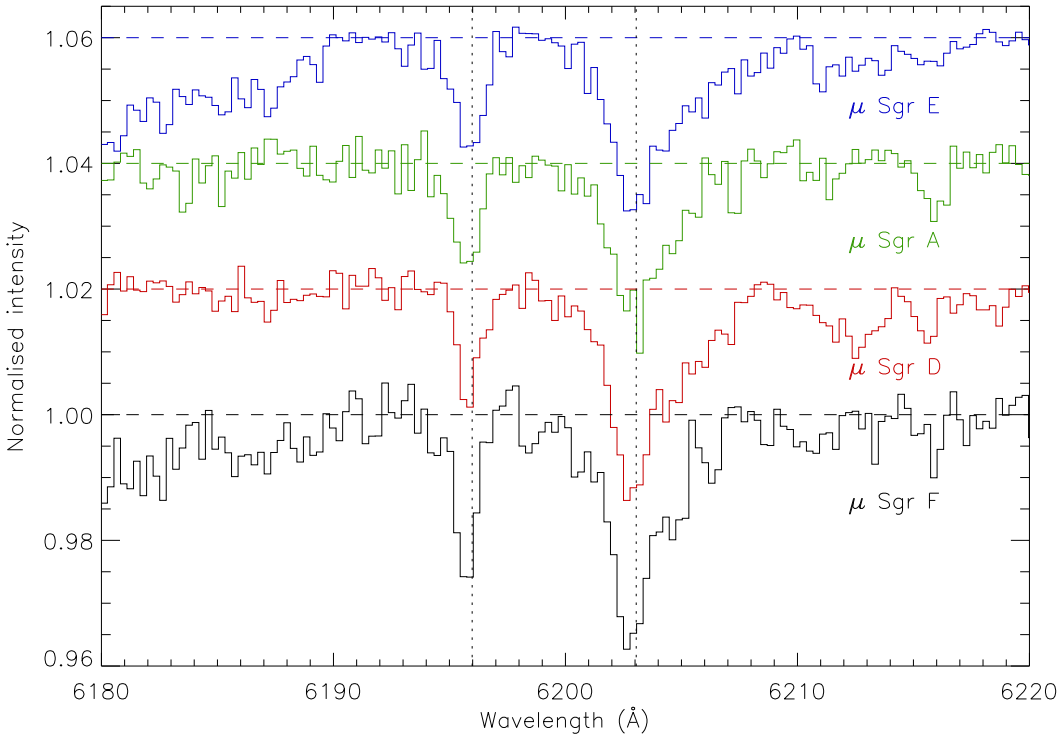

Figure 4.24 – Comparison of the $\lambda\lambda$6196 and 6203 DIBs towards μ Sgr. The horizontal dashed line indicates the continuum level, whilst the vertical dotted lines indicate the DIB rest wavelengths.

other, despite in some cases being members of the same KW group e.g. $\lambda\lambda$5797 and 5850 towards HD 168075/6. Whilst these DIBs tend to vary in concert overly widely separated lines-of-sight (hence their inclusion in the same KW group), the carriers respond in opposite senses to the smaller local changes in (physical or chemical) conditions between two closely-separated sightlines.

Disentangling exactly which changes in local conditions are causing the variations in DIBs cannot be determined from the current observations, and will require high-resolution follow-up. However, the advantage of the DIB technique is that a large number of sightlines may be quickly surveyed, both to determine statistical properties and to select the best targets for high-resolution follow-up; this is discussed further in chapter 6.

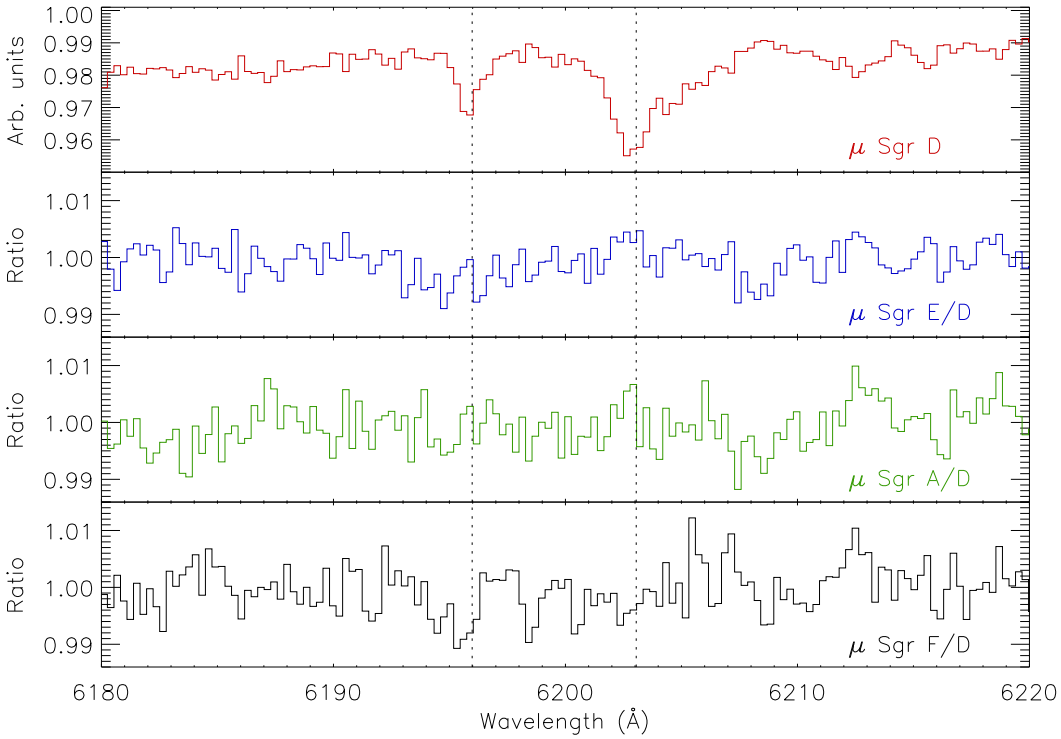

Figure 4.25 – Ratio of the region around the $\lambda\lambda$6196 and 6203 DIBs towards μ Sgr. Upper panel: Spectrum of μ Sgr D. Lower three panels: ratio spectra, with respect to μ Sgr D. The vertical dotted lines indicate the DIB rest wavelengths.

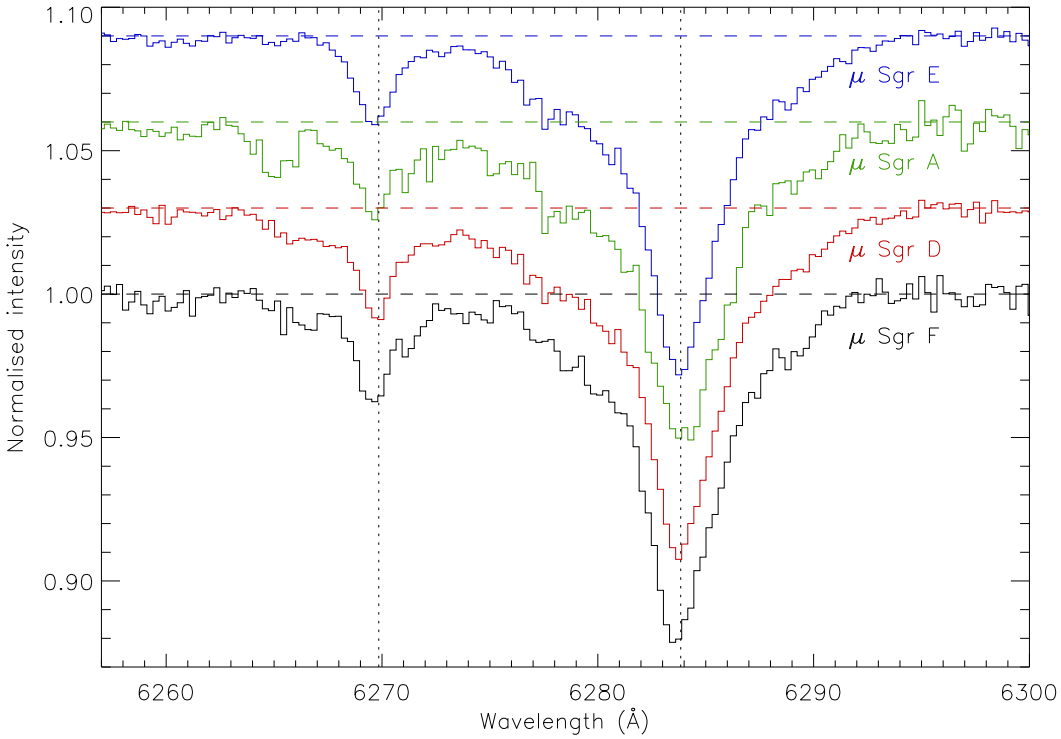

Figure 4.26 – Comparison of the $\lambda\lambda$6269 and 6283 DIBs towards μ Sgr. The horizontal dashed line indicates the continuum level, whilst the vertical dotted lines indicate the DIB rest wavelengths.

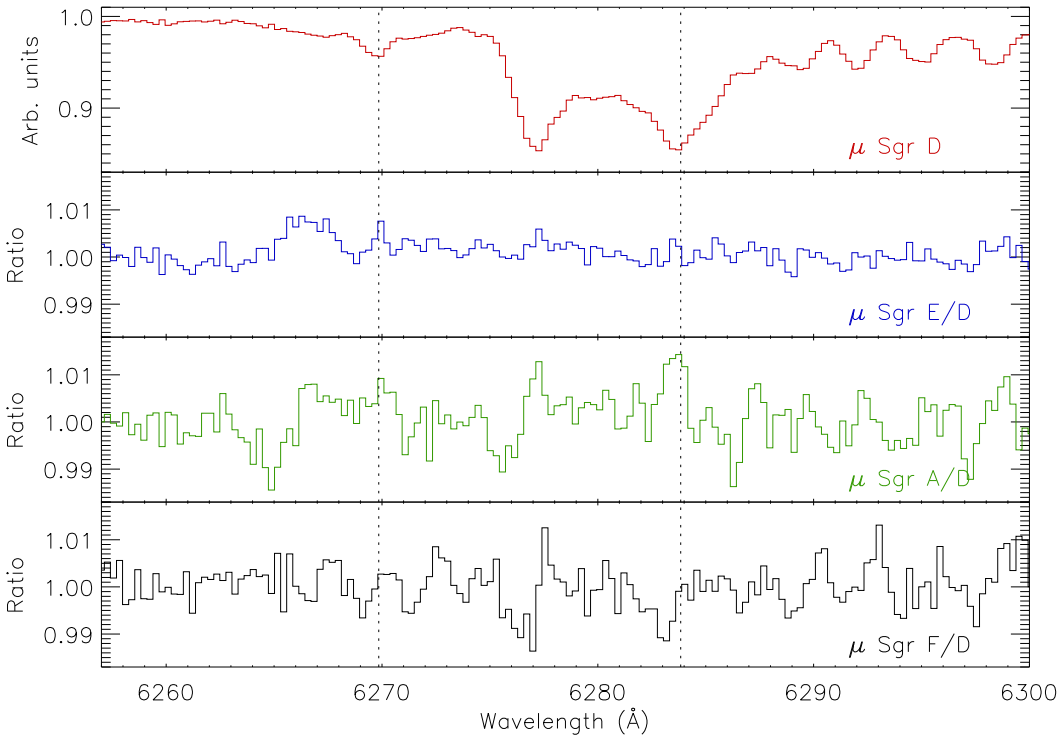

Figure 4.27 – Ratio of the region around the $\lambda\lambda$6269 and 6283 DIBs towards μ Sgr. Upper panel: Spectrum of μ Sgr D. Lower three panels: ratio spectra, with respect to μ Sgr D. The vertical dotted lines indicate the DIB rest wavelengths.

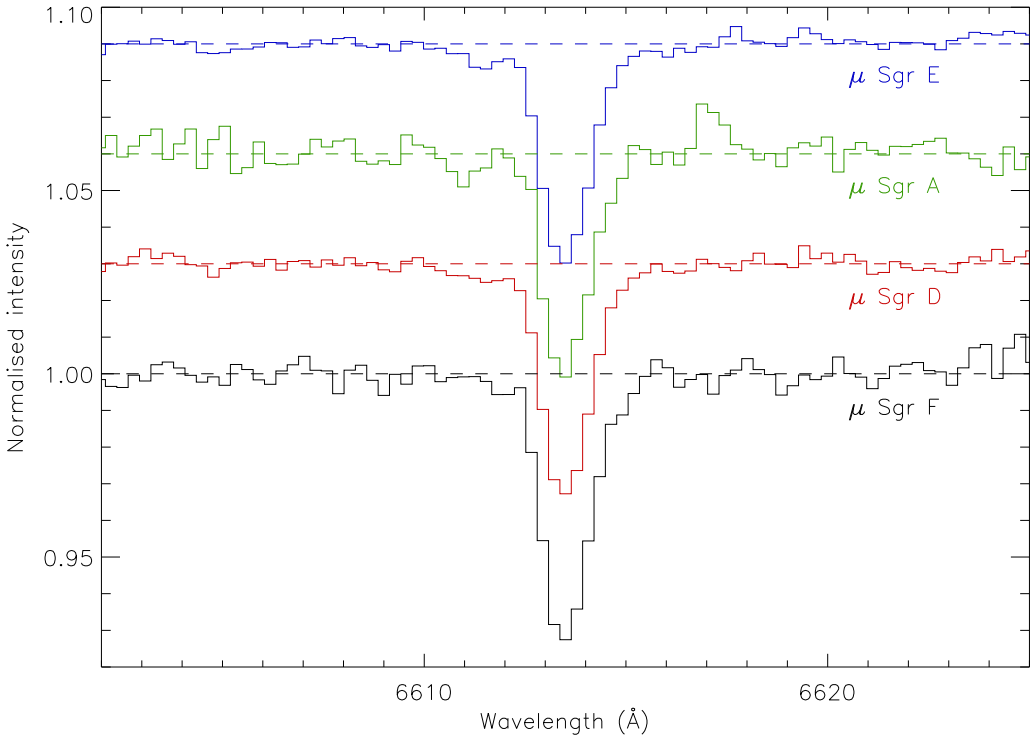

Figure 4.28 – Comparison of the λ6613 DIB towards μ Sgr. The horizontal dashed line indicates the continuum level, whilst the vertical dotted line indicates the DIB rest wavelength.

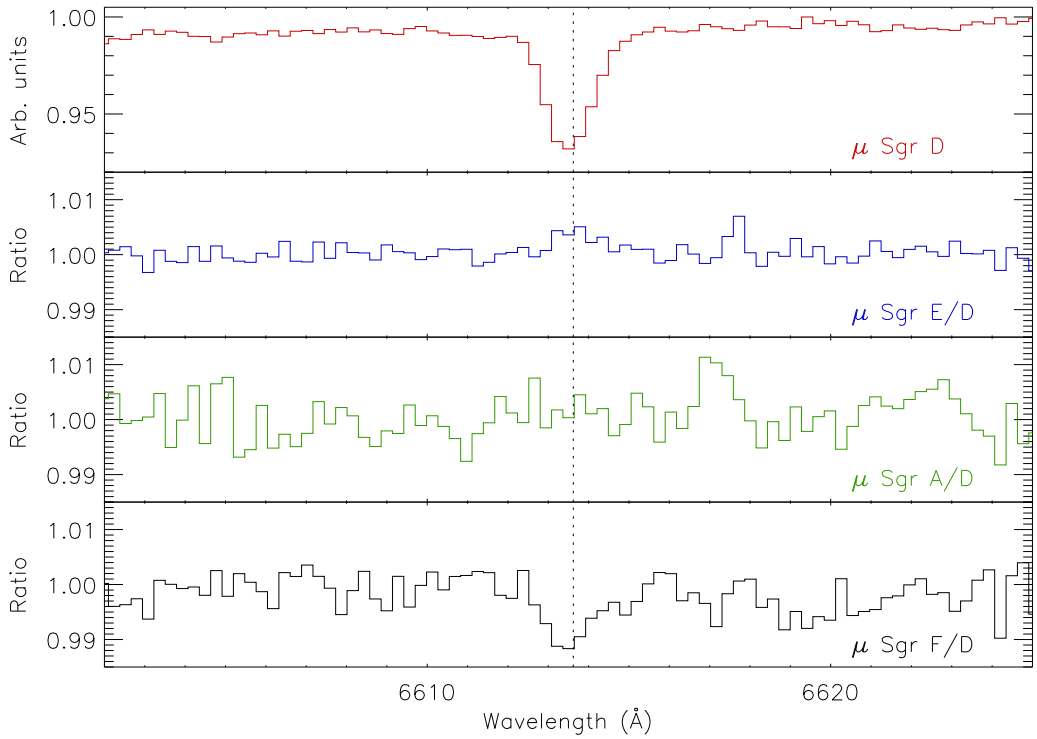

Figure 4.29 – Ratio of the region around the λ6613 DIB towards μ Sgr. Upper panel: Spectrum of μ Sgr D. Lower three panels: ratio spectra, with respect to μ Sgr D. The vertical dotted line indicates the DIB rest wavelength.

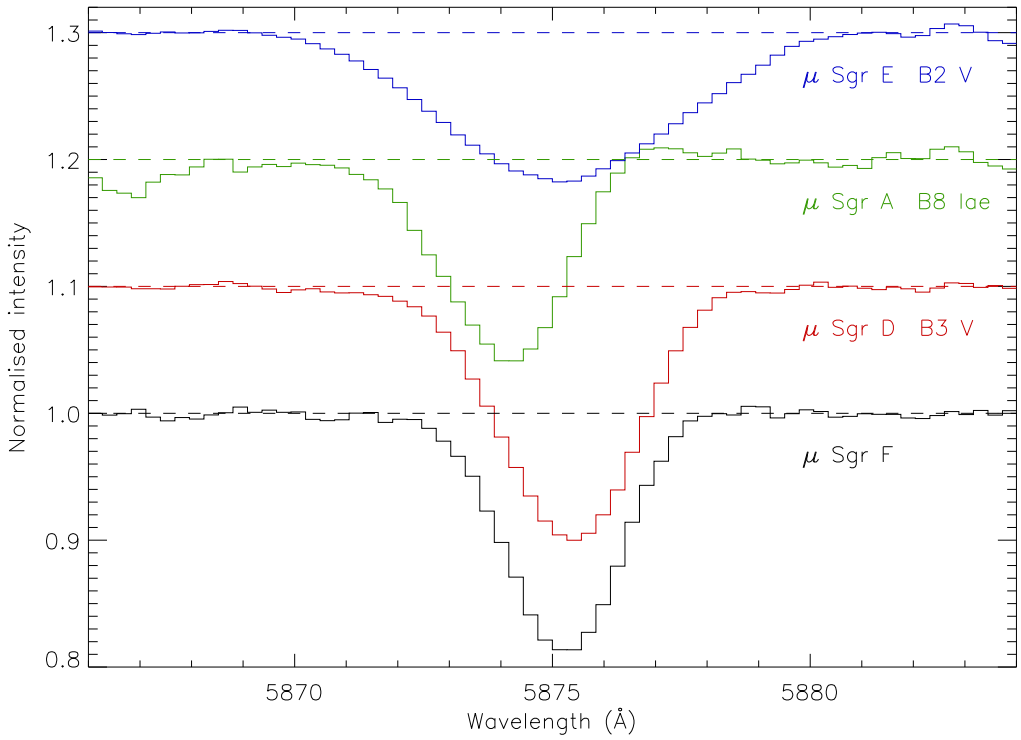

Figure 4.30 – The He I D_3 lines observed in the stars of the μ Sgr system. μ Sgr F is thought to be a late-B dwarf (see text).

4.2 Multi-object spectroscopy of interstellar absorption towards ω Centauri

The research described in this section has been published in *Monthly Notices of the Royal Astronomical Society*: J Th van Loon, K T Smith et al., *Detailed maps of interstellar clouds in front of ω Centauri: Small-scale structures in the Galactic Disc–Halo interface*, **399**, 195, 2009 (van Loon et al. 2009)

The main limitation of all absorption line studies of the ISM is the availability of suitable background sources. This problem is particularly acute for studies of small-scale structure, because it is necessary to sample a number of closely-spaced lines-of-sight. One solution to this problem is to utilise background sources which are intrinsically extended. Radio observations of H I gas in front of extended radio sources such as 3C 147 provided some of the earliest evidence for small-scale structure in the ISM, and probe scales as small as 10 AU (Lazio et al. 2009). Unfortunately, there are only a handful of radio sources in the sky which are both extended and bright enough for these studies.

In theory, external galaxies could be used as background sources. There are however a number of difficulties with this idea. The integrated spectrum of an entire stellar population is highly complex and unsuitable for measuring interstellar absorption, which restricts observations to individually resolved early-type stars in nearby galaxies. Such stars are faint, which severely restricts the signal-to-noise which may be achieved (c.f. chapter 5). The location of nearby galaxies away from the galactic plane results in a dearth of intervening interstellar material within the Milky Way, resulting in weak foreground absorption. Finally, it is impossible to define the distance at which the foreground absorption occurs, so information on the scale of the hypothetical variations is lost.

For these reasons, all optical observations of SSS towards extended sources have utilised star clusters as background sources – prior to the work described below, five such studies have been published. The first observations of variable interstellar absorption towards clusters were performed by Langer et al. (1990), who found spatial variations in ISM absorption towards ten stars in M92 and seven stars in M15. These results were extended below the 0.2 pc cut-off of Crovisier et al. (1985) by Kemp et al. (1993), who used 16 stars in the globular cluster M4 to probe SSS in the ρ Oph cloud and Loop I Bubble on scales of $\sim 2,000$ AU. Meyer and Lauroesch (1999) performed integral field spectroscopy on the core of M15 and detected variations in interstellar structure in two

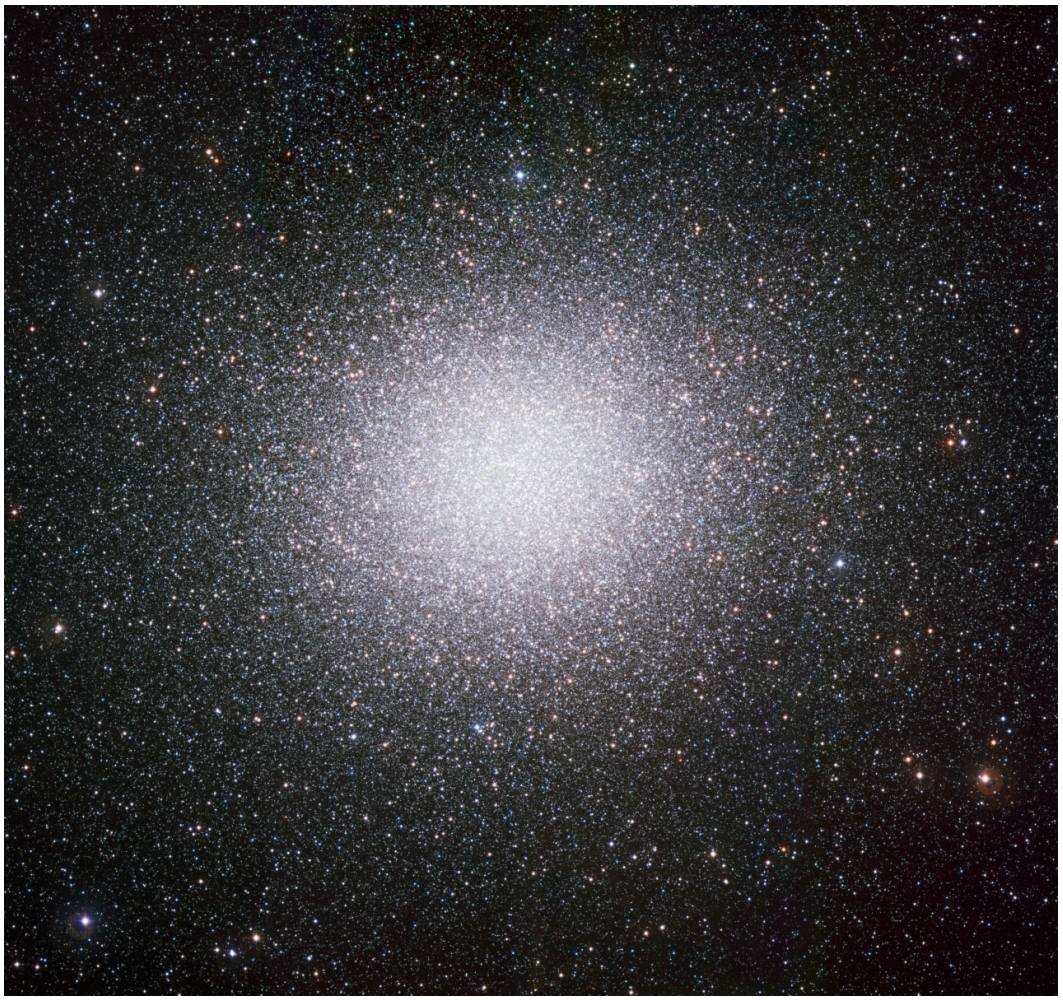

Figure 4.31 – The globular cluster ω Cen. Image is a *BVI* colour composite, copyright European Southern Observatory, used under license.

distinct intervening layers. Andrews et al. (2001) used the same technique to sample the core of M92, detecting two absorbing clouds whose Na I column densities varied over scales of 1,600 and 3,200 AU respectively; over the full $27 \times 43''$ field of view the column density was seen to vary by factors of 4 and 7 respectively. Most recently, Points et al. (2004) used 150 stars in the double open cluster h & χ Per to probe absorption in the Perseus spiral arm on larger scales of 0.1–50 pc and found differences between *all* pairs of stars in their sample. Points et al. (2004) also made the first use of DIBs in SSS observations, observing the λ5797 DIB towards three of their target stars from which the presence of a dense CNM cloud was inferred.

The globular cluster ω Centauri offers an ideal opportunity to extend these studies. ω Cen is the most massive known globular cluster, and one of the closest to the Sun ($M \sim 2.5 \times 10^6\, M_\odot$ van de Ven et al. 2006, $d = 5$ kpc McDonald et al. 2009). As a

result, there exist within the cluster a large number of bright, metal-poor hot horizontal branch stars, which are excellent background sources for ISM studies due to their clean photospheric spectra. The large retrograde motion and tight velocity dispersion of the cluster ($v_{\rm LSR} \approx 229\,{\rm km\,s^{-1}}$, $\sigma v \approx 12\,{\rm km\,s^{-1}}$) ensure that the weak photospheric absorption which is present is well displaced from the interstellar absorption.

The research described in this section arose from a collaborative project; therefore only a brief description is given below, full details, including data tables, can be found in van Loon et al. (2009).

4.2.1 Observations

Spectra of several hundred stars located in ω Cen were obtained using the AAOmega multi-object spectrograph on the 3.9 m Anglo-Australian Telescope. The observations were performed in service mode by R Sharp (AAO) on the night of 2008 March 28. The AAOmega bench-mounted spectrograph was fed by the Two Degree Field (2dF) fibre positioner located at the prime focus of the AAT (Saunders et al. 2004; Sharp et al. 2006). The targets were hot horizontal branch stars selected from the survey of van Leeuwen et al. (2000). Two fibre setups were employed to ensure good coverage throughout the cluster, resulting in a total of four hundred and fifty-two targets observed, more than any previous ISM mapping experiment. The stars cover a field with a diameter of 1° and mutual separations > 1′.

AAOmega is a dual-beam spectrograph, with the two arms separated by a dichroic mirror operating at 5700 Å. The blue arm was used with the 3200B grating, providing a wavelength coverage of ∼ 3890 – 4170 Å at a spectral resolution of $R \sim 8200$. The red arm utilised the 2000R grating, which resulted in a wavelength coverage of ∼ 5740 – 6220 Å at $R \sim 7250$. The primary targets were the interstellar Ca II H & K and Na I D lines.

Data reduction (using the `2dfdr` pipeline) was performed by J van Loon (Keele); the author was primarily involved in the interpretation and analysis. Full details of the observations and data reduction are given in van Loon et al. (2009). The final per pixel signal-to-noise ratio of each spectrum was around 30–50 at the Ca II K line and 60–100 at the Na I D_2 line.

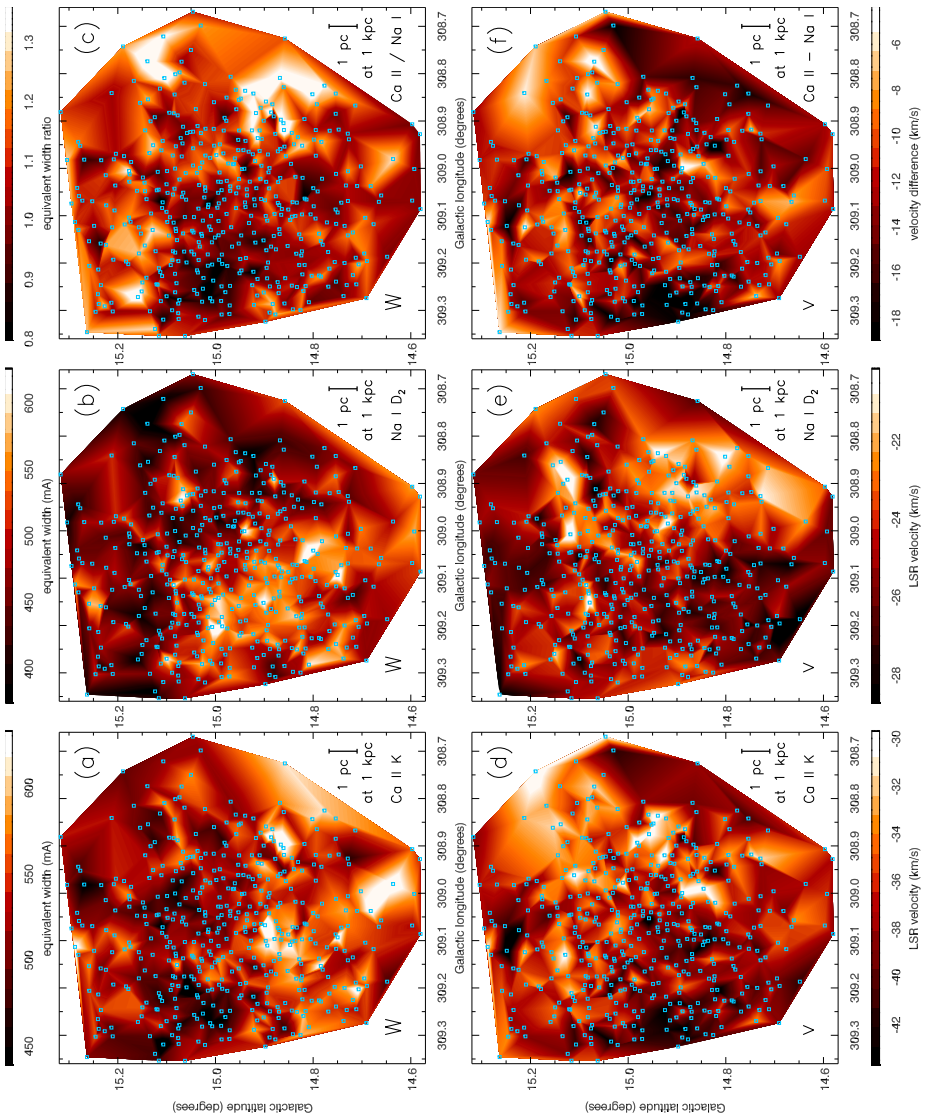

Figure 4.32 – Maps of interstellar Na I and Ca II absorption towards ω Cen, on galactic coordinates. Equivalent widths of Ca II (a), Na I (b) and their ratio (c) are plotted in the top row. On the bottom row, the corresponding velocities of Ca II (d) and Na I (e) together with the difference in velocity (f) are shown. Blue squares indicate the location of the stellar probes. Values are shown on a nearest-neighbour linear interpolation, covering the range of $\pm 2\sigma$ about the median value. Reproduced with permission from van Loon et al. (2009).

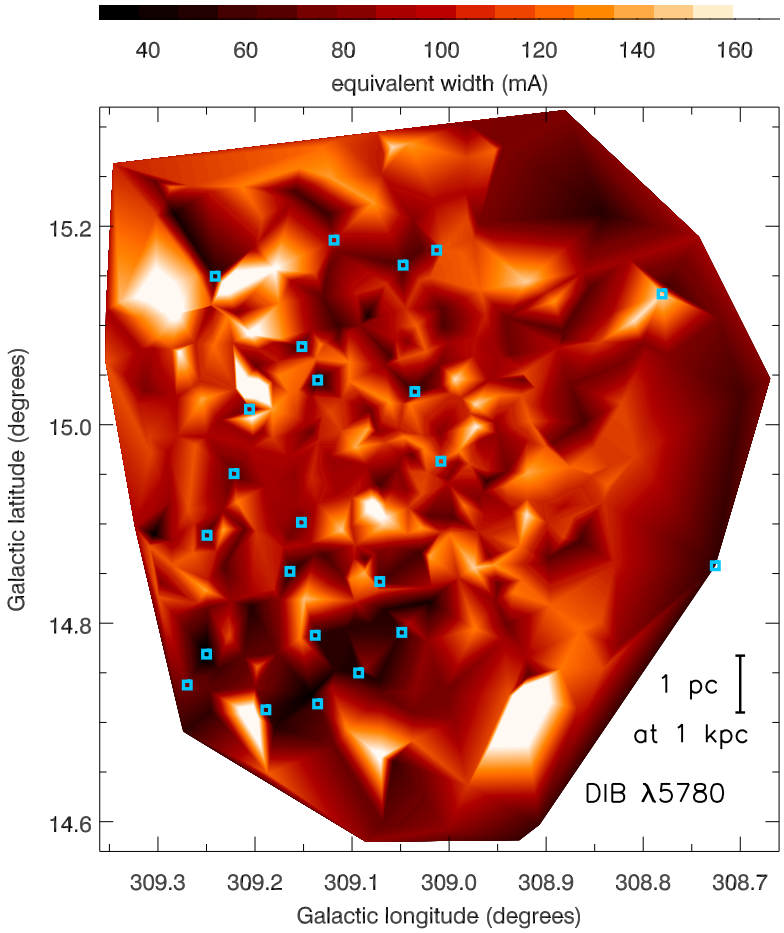

Figure 4.33 – Map of λ5780 DIB absorption towards ω Cen, plotted on galactic coordinates. The equivalent width is shown on a nearest-neighbour linear interpolation, covering the range of $\pm 2\sigma$ about the median value. Blue squares indicate lines of sight with $\log(\lambda 5797/\lambda 5780) > -0.2$. Reproduced with permission from van Loon et al. (2009).

4.2.2 Results

The interstellar Ca II H line overlaps the strong photospheric H ζ line, whilst the interstellar Na I D_1 line overlaps the weak redshifted photospheric Na I D_2 line, so the interstellar Ca II K and Na I D_2 lines were selected for analysis. The λλ5780 and 5797 DIBs were also present in the red arm spectra, and subjected to the same analysis. The λλ6196 and 6203 DIBs were also detected, but this wavelength region was only covered in a small number of spectra and so these DIBs were not investigated. The measured interstellar Ca II K and Na I D_2 lines are shown in figure 4.32; the DIBs are shown in figure 4.33.

The measured equivalent widths of the Ca II and Na I lines vary significantly across the field, by up to a factor of two. For Ca II, the range was 383–709 mÅ, with a mean of

536 mÅ and typical uncertainty of 25 mÅ. For Na I, the range was 350–682 mÅ, with a mean of 500 mÅ and typical uncertainty of 20 mÅ. The overall variation shown in figure 4.32 are therefore large with respect to the uncertainties, but smaller variations between neighbouring stars are sometimes comparable to the uncertainties. Taking into account the associated uncertainties and the standard deviations in the measured distributions, the variations seen in Na I are approximately twice as strong as those in Ca II, with real fluctuations of $\sim 12\%$ and $\sim 7\%$ respectively (1σ). The variations in λ5780 equivalent width across the field are comparable to those seen in the atomic species, but with substantially larger relative uncertainties. The λ5797 measurements were too noisy for a statistically significant measure of their variations to be obtained.

The FWHMs of the atomic lines are far larger than would be expected from thermal or turbulent broadening, which is evidence for multiple unresolved velocity components along the line-of-sight. The relatively low reddening of the cluster ($E_{(B-V)} \approx 0.08$, McDonald et al. 2009) provides confidence that none of the components is likely to be optically thick and thus the equivalent widths map linearly to column densities. Although there are variations in line ratio across the map, the λ5780 DIB is distributed more similarly to Ca II than Na I. Although the $\lambda5780/\lambda5797$ ratio indicates a σ-type environment across the vast majority of the map, some individual lines-of-sight have $\lambda5780/\lambda5797$ ratios consistent with ζ-type clouds.

Comparison of the atomic lines to dust distribution as seen in Spitzer 24 μm maps and the Schlegel et al. (1998) reddening maps (see section 5.3.2) indicates that the dust distribution is far more uniform than the observed atomic lines. This is not merely an artefact of the lower resolution of the dust maps, because both dust and atomic maps can be used to de-redden the ω Cen colour-magnitude diagram of the targets; using the dust map results in a much cleaner colour-magnitude diagram (for full details of this procedure, see van Loon et al. 2009).

4.2.3 Discussion & conclusions

The interstellar path to ω Cen passes through the Local Bubble for ~ 100 pc, then through the disc of the galaxy for another ~ 1 kpc, before entering the galactic halo for the remaining ~ 4 kpc (Lallement et al. 2003). Calcium is a highly refractory element and is easily depleted onto dust grains. The relatively high Ca II/Na I ratio across the whole cluster indicates that most of the the interstellar absorption is occurring in warm interstellar media, at $T \sim 5,000$–$7,000$ K. From an analysis of the velocities and an

assumed flat Milky Way rotation curve, the majority of the absorption probably arises from gas at the disc-halo interface, at around the distance of the Carina-Sagittarius spiral arm. This region has been little-studied in the past, due to a lack of suitable background sources. The small-scale variations seen in Na I and the presence of some ζ-type lines-of-sight indicates that some small clumpy or filamentary clouds of colder material exist, though these may be confined to the foreground of the absorption, within the disc of the MW. If the absorption is indeed mostly located at the disc-halo interface, the scales probed are around 0.2–10 pc (see scale bars on figure 4.32 and figure 4.33, which were calculated assuming a distance of 1 kpc).

The moderately high equivalent widths of the λ5780 DIB indicate that the carrier is capable of surviving in the warm neutral medium. The temperature, electron density and UV field are much higher in such environments than in the diffuse media where DIBs are commonly observed. The carrier must be relatively resilient to these conditions. The presence of some ζ-type lines-of-sight provides evidence for the presence of some cooler material, which would not be evident from the atomic lines alone. DIBs therefore supply useful additional information for studies of interstellar small-scale-structure, which would not be otherwise available. A fuller description of the results and conclusions are presented in van Loon et al. (2009).

Chapter 5

Diffuse interstellar bands in M33

Some of the research described in this chapter has been published in *Astronomy & Astrophysics*: M A Cordiner, K T Smith et al., *Diffuse interstellar bands in M33*, **492**, L5, 2008 (Cordiner et al. 2008b)

Most of what is known about the diffuse interstellar bands has been learnt from studies of the interstellar medium close to the Sun (within a few kpc). Whilst there are good pragmatic reasons for this, the possibility exists that some of the properties of the DIBs which appear to be constant over this relatively small volume in fact vary with local conditions. In particular, the local metallicity and gas-to-dust ratio might be expected to have an effect upon the DIB spectrum.

External galaxies provide a range of interstellar conditions which can be quite different to those found in the Milky Way. Even in case of those ISM properties which do exist in some parts of the MW, it may be more straightforward to study external galaxies (particularly face-on spirals) where it is easier to disentangle foreground absorption and the problems of multiple clouds may be avoided. Other galaxies may be used as astrochemical laboratories to study the effect of local interstellar conditions on the chemical make-up of the gas and dust, including the diffuse interstellar bands. Potentially, this could lead to new insights into the behaviour of the DIB carriers which could assist in their eventual identification. Some properties of DIBs may prove to be useful astrophysical probes for use in extragalactic astrophysics, despite their unknown carriers.

In this chapter, multi-object spectroscopy is presented for 43 stars located in the M33 galaxy, spread across the disk on scales of ~10 kpc. The first detections of diffuse interstellar bands in this galaxy are reported.

5.1 Diffuse interstellar bands in other galaxies

The first detection of DIBs outside the Milky Way (MW) was made by Walker (1963), who used narrowband imaging to infer the presence of the λ4428 DIB in the spectrum of eight stars in the Small Magellanic Cloud. The first direct spectroscopic detections were made by Hutchings (1964, 1966), who detected λ4428 towards several stars in both Magellanic Clouds. Most studies since have concentrated on the Large and Small Magellanic Clouds (LMC and SMC) due to their proximity and position outside the plane of the MW, and hence ease of observation. Nevertheless, individual stars within the Clouds remain quite faint, limiting the resolution and signal-to-noise which could be achieved, particularly with photographic plates. Early work concentrated on the λ4428 DIB because this has the largest EW of any DIB (for a given line-of-sight) and lies within the wavelength region used for assigning stellar spectral types. However, its large width leads to problems of continuum definition, overlapping stellar and telluric lines, and difficulty in separating the foreground MW contribution.

The first detection of a DIB other than λ4428 was not reported until Pettini and Dodorico (1986) detected λλ6376 and 6379 in the LMC. The difficulties posed by the faintness of the background sources may be overcome by observing the ISM towards a supernova when these events occur in nearby galaxies. The great brightness of SN 1987A (peaking at $V \sim 3$) allowed Vladilo et al. (1987) to detect λλ5780, 5797 and 6283 in the LMC, together with tentative detections of λλ5778 and 6379. SN 1986G in the active galaxy Centaurus A was used by Rich (1987) to make the first detection of DIBs beyond the Magellanic Clouds, and indeed the Local Group; λλ5780, 5797, 6283 and 6613 were detected. Some time later, Heckman and Lehnert (2000) detected λλ5780 and 6283 in a sample of seven dusty starburst galaxies, including M82, and made tentative detections of several other DIBs. A review of extragalactic DIBs was given by Snow (2002), who found that only 13 papers had been published on the subject, of which seven concerned λ4428 in the Magellanic Clouds.

Over the past seven years the field has expanded rapidly. High-resolution spectrographs mounted on 8 m telescopes have been used to obtain new observations of DIBs in both Magellanic clouds (Ehrenfreund et al. 2002; Welty et al. 2006; Cox et al. 2006, 2007b) and towards several supernovae (Sollerman et al. 2005; Cox and Patat 2008; Thöne et al. 2009). DIBs have been detected in more distant objects, including a $z = 0.16$ Ca II absorber in front of a quasi-stellar object (QSO) (Ellison et al. 2008) and a $z = 0.5$ damped Lyman-α (DLA) system (York et al. 2006; Lawton et al. 2008), whilst

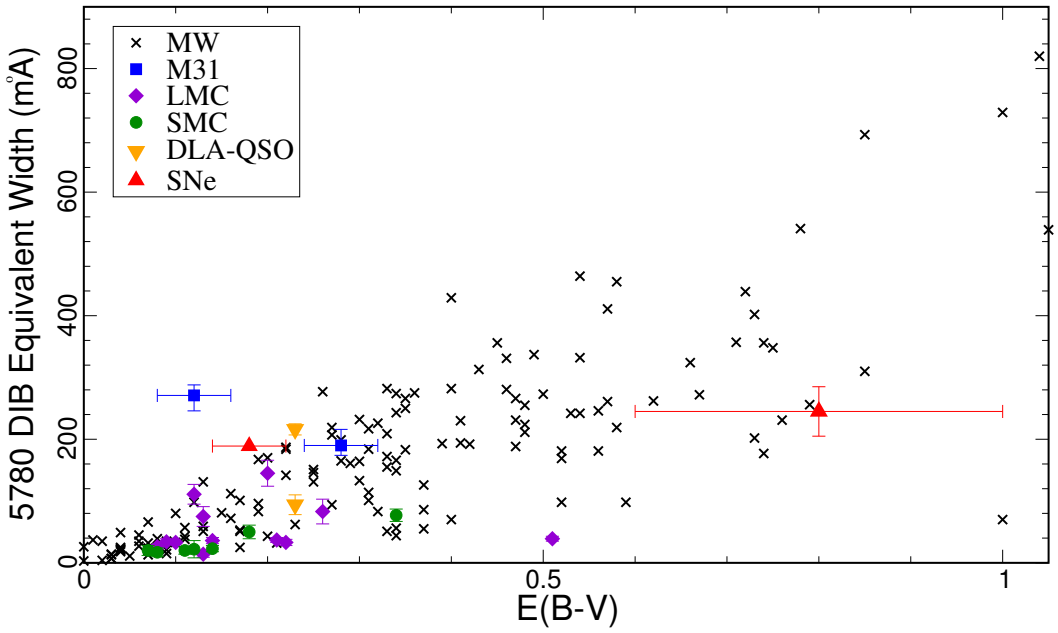

Figure 5.1 – Previous detections of the λ5780 DIB in other galaxies, plotted against $E_{(B-V)}$. MW data are from Herbig (1993); Thorburn et al. (2003); Megier et al. (2005) and Cordiner (2006), whilst the extragalactic data are from Cordiner et al. (2008a) for M31, Cox et al. (2006) for the LMC, Cox et al. (2007b) for the SMC, Ellison et al. (2008) for the QSO, Lawton et al. (2008) for the DLA, and Sollerman et al. (2005) and Cox and Patat (2008) for the SNe.

tight upper limits have been derived for other intermediate-redshift absorbers. Finally, Cordiner et al. (2008a) detected several DIBs towards two stars in M31.

Perhaps surprisingly, the majority of these detections were not obtained in order to study the DIBs themselves, but as proxies for properties along the line of sight. In particular, the DIB-$E_{(B-V)}$ relationships have been used to estimate $E_{(B-V)}$ towards sources for which this would be difficult or impossible by conventional means. These are generally sources for which the intrinsic $(B-V)_0$ colours are unknown, such as SNe and DLAs. This technique is also applied to sources within the Milky Way that have similarly uncertain colours, such as variable stars and those of unusual spectral type (e.g Kiss et al. 2001; Crowther and Evans 2009).

The DIB which has been most widely utilised as a proxy for $E_{(B-V)}$ is λ5780, which is also the DIB with the most extragalactic detections reported in the literature. The variation of the equivalent width of this DIB with $E_{(B-V)}$ is shown in figure 5.1 for a sample of MW targets and all extragalactic detections available in the literature prior to the work presented in this chapter.

Desirable characteristics for targets for further study of extragalactic DIBs include:

- Proximity, so individual stars may be resolved and stars remain relatively bright to keep down exposure times
- High numbers of early type stars to act as background sources of illumination
- Low Milky Way foreground absorption and extinction
- Radial velocity $\gtrsim 100\,\mathrm{km\,s^{-1}}$ so absorption lines arising within the galaxy may be kinematically separated from those in the MW foreground
- Known presence of substantial quantities of neutral gas, to increase the chances of detection
- Projected size which is well-matched to instrumental fields-of-view for multi-object spectroscopy
- A wide range of complementary data available in the literature, such as metallicity gradients, H I maps, UV imaging etc.

Amongst the nearby galaxies of the Local Group, the various dwarf satellites of the Milky Way (such as the Fornax and Carina dwarfs) and the ellipticals M32 and M110 contain little gas and few early-type stars. The nearby Magellanic Clouds have been previously studied (see above), at high resolution towards a relatively small number of targets. The low strength of DIBs (per unit $E_{(B-V)}$) in the SMC in particular suggest a possible dependence on metallicity and/or UV field. The interstellar environment of the SMC is atypical, whilst the low DIB strength is a challenge for detection. It is therefore desirable to extend DIB research to more galaxies, particularly those with more typical interstellar environments. The obvious candidates are the two large spiral galaxies in the Local Group (in addition to the MW) – M31 and M33. Both are located at similar distances, have metallicity approximately solar (but varying across the discs), are located away from the galactic plane (hence low foreground) and have a wealth of complementary data. Of the two, M33 is the preferable target because:

- M33 is viewed face-on, whilst M31 is viewed at high inclination. It is thus easier to disentangle the ISM of M33.
- The Doppler velocity of M33 is consistently more than $-200\,\mathrm{km\,s^{-1}}$ across the whole disc, which provides sufficient offset from the MW. The velocity offset

of M31 varies across the galaxy, and in many cases is insufficient to offset M31 absorption from MW foreground.

- With apparent dimensions $\sim 30' \times 35'$, M33 is well matched to fields-of-view of many multi-object spectrographs. M31 is much larger on the sky, and cannot be fully observed with a single setup.
- There are many more known early-type stars in M33 than M31, as a result of the later galaxy type.

It was therefore decided to extend the study of extragalactic DIBs to M33. The stars in M33 are 10 times more distant than those in the Magellanic Clouds, making high-resolution study prohibitively expensive in terms of telescope time. However, the multiplexing capabilities of multi-object spectrographs at spectral resolution of several thousand means several tens of targets may be studied at this lower resolution simultaneously. Thus a large number of targets in M33 may be studied at low resolution in approximately the same amount of time as required for a handful of Magellanic Cloud targets at high resolution.

5.2 Observations

Forty-three stars located throughout the disc of M33 were observed using the Deep Imaging Multi-Object Spectrograph (DEIMOS) mounted at the right Nasmyth focus of the 10 m Keck II telescope. The observations were carried out by N Przybilla (Erlangen-Nürnberg) on the night of 2003 November 1, as part of a stellar metallicity study. Data reduction and analysis were performed by the author. The targets were selected to be relatively bright ($V < 19$), early-type stars; stellar data is presented in table 5.1

The 1200G grating (blaze = 7500 Å) was used to cover the complete optical spectrum from 3500-9000 Å by observing at two different grating angles. The detector was an 8192×8192 pixel mosaic formed from eight 2048×4096 (15 μm pixels) CCDs arranged 4×2. Two small gaps appear in the wavelength coverage around 4900 and 7400 Å, due to the gaps between the CCD detectors. The CCDs were operated unbinned in the default low gain, fast readout configuration, which provides an RMS readout noise of 2.3–3.3 e^-/pixel (varying between CCDs) and a total readout time of 60 seconds. The large mosaic size results in a considerable data volume of 140 MB per image.

Exposure times were 3×2700 s (2.25 hrs) for the blue setting and 3×2100 s (1.5 hrs) for the red setting. Each slit was 1″ wide (except the two alignment stars which were

4″ wide), whilst the seeing varied from 0.5-0.8″ during the observations. Flat fields were provided by an internal quartz lamp for the red setting, and an illuminated dome screen for the blue. Wavelength calibration was by arc lamps containing Xe, Hg, Ne, Cd and Zn in the blue, and Kr, Xe, Ar and Ne in the red. The resolution was element was approximately constant at $\Delta\lambda \approx 1.7$ Å, which corresponds to resolving powers of $R \sim 2,200$–5,000 over the optical wavelength region.

The data reduction was performed using the `deep2` pipeline* in IDL. The pipeline data products include an optimally extracted 1D spectrum from each CCD for each target, for both grating tilts. Since the spectrum from each slit falls on two CCDs, this results in four spectra per target. These were converted into standard FITS spectra using IDL; further reduction was performed using IRAF. This consisted of combining the separate wavelength regions for each target, Doppler correction to an LSR reference frame, and continuum normalisation. For a small number of targets, the pipeline failed to accurately extract the spectrum. These targets were identified and manually extracted from the intermediate pipeline data products.

*The analysis pipeline used to reduce the DEIMOS data was developed by the DEEP2 team at UC Berkeley with support from NSF grant AST-0071048

Table 5.1 – Stellar data and signal-to-noise obtained for the stars observed in M33. LGGS designations (which contain the coordinates), V magnitudes and $B-V$ colours were taken from the Local Group Galaxies Survey (Massey et al. 2006). Formal errors on V and $B-V$ are 0.004 mag.

Star	LGGS	V	$B-V$	S/N @ 6000Å
0	J013339.18+302934.5	18.622	0.013	40
1	J013347.43+303042.0	17.082	0.783	†
2	J013337.74+304456.3	15.642	1.008	†
3	J013335.14+303600.4	16.429	0.102	125
4	J013335.48+303835.1	17.268	0.016	300
5	*	*	*	100
6	*	*	*	100
7	*	*	*	70
8	J013340.55+303158.7	18.047	-0.039	70
9	J013340.69+304059.8	18.264	-0.037	70
10	J013343.26+303153.8	17.221	0.046	70
11	J013343.34+303534.1	*	*	60
12	J013346.36+303257.5	17.381	0.124	60
13	J013349.22+303809.3	*	*	100
14	J013350.12+304126.6	16.819	0.035	60
15	J013351.20+303224.5	17.194	0.034	90
16	J013351.56+304005.2	17.102	0.039	100
17	J013355.21+303429.9	17.572	-0.009	60
18	J013356.63+303316.4	17.037	-0.043	70
19	J013335.48+303835.1	17.268	0.016	†
20	J013334.98+303852.4	18.076	-0.124	80
21	J013337.09+303521.6	17.937	0.062	50
22	J013340.09+302846.1	16.047	0.118	110
23	J013340.47+303503.3	17.997	0.025	55
24	J013340.48+304256.5	16.427	0.170	40
25	J013340.84+303822.5	18.235	0.172	70

* unreliable photometry, due to e.g. blends with other sources

† no clean continuum for S/N measurement

Continued...

Table 5.1 continued

Star	LGGS	V	$B-V$	S/N @ 6000Å
26	J013341.36+303629.6	17.913	0.106	55
27	J013344.26+303148.0	17.315	-0.086	95
28	J013344.27+304247.2	18.209	0.011	40
29	J013344.43+303843.9	17.941	0.054	120
30	J013344.81+303217.8	18.067	0.025	90
31	J013346.96+303642.8	17.965	0.332	75
32	J013346.92+304325.0	18.128	-0.012	40
33	J013349.56+303941.6	16.753	0.254	125
35	J013346.16+303448.5	17.075	0.186	60
36	J013335.58+302940.8	18.444	0.042	60
37	J013335.45+303010.1	18.628	-0.076	50
38	J013352.16+303333.5	17.959	0.095	75
39	J013339.92+303729.2	18.863	-0.085	55
40	J013347.26+303921.3	18.065	0.221	100
41	J013344.50+304045.9	18.823	-0.059	55
42	J013342.46+304211.1	18.735	0.053	45
43	J013347.55+304347.0	18.641	-0.088	35

5.3 Stellar spectral types and reddening determination

Stellar spectral types were assigned by C Evans (UK ATC) with reference to the standard stars of Evans and Howarth (2003) and Evans et al. (2004). Luminosity classes were assigned on the basis of the H γ equivalent width according to the prescriptions of Evans et al. (2004). The adopted spectral types are given in table 5.2. Spectral types for the two foreground alignment stars are also given; these spectra were subsequently discarded as these stars lie within the MW.

$E_{(B-V)}$ values were determined from the $B-V$ photometry of the Local Group Galaxies Survey (LGGS, Massey et al. 2006, see table 5.1) and the intrinsic $(B-V)_0$ colours given by Fitzgerald (1970). As Fitzgerald does not present intrinsic colours for O stars, the colours given by Martins and Plez (2006) were used for the single M33 star of this type. The uncertainties in $(B-V)_0$ were taken to be those equivalent to misclassification by one spectral subtype or one luminosity class; the formal LGGS photometric errors

are negligibly small by comparison.

5.3.1 Evolved massive stars

$(B-V)_0$ is unknown for four stars, of which three are classified as Luminous Blue Variable (LBV) candidates and one Wolf-Rayet star. These are both classes of bright evolved high-mass stars, which are thought to represent a short-lived heavily mass-losing phase of massive star evolution. A reviews of Wolf-Rayet stars has been presented for by Crowther (2007), whilst Massey (2003) has presented a review of these classes of star in the Local Group.

The single Wolf-Rayet was classified by the author as a WC4 by reference to the criteria given by Crowther et al. (1998). Subsequent investigation of the literature determined that this star was first classified as a Wolf-Rayet by Massey and Johnson (1998), who assigned it as a WC star. Abbott et al. (2004) also obtained a spectrum of this star, and classified it as a WC4.

A search in lists of known LBV stars revealed that the three candidates were among the four bright variable stars found in M33 by Hubble and Sandage (1953), the prototypes of the Hubble-Sandage variables. Hubble and Sandage designated these stars Var A, Var B and Var C; they are amongst the best-studied LBV stars outside the Milky Way (Massey 2003). Our DEIMOS spectra reveal a number of significant variations in the spectra of these stars when compared to other observations a few years apart. Further investigations of these differences are ongoing.

Table 5.2 – Measured spectral types, reddenings and diffuse interstellar band equivalent widths for the stars observed in M33. Uncertainties in the spectral types are one spectral subtype or one luminosity class. $E_{(B-V),\mathrm{M33}}$ assumes a foreground reddening of $E_{(B-V),\mathrm{MW}} = 0.04 \pm 0.02$, see section 5.3.2. Uncertainties are 1σ, upper limits are 3σ.

Star	SpT	$E_{(B-V),\mathrm{M33}}$	λ5780	
			v_{LSR} (km s^{-1})	W (mÅ)
0	B1-2 I	0.15 ± 0.04	-	< 200
1	K0 V	fg	-	-
2	K2-3 V	fg	-	-
3	LBV	-	-	-
4	B I	0.10 ± 0.12	-	< 360
5	B5-8 Ib	*	-91 ± 13	197 ± 17
6	B5 Ib-II	*	-10 ± 48	178 ± 31
7	B3 II-III	*	-80 ± 12	324 ± 19
8	B5 Ia	0.01 ± 0.03	-14 ± 7	67 ± 9
9	B3 Ia	0.13 ± 0.03	-	< 130
10	A0 Ia	-0.01 ± 0.03	$+36 \pm 15$	105 ± 28
11	B1 Ib-II	*	$+7 \pm 21$	182 ± 32
12	A2 Ia	0.03 ± 0.03	-	< 140
13	LBV	-	-	< 110
14	LBV	-	-	< 350
15	B9 Ia	-0.01 ± 0.02	-47 ± 29	66 ± 16
16	B9 Ia	0.00 ± 0.02	-43 ± 14	75 ± 13
17	B3 Ia	0.08 ± 0.03	-	< 80
18	B2 Ia	0.09 ± 0.03	-39 ± 37	82 ± 24
19	WC4	-	-	-
20	B1 Ia	0.03 ± 0.03	-	< 130
21	A3 Ia	-0.04 ± 0.03	-	< 150
22	B8 Ia	0.09 ± 0.03	†	†
23	B8 Ia	-0.01 ± 0.03	-	< 150
24	A0 Ia	0.11 ± 0.02	-189 ± 29	129 ± 36

* unreliable photometry, due to e.g. blends with other sources

† no spectrum at this wavelength due to camera vignetting

Continued...

Table 5.2 continued

Star	SpT	$E_{(B-V),\mathrm{M33}}$	λ5780	
			v_{LSR} (km s^{-1})	W (mÅ)
25	F0 Ia	-0.02 ± 0.02	-98 ± 53	87 ± 27
26	F0 Ia	-0.08 ± 0.03	23 ± 28	117 ± 30
27	B1 Ia	0.06 ± 0.03	-32 ± 17	97 ± 18
28	B5 Ia	0.06 ± 0.03	-30 ± 37	< 300
29	B9 Ia	0.01 ± 0.02	-	< 110
30	B8 Ia	0.00 ± 0.04	-67 ± 26	126 ± 25
31	A3 Ia	0.23 ± 0.03	-124 ± 11	321 ± 41
32	B3 Ia	0.08 ± 0.03	-	< 260
33	F2 Ia	0.03 ± 0.03	-28 ± 10	88 ± 11
35	F2 Ia	-0.03 ± 0.03	-2 ± 14	135 ± 31
36	B1 Ia	0.19 ± 0.03	†	†
37	B2.5 Ia	0.03 ± 0.03	-	< 170
38	B1.5 Ia	0.24 ± 0.02	-96 ± 18	116 ± 25
39	B0.7 Ia	0.08 ± 0.03	-	< 490
40	B2.5 Ia	0.33 ± 0.03	-154 ± 11	114 ± 25
41	O7-8 II(f)	0.17 ± 0.02	-185 ± 11	179 ± 59
42	B5: Ia	0.10 ± 0.03	-	< 240
43	B0.5-1 Ia	0.06 ± 0.03	-	< 270

* unreliable photometry, due to e.g. blends with other sources

† no spectrum at this wavelength due to camera vignetting

5.3.2 Foreground dust

$E_{(B-V)}$ is a measure of the total line-of-sight reddening, which is caused by dust within the Milky Way halo and local ISM as well as M33. Because the radial velocity of M33 is sufficient to Doppler shift the M33 DIBs away from their MW counterparts, the DIB absorption within M33 may be separated and measured independently. The stellar $E_{(B-V)}$ values must therefore be corrected for the foreground MW contribution, in order to obtain a meaningful DIB–$E_{(B-V)}$ relationship.

Determination of foreground reddening is a common task in extragalactic astronomy, but is complicated by the size and proximity of M33. Generally, the most accurate method is to use the maps of foreground reddening derived by Schlegel et al. (1998)

from the infrared dust emission detected by the IRAS and COBE satellites. These maps indicate that the foreground reddening in the direction of M33 is $E_{(B-V),\mathrm{MW}} = 0.042 \pm 0.007$, where the uncertainty is a nominal 16%. However, the Schlegel et al. maps may have been contaminated by dust within M33 itself, which is sufficiently nearby to contribute at potentially non-negligible levels to the far-IR emission detected by IRAS and COBE. The other large galaxies in the Local Group – M31, the LMC and SMC – were each masked out of the Schlegel et al. maps for this reason; M33 is the closest galaxy for which this masking was not performed. This problem is known to affect the more distant (though dustier) galaxy M82 (Johnson et al. 2009). Futhermore, the Schlegel et al. maps have a low angular resolution of 6′.

Prior to the availability of the far-IR dust maps, the standard method for determining extragalactic extinction was that of Burstein and Heiles (1982), who derived their estimates from a combination of faint galaxy counts and H I emission surveys, including a crude correction for variations in the dust-to-gas ratio. Extinction derived from H I data has the advantage that emission from M33 may be kinematically separated from that of the MW, but the disadvantage of being an indirect indicator of dust. The extinction for M33 interpolated from the Burstein and Heiles data, as reported by the NED database*, corresponds to a foreground reddening $E_{(B-V),\mathrm{MW}} = 0.04 \pm 0.01$, essentially identical to the Schlegel et al. value. However, these two methods are known to have zero-points which differ by 0.02 mag.

The Burstein and Heiles maps have a much lower angular resolution than the Schlegel et al. maps (several degrees, set by the scale of the galaxy count surveys), and may be affected by an instrumental zero-point offset in the H I data. These problems may be reduced, at the cost of assuming a constant gas-to-dust ratio, by combining the recent LAB H I survey (Kalberla et al. 2005) with the corrected H I-to-$E_{(B-V)}$ relation of Burstein and Heiles (1978). Data for the relevant LAB survey point for M33 (the LAB survey has an angular resolution of 30′) were obtained† and the total H I column density over the velocity range of the foreground MW gas (-60 to $+50\,\mathrm{km\,s^{-1}}$) was determined to be $N(\mathrm{H\,I}) = 4.3 \times 10^{20}\,\mathrm{cm^{-2}}$. Application of equation 7 of Burstein and Heiles (1978) then results in $E_{(B-V),\mathrm{MW}} = 0.03 \pm 0.01$.

All of the above estimates result in a single estimate of $E_{(B-V)}$ for the whole of M33.

*The NASA/IPAC Extragalactic Database (NED) is operated by the Jet Propulsion Laboratory, California Institute of Technology, under contract with the National Aeronautics and Space Administration

†Data were downloaded from `http://www.astro.uni-bonn.de/~webaiub/english/tools_labsurvey.php`

However, the individual foreground absorption along multiple lines-of-sight distributed across the disk of M33 might not be uniform, particularly as the galaxy covers an area on the sky larger than the full moon. The DEIMOS data do include a direct measure of the amount of foreground MW material along each individual line-of-sight in the form of the Na I D lines. An estimate of the reddening towards each individual target can be derived from the measured column density in the MW component of the observed Na I D profiles, using the relation between these quantities derived by Hobbs (1974, his table 3). The resulting range of foreground reddenings is then $E_{(B-V),\mathrm{MW}} = 0.00$–$0.27$, with most targets in the interval $E_{(B-V),\mathrm{MW}} = 0.04$–$0.14$. These markedly different reddenings are probably unreliable, for the following reasons. The relationship derived by Hobbs was based upon observations of nearby bright stars, mostly in the plain of the Milky Way, which all lie behind diffuse interstellar clouds. The relation between $N(\mathrm{Na\,I})$ and $E_{(B-V)}$ may well not be valid for the substantially hotter medium in the galactic halo. Secondly, in many cases the Na I D lines detected by Hobbs were saturated; in some cases these were supplemented with Na I 3302 Å lines, but in others the column densities used by Hobbs represent lower limits only. Thirdly, there is intrinsic scatter by a factor of about 0.4 dex (1σ) in the relation. Finally, the measured Na I D around $v = 0$ (i.e. the MW contribution) may be contaminated by imperfect subtraction of the strong Na I D night sky emission lines, a possibility which is exacerbated by the faintness of the targets and the low resolution of the DEIMOS spectra.

Considering the differing estimates derived above, the adopted value of the foreground reddening was conservatively taken to be $E_{(B-V),\mathrm{MW}} = 0.04 \pm 0.02$, constant for all targets.

5.4 Diffuse interstellar bands

Many of the diffuse interstellar bands are asymmetric, and most have non-negligible line widths compared to the DEIMOS point spread function. In order to minimise the systematic effects this introduces into measurement of weak or marginally-detected DIBs, it is not sufficient to simply integrate equivalent widths or fit to Gaussian or Voigtian profiles. The method adopted here is to fit the spectra using intrinsic DIB profiles derived from high quality observations of DIBs along a line-of-sight which are dominated by a single interstellar cloud. These profiles are then broadened by the instrumental resolution before being allowed to vary in N and v during the fitting process.

The DIB profiles used were derived from high resolution ($R \sim 58,000$), high signal-

to-noise (S/N> 1,000) observations of the star β^1 Sco, obtained with the UCLES spectrograph on the Anglo Australian Telescope. The development of these model profiles and the efficacy of the technique have been discussed by Cordiner (2006), who found that the method accurately determines the equivalent widths and velocities of DIBs in extragalactic spectra. Small uncertainties of $\sim 1\,\mathrm{km\,s^{-1}}$ are introduced by the full range of DIB profile variations observed within the Milky Way; if extragalactic DIBs have an intrinsically different profile to those seen in the MW then these uncertainties would only constitute lower limits. However, no evidence has ever been found for such large profile variations in extragalactic DIBs, and the error bars reported below are far larger due to the low resolution and signal-to-noise in the DEIMOS spectra.

The resulting equivalent widths for the λ5780 DIB are given in table 5.2, and plotted in figure 5.2. These constitute the first reported measurements of DIBs in the M33 galaxy. The detections are generally at or above the upper limit of λ5780 equivalent widths detected in the Milky Way for a given $E_{(B-V)}$. However, this may be caused by a selection effect, whereby weak DIBs are not detected. The behaviour of DIBs in M33 is certainly unlike that in the Magellanic Clouds (cf. figure 5.1). The uncertainties from the equivalent width measurements are seen to be comparable or less than those from the reddening determination, which are derived partly from uncertainties in the stellar spectral type but mostly in the foreground reddening correction.

One star in the sample (star 31, J013346.96+303642.8) was found to exhibit detectable absorption in far more DIBs than any other. Towards this star, searches were performed for twenty of the (typically) strongest DIBs. The $\lambda\lambda$5705, 5780, 5797, 6203, 6269, 6283 and 6613 DIBs were all detected at a significance $> 2.5\sigma$. λ4428 and λ6196 were tentatively detected at a lower significance. Equivalent widths and velocities for these DIBs are presented in table 5.3, and the spectra are shown in figure 5.3.

Star 31 has a reddening of $E_{(B-V)} = 0.23 \pm 0.03$, making these DIBs amongst the strongest per unit $E_{(B-V)}$ ever detected. The only star with a higher $\lambda 5780/E_{(B-V)}$ ratio is MAG 70817 in the M31 galaxy (Cordiner et al. 2008a). A possible explanation is that star 31 lies close ($\sim 25''$, $\sim 100\,\mathrm{pc}$) to a cluster of UV-bright stars visible in GALEX images of M33. A similar coincidence of nearby UV sources has been noted by the author for stars in M31 with DIB detections (Cordiner et al. submitted). If the DIB carriers require UV radiation for their formation and/or excitation, but are destroyed at very high UV levels, this could explain why the DIBs are so strong towards star 31. Higher resolution and signal-to-noise spectra of this star would be desirable to confirm such strong DIBs and determine the interstellar conditions along the sightline towards

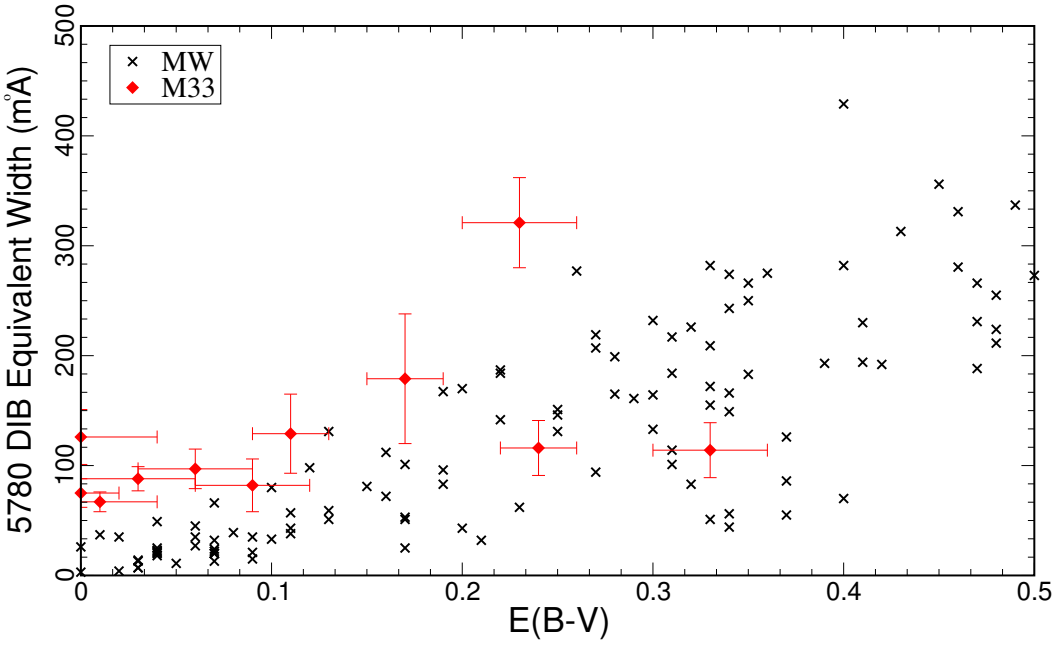

Figure 5.2 – Detections of the λ5780 DIB in M33, plotted against $E_{(B-V)}$. MW data are those from figure 5.1.

DIB	v (km s^{-1})	W (mÅ)
4428	-	< 1550
5705	-143 ± 15	46 ± 18
5780	-130 ± 17	321 ± 41
5797	-142 ± 14	92 ± 22
6196	-	< 31
6203	-155 ± 27	133 ± 28
6269	-120 ± 14	45 ± 18
6283	-144*	524 ± 58
6613	-130 ± 5	137 ± 14

* velocity held fixed during fitting

Table 5.3 – Diffuse interstellar bands detected towards star 31 in M33. Uncertainties are 1σ, whilst upper limits are 3σ.

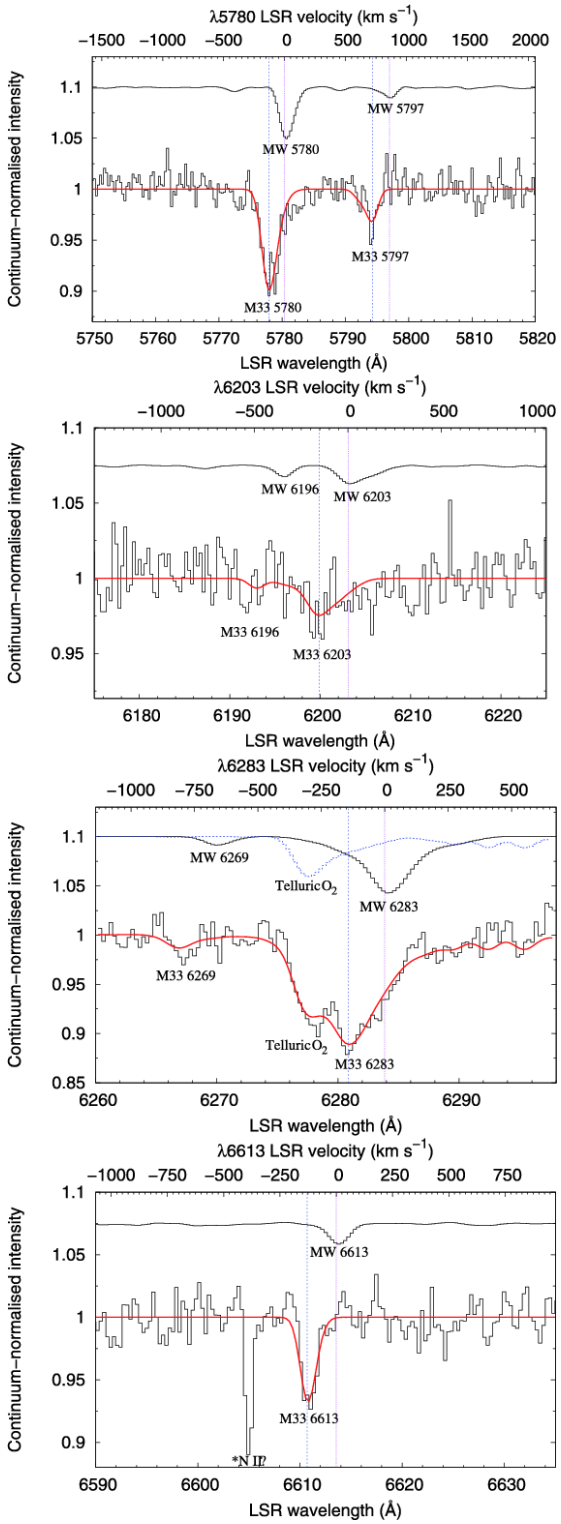

Figure 5.3 – Diffuse interstellar bands detected towards star 31 in M33. Lower black histograms are the observed spectra, whilst red lines are the modelled profiles. The upper black histograms show the DIB profiles observed towards β^1 Sco used in the fitting (from Cordiner 2006). Vertical dotted lines indicate the DIB central wavelengths for absorbers located in the MW and M33. Reproduced with permission from Cordiner et al. (2008b).

star 31.

5.5 Conclusions

Multi-object spectroscopy of forty-three stars located throughout the disc of M33 have been presented, including the first measurements of DIBs in this galaxy. For each star, stellar spectral types and reddenings were determined, including a correction for foreground reddening in the Milky Way. DIB equivalent widths were measured using model profiles derived from a MW standard, and rigorous Monte-Carlo error estimates derived. Firm detections of the λ5780 DIB are made towards 20 stars, although four of these do not have $E_{(B-V)}$ determinations.

The measured DIB equivalent widths in M33 are around the upper end of those observed in the MW for the same degree of reddening. One target (star 31) exhibits extremely strong DIBs per unit $E_{(B-V)}$, and a total of seven DIBs are detected towards this star. However, the low number statistics and high uncertainties prevent definitive conclusions being drawn on the relative behaviour of DIB in M33 and the MW. Nevertheless, there is a clear difference between M33 and the MW on one hand, and the Magellanic Clouds on the other. This may be caused by the differing metallicities of the galaxies. However, metallicity would affect both dust and the gas-phase molecules thought to be responsible for the DIBs. The DIB/$E_{(B-V)}$ ratio may instead be related to the differences in UV field between the galaxies. Further observations are required, both to improved the statistics and distinguish between these possibilities, which are discussed in chapter 6.

Chapter 6

Summary & further work

6.1 Summary

This thesis has presented studies of the interstellar medium which probe scales from 10 AU to 10 kpc. The observations tackle two major problem in ISM research: small-scale structure and the diffuse interstellar bands. The relevant scientific background was introduced in chapter 1, whilst the methods used were detailed in chapter 2.

In chapter 3, ultra-high resolution observations of interstellar absorption towards the star κ Vel were presented. The results show continued increases in atomic equivalent widths since observations ~ 4 yr earlier, as the transverse velocity of the star carried it ≈ 10 AU in a direction perpendicular to the line of sight. The diatomic CH molecule was also detected, whilst only an upper limit was found for the C_2 molecule. Line profile models were fitted to the data, and two main components identified for all species except CH. The line widths were used to place constraints on the kinetic temperature, whilst line ratios were used to derive the electron density (and hence a lower limit to the total number density) and calcium depletion. The results were compared to a chemical model from the literature.

In chapter 4, two studies using DIBs as a probe of small-scale structure were presented. In the first study, medium-resolution observations of DIB absorption towards the two binaries HD 168075/6 & HD 176269/70 and four members of the μ Sgr system were performed. Towards HD 176269/70 no significant DIB absorption was detected. However, significant absorption and variation between sightlines was found for HD 168075/6 and μ Sgr, over scales $\sim$ 50,000–200,000 AU. In the second study, observations of 452 stars in the globular cluster ω Cen were used to trace Na I, Ca II and the $\lambda\lambda$5780 & 5797 DIBs in the galactic disc-halo interface. Significant structure was

detected on scales of around a parsec.

The first detections of diffuse interstellar bands in the M33 galaxy were presented in chapter 5. Multi-object spectroscopy of 43 stars located across the disc of the galaxy were used to derive spectral types and search for DIBs. Model DIB profiles and a shift-and-scale technique were used to measure statistically robust DIB equivalent widths. Combined with photometry from the literature and estimates of the foreground reddening, $E_{(B-V)}$ was determined for almost all stars and the $\lambda 5780/E_{(B-V)}$ ratio measured. The ratio was found to be at the upper end of that observed in the Milky Way, with a possible additive offset. One star has an unusually strong ratio of DIB equivalent width to $E_{(B-V)}$, and a total of seven DIBs were detected towards this star.

6.2 Further work

6.2.1 Small-scale structure

Continued monitoring of the interstellar absorption towards κ Vel would appear to be worthwhile, in order to determine the size of the structure from the time taken for the absorption strength to begin to decline. However, this should be limited to the strong K I, Ca II and perhaps Ca I lines for comparison with previous observations. The difficulty in deriving firm conclusions in chapter 3 indicates the limitations of the available optical observations of atomic lines, whilst further molecular detections appear unlikely. The most promising avenue to increased understanding of the small-scale structure towards this star is UV spectroscopy. In particular, observations of the C I fine structure lines in the near-UV would allow derivation of the local density and kinetic temperature. Although these quantities are partly degenerate via this method, that degeneracy could be lifted via the existing constraints on temperature and density, though (nearly) simultaneous optical observations would be an advantage. A direct measurement of the H_2 fraction would also be beneficial.

The observations presented in chapter 4 clearly demonstrate the efficacy of DIBs as probes of small-scale structure, and the significant savings in telescope time this technique may represent. The next step is to apply this technique to a large sample of binary/multiple systems. This would provide information on the statistical properties, ubiquity and spatial distribution of small-scale structure, and provide identification of promising targets for high-resolution follow-up of atomic and diatomic species. Ultimately, these may provide new insights into the carriers of the DIBs. However, such a project

is clearly a large undertaking, requiring significant lead time, telescope time allocation and collaboration with numerous other investigators.

Further study of DIBs towards star clusters is a promising avenue of research. Whilst suitable globular clusters are rare and their stars faint, nearby open clusters and OB associations make suitable candidate targets. Many have been well studied for other purposes, and some data may already exist from previous observations. New observations of the clusters/associations M35, Aur OB2, h & χ Per and Cas OB6 were obtained by the author as poor-weather backup during a observing run on the 4.2 m William Herschel Telescope (see below). Analysis of these observations is now in progress.

6.2.2 Extragalactic DIBs

In chapter 5, it was concluded that more data was required on DIBs in M33. Follow-up observations have been conducted, with the intention of improving the number statistics. In an attempt to improve the detection rate, all the targets were previously confirmed to be OB stars via literature spectroscopy. Six grey nights were awarded for the project on the 4.2 m William Herschel Telescope during 2009 October; the observers were the author and M Cordiner (NASA GSFC). Thirty-four stars in M33 were observed using the AF2/WYFFOS multi-object spectrograph over the wavelength region 5650–6550 Å, covering most of the strong DIBs. Targets were selected to provide as wide a range of $E_{(B-V)}$ as possible (0–0.8 mag); star 31 was also re-observed to provide independent confirmation of the extremely strong DIBs. Analysis of these data is now under way.

Disentangling *why* the DIBs towards star 31 are so strong requires additional information, in particular high-resolution studies of the atomic and diatomic species along the line of sight. An application for high-resolution observations of star 31 in M33 and MAG 70817 in M31 (these stars have the two highest $5780/E_{(B-V)}$ ratios known) has been submitted. The request was for two nights of bright time on the Keck-I 10 m telescope, with the HIRES spectrograph; time allocations have not yet been announced.

The author has contributed at the co-authorship level to a project measuring DIBs in the M31 galaxy, in a manner similar to chapter 5. Twenty-three hours of service time observations were granted on the Gemini North 8 m telescope with the GMOS-N multi-object spectrograph. Thirty-four stars were observed, DIBs were detected towards 11 of them. The results have been submitted for publication (Cordiner et al. 2010, *Astrophys. J.* submitted).

References

Abbott, J. B., Crowther, P. A., Drissen, L., Dessart, L., Martin, P., and Boivin, G., 2004, *Mon. Not. Roy. Astron. Soc.* **350**, 552

Abt, H. A., 1986, *Astrophys. J.* **304**, 688

Andrews, S. M., Meyer, D. M., and Lauroesch, J. T., 2001, *Astrophys. J. Letters* **552**, L73

Araki, M., Linnartz, H., Kolek, P., Ding, H., Boguslavskiy, A., Denisov, A., Schmidt, T. W., Motylewski, T., Cias, P., and Maier, J. P., 2004, *Astrophys. J.* **616**, 1301

Asplund, M., Grevesse, N., Sauval, A. J., and Scott, P., 2009, *Ann. Rev. Astron. & Astrophys.* **47**, 481

Ball, C. D., McCarthy, M. C., and Thaddeus, P., 2000, *Astrophys. J. Letters* **529**, L61

Ball, D. W., 2006, *Field Guide to Spectroscopy*, SPIE Press

Bell, T. A., Viti, S., Williams, D. A., Crawford, I. A., and Price, R. J., 2005, *Mon. Not. Roy. Astron. Soc.* **357**, 961

Black, J. H. and van Dishoeck, E. F., 1988, *Astrophys. J.* **331**, 986

Bromm, V. and Larson, R. B., 2004, *Ann. Rev. Astron. & Astrophys.* **42**, 79

Burgh, E. B., Nordsieck, K. H., Kobulnicky, H. A., Williams, T. B., O'Donoghue, D., Smith, M. P., and Percival, J. W., 2003, in M. Iye and A. F. M. Moorwood (eds.), *SPIE Conference Series*, Vol. 4841, p. 1463

Burles, S., Nollett, K. M., and Turner, M. S., 2001, *Astrophys. J. Letters* **552**, L1

Burstein, D. and Heiles, C., 1978, *Astrophys. J.* **225**, 40

Burstein, D. and Heiles, C., 1982, *Astron. J.* **87**, 1165

Cannon, A. J. and Pickering, E. C., 1901, *Annals of Harvard College Observatory* **28**, 129

Cardelli, J. A., Clayton, G. C., and Mathis, J. S., 1989, *Astrophys. J.* **345**, 245

Cecchi-Pestellini, C., Williams, D. A., Viti, S., and Casu, S., 2009, *Astrophys. J.* **706**, 1429

Cordiner, M. A., 2006, *Ph.D. thesis*, The University of Nottingham

Cordiner, M. A., Cox, N. L. J., Trundle, C., Evans, C. J., Hunter, I., Przybilla, N., Bresolin, F., and Salama, F., 2008a, *Astron. & Astrophys.* **480**, L13

Cordiner, M. A., Fossey, S. J., Smith, A. M., and Sarre, P. J., 2006, *Faraday Discussions* **133**, 403

Cordiner, M. A. and Sarre, P. J., 2007, *Astron. & Astrophys.* **472**, 537

Cordiner, M. A., Smith, K. T., Cox, N. L. J., Evans, C. J., Hunter, I., Przybilla, N., Bresolin, F., and Sarre, P. J., 2008b, *Astron. & Astrophys.* **492**, L5

Cox, A. N., 2000, *Allen's astrophysical quantities*, Springer, 4th edition

Cox, D. P., 2005, *Ann. Rev. Astron. & Astrophys.* **43**, 337

Cox, N. L. J., Boudin, N., Foing, B. H., Schnerr, R. S., Kaper, L., Neiner, C., Henrichs, H., Donati, J.-F., and Ehrenfreund, P., 2007a, *Astron. & Astrophys.* **465**, 899

Cox, N. L. J., Cordiner, M. A., Cami, J., Foing, B. H., Sarre, P. J., Kaper, L., and Ehrenfreund, P., 2006, *Astron. & Astrophys.* **447**, 991

Cox, N. L. J., Cordiner, M. A., Ehrenfreund, P., Kaper, L., Sarre, P. J., Foing, B. H., Spaans, M., Cami, J., Sofia, U. J., Clayton, G. C., Gordon, K. D., and Salama, F., 2007b, *Astron. & Astrophys.* **470**, 941

Cox, N. L. J. and Patat, F., 2008, *Astron. & Astrophys.* **485**, L9

Crane, P., Lambert, D. L., and Sheffer, Y., 1995, *Astrophys. J. Supplement* **99**, 107

Crawford, I. A., 1991, *Astron. & Astrophys.* **247**, 183

Crawford, I. A., 1995, *Mon. Not. Roy. Astron. Soc.* **277**, 458

Crawford, I. A., 2002, *Mon. Not. Roy. Astron. Soc.* **334**, L33

Crawford, I. A., 2003, *Astrophys. & Space Sci.* **285**, 661

Crawford, I. A., Howarth, I. D., Ryder, S. D., and Stathakis, R. A., 2000, *Mon. Not. Roy. Astron. Soc.* **319**, L1

Crovisier, J., Kazes, I., and Dickey, J. M., 1985, *Astron. & Astrophys.* **146**, 223

Crowther, P. A., 2007, *Ann. Rev. Astron. & Astrophys.* **45**, 177

Crowther, P. A., De Marco, O., and Barlow, M. J., 1998, *Mon. Not. Roy. Astron. Soc.* **296**, 367

Crowther, P. A. and Evans, C. J., 2009, *Astron. & Astrophys.* **503**, 985

Deshpande, A. A., McCulloch, P. M., Radhakrishnan, V., and Anantharamaiah, K. R., 1992, *Mon. Not. Roy. Astron. Soc.* **258**, 19P

Diamond, P. J., Goss, W. M., Romney, J. D., Booth, R. S., Kalberla, P. M. W., and Mebold, U., 1989, *Astrophys. J.* **347**, 302

Dickey, J. M. and Lockman, F. J., 1990, *Ann. Rev. Astron. & Astrophys.* **28**, 215

Diego, F., Fish, A. C., Barlow, M. J., Crawford, I. A., Spyromilio, J., Dryburgh, M., Brooks, D., Howarth, I. D., and Walker, D. D., 1995, *Mon. Not. Roy. Astron. Soc.* **272**, 323

Dieter, N. H., Welch, W. J., and Romney, J. D., 1976, *Astrophys. J. Letters* **206**, L113

Dommanget, J. and Nys, O., 2000, *Astron. & Astrophys.* **363**, 991

Draine, B. T., 2003, *Ann. Rev. Astron. & Astrophys.* **41**, 241

Ducourant, C., Teixeira, R., Périé, J. P., Lecampion, J. F., Guibert, J., and Sartori, M. J., 2005, *Astron. & Astrophys.* **438**, 769

Dufton, P. L., Smartt, S. J., Lee, J. K., et al., 2006, *Astron. & Astrophys.* **457**, 265

Dunkin, S. K. and Crawford, I. A., 1999, *Mon. Not. Roy. Astron. Soc.* **302**, 197

Ehrenfreund, P., Cami, J., Jiménez-Vicente, J., Foing, B. H., Kaper, L., van der Meer, A., Cox, N., D'Hendecourt, L., Maier, J. P., Salama, F., Sarre, P. J., Snow, T. P., and Sonnentrucker, P., 2002, *Astrophys. J. Letters* **576**, L117

Ellison, S. L., York, B. A., Murphy, M. T., Zych, B. J., Smith, A. M., and Sarre, P. J., 2008, *Mon. Not. Roy. Astron. Soc.* **383**, L30

ESA (ed.), 1997, *The HIPPARCOS and TYCHO catalogues. Astrometric and photometric star catalogues derived from the ESA HIPPARCOS Space Astrometry Mission*, Vol. 1200 of *ESA Special Publications*, European Space Agency

Evans, C. J. and Howarth, I. D., 2003, *Mon. Not. Roy. Astron. Soc.* **345**, 1223

Evans, C. J., Howarth, I. D., Irwin, M. J., Burnley, A. W., and Harries, T. J., 2004, *Mon. Not. Roy. Astron. Soc.* **353**, 601

Evans, C. J., Smartt, S. J., Lee, J.-K., et al., 2005, *Astron. & Astrophys.* **437**, 467

Field, G. B., Goldsmith, D. W., and Habing, H. J., 1969, *Astrophys. J. Letters* **155**, L149

Fitzgerald, M. P., 1970, *Astron. & Astrophys.* **4**, 234

Flower, D., 2007, *Molecular Collisions in the Interstellar Medium*, No. 42 in Cambridge Astrophysics Series, Cambridge University Press, 2nd edition

Foing, B. H. and Ehrenfreund, P., 1994, *Nature* **369**, 296

Fossey, S. J., 1991, *Nature* **353**, 393

Frail, D. A., Cordes, J. M., Hankins, T. H., and Weisberg, J. M., 1991, *Astrophys. J.* **382**, 168

Frail, D. A., Weisberg, J. M., Cordes, J. M., and Mathers, C., 1994, *Astrophys. J.* **436**, 144

Fuchs, B., Breitschwerdt, D., de Avillez, M. A., and Dettbarn, C., 2009, *Space Sci. Reviews* **143**, 437

Fulara, J. and Krełowski, J., 2000, *New Astronomy Review* **44**, 581

Galazutdinov, G., Moutou, C., Musaev, F., and Krełowski, J., 2002, *Astron. & Astrophys.* **384**, 215

Galazutdinov, G. A. and Krełowski, J., 2006, *Astrophys. J.* **637**, 342

Galazutdinov, G. A., Krełowski, J., Musaev, F. A., Ehrenfreund, P., and Foing, B. H., 2000, *Mon. Not. Roy. Astron. Soc.* **317**, 750

Galazutdinov, G. A., LoCurto, G., and Krełowski, J., 2008, *Astrophys. J.* **682**, 1076

Hartquist, T. W., Falle, S. A. E. G., and Williams, D. A., 2003, *Astrophys. & Space Sci.* **288**, 369

Hearnshaw, J. B., 1986, *The analysis of starlight: One hundred and fifty years of astronomical spectroscopy*, Cambridge University Press

Heckman, T. M. and Lehnert, M. D., 2000, *Astrophys. J.* **537**, 690

Heger, M. L., 1922, *Lick Observatory Bulletin* **10**, 141

Heiles, C., 1997, *Astrophys. J.* **481**, 193

Heiles, C., 2007, in M. Haverkorn & W. M. Goss (ed.), *SINS - Small Ionized and Neutral Structures in the Diffuse Interstellar Medium*, Vol. 365 of *Astronomical Society of the Pacific Conference Series*, p. 3

Heiles, C. and Stinebring, D., 2007, in M. Haverkorn and W. M. Goss (eds.), *SINS - Small Ionized and Neutral Structures in the Diffuse Interstellar Medium*, Vol. 365 of *Astronomical Society of the Pacific Conference Series*, p. 331

Heiles, C. and Troland, T. H., 2003, *Astrophys. J.* **586**, 1067

Herbig, G. H., 1963, *Astrophys. J.* **137**, 200

Herbig, G. H., 1975, *Astrophys. J.* **196**, 129

Herbig, G. H., 1993, *Astrophys. J.* **407**, 142

Herbig, G. H., 1995, *Ann. Rev. Astron. & Astrophys.* **33**, 19

Hillenbrand, L. A., Massey, P., Strom, S. E., and Merrill, K. M., 1993, *Astron. J.* **106**, 1906

Hinshaw, G., Weiland, J. L., Hill, R. S., Odegard, N., Larson, D., Bennett, C. L., Dunkley, J., Gold, B., Greason, M. R., Jarosik, N., Komatsu, E., Nolta, M. R., Page, L., Spergel, D. N., Wollack, E., Halpern, M., Kogut, A., Limon, M., Meyer, S. S., Tucker, G. S., and Wright, E. L., 2009, *Astrophys. J. Supplement* **180**, 225

Hirata, S., Head-Gordon, M., Szczepanski, J., and Vala, M., 2003, *J. Phys. Chem. A* **107**, 4940

Hobbs, L. M., 1974, *Astrophys. J.* **191**, 381

Hobbs, L. M., Ferlet, R., Welty, D. E., and Wallerstein, G., 1991, *Astrophys. J.* **378**, 586

Hobbs, L. M., Wallerstein, G., and Huu, E. M., 1982, *Astrophys. J. Letters* **252**, L17

Hobbs, L. M., York, D. G., Snow, T. P., Oka, T., Thorburn, J. A., Bishof, M., Friedman, S. D., McCall, B. J., Rachford, B., Sonnentrucker, P., and Welty, D. E., 2008, *Astrophys. J.* **680**, 1256

Hobbs, L. M., York, D. G., Thorburn, J. A., Snow, T. P., Bishof, M., Friedman, S. D., Mc Call, B. J., Oka, T., Rachford, B., Sonnentrucker, P., and Welty, D. E., 2009, *Astrophys. J.* **705**, 32

Høg, E., Fabricius, C., Makarov, V. V., Urban, S., Corbin, T., Wycoff, G., Bastian, U., Schwekendiek, P., and Wicenec, A., 2000, *Astron. & Astrophys.* **355**, L27

Houk, N., 1982, *Michigan Catalogue of Two-dimensional Spectral Types for the HD stars*, Vol. 3: Declinations -40° to -26°, University of Michigan Press

Howarth, I. D., Price, R. J., Crawford, I. A., and Hawkins, I., 2002, *Mon. Not. Roy. Astron. Soc.* **335**, 267

Hubble, E. and Sandage, A., 1953, *Astrophys. J.* **118**, 353

Hutchings, J. B., 1964, *Nature* **202**, 992

Hutchings, J. B., 1966, *Mon. Not. Roy. Astron. Soc.* **131**, 299

Iglesias-Groth, S., 2007, *Astrophys. J. Letters* **661**, L167

Indriolo, N., Oka, T., Geballe, T. R., and McCall, B. J., 2010, *Astrophys. J.* **711**, 1338

Jenkins, E. B., 2009, *Astrophys. J.* **700**, 1299

Jenniskens, P., Mulas, G., Porceddu, I., and Benvenuti, P., 1997, *Astron. & Astrophys.* **327**, 337

Jochnowitz, E. B. and Maier, J. P., 2008, in S. Kwok & S. Sandford (ed.), *Organic Matter in Space*, Vol. 251 of *IAU Symposiums*, p. 395

Johnson, L. C., Méndez, R. H., and Teodorescu, A. M., 2009, *Astrophys. J.* **697**, 1138

Kalberla, P. M. W., Burton, W. B., Hartmann, D., Arnal, E. M., Bajaja, E., Morras, R., and Pöppel, W. G. L., 2005, *Astron. & Astrophys.* **440**, 775

Kalberla, P. M. W. and Kerp, J., 2009, *Ann. Rev. Astron. & Astrophys.* **47**, 27

Kemp, S. N., Bates, B., and Lyons, M. A., 1993, *Astron. & Astrophys.* **278**, 542

Kendall, T. R., Mauron, N., McCombie, J., and Sarre, P. J., 2002, *Astron. & Astrophys.* **387**, 624

Kerr, T. H., Hibbins, R. E., Fossey, S. J., Miles, J. R., and Sarre, P. J., 1998, *Astrophys. J.* **495**, 941

Kerr, T. H., Hibbins, R. E., Miles, J. R., Fossey, S. J., Somerville, W. B., and Sarre, P. J., 1996, *Mon. Not. Roy. Astron. Soc.* **283**, L105

Kiss, L. L., Thomson, J. R., Ogloza, W., Furész, G., and Sziládi, K., 2001, *Astron. & Astrophys.* **366**, 858

Kitchin, C. R., 2009, *Astrophysical Techniques*, CRC Press, 5th edition

Kobulnicky, H. A., Nordsieck, K. H., Burgh, E. B., Smith, M. P., Percival, J. W., Williams, T. B., and O'Donoghue, D., 2003, in M. Iye and A. F. M. Moorwood (eds.), *SPIE Conference Series*, Vol. 4841, p. 1634

Krełowski, J., Ehrenfreund, P., Foing, B. H., Snow, T. P., Weselak, T., Tuairisg, S. Ó., Galazutdinov, G. A., and Musaev, F. A., 1999, *Astron. & Astrophys.* **347**, 235

Krełowski, J. and Sneden, C., 1995, in A. G. G. M. Tielens and T. P. Snow (eds.), *The Diffuse Interstellar Bands*, Vol. 202 of *Astrophysics and Space Science Library*, p. 13

Krełowski, J., Snow, T. P., Papaj, J., Seab, C. G., and Wszolek, B., 1993, *Astrophys. J.* **419**, 692

Krełowski, J., Snow, T. P., Seab, C. G., and Papaj, J., 1992, *Mon. Not. Roy. Astron. Soc.* **258**, 693

Krełowski, J. and Walker, G. A. H., 1987, *Astrophys. J.* **312**, 860

Kroto, H. W., Heath, J. R., Obrien, S. C., Curl, R. F., and Smalley, R. E., 1985, *Nature* **318**, 162

Kroto, H. W. and Jura, M., 1992, *Astron. & Astrophys.* **263**, 275

Lallement, R., Welsh, B. Y., Vergely, J. L., Crifo, F., and Sfeir, D., 2003, *Astron. & Astrophys.* **411**, 447

Lambert, D. L. and Danks, A. C., 1986, *Astrophys. J.* **303**, 401

Langer, G. E., Prosser, C. F., and Sneden, C., 1990, *Astron. J.* **100**, 216

Lauroesch, J. T., 2007, in M. Haverkorn & W. M. Goss (ed.), *SINS - Small Ionized and Neutral Structures in the Diffuse Interstellar Medium*, Vol. 365 of *Astronomical Society of the Pacific Conference Series*, p. 40

Lawton, B., Churchill, C. W., York, B. A., Ellison, S. L., Snow, T. P., Johnson, R. A., Ryan, S. G., and Benn, C. R., 2008, *Astron. J.* **136**, 994

Lazio, T. J. W., Brogan, C. L., Goss, W. M., and Stanimirović, S., 2009, *Astron. J.* **137**, 4526

Le Bertre, T. and Lequeux, J., 1992, *Astron. & Astrophys.* **255**, 288

Le Page, V., Snow, T. P., and Bierbaum, V. M., 2003, *Astrophys. J.* **584**, 316

Léger, A. and d'Hendecourt, L., 1985, *Astron. & Astrophys.* **146**, 81

Léger, A. and Puget, J. L., 1984, *Astron. & Astrophys.* **137**, L5

Leone, F. and Lanzafame, A. C., 1997, *Astron. & Astrophys.* **320**, 893

Lequeux, J., 2005, *The Interstellar Medium*, Astronomy & Astrophysics Library, Springer

Lindroos, K. P., 1985, *Astron. & Astrophys. Supplement* **60**, 183

Linnartz, H., Wehres, N., van Winckel, H., Walker, G. A. H., Bohlender, D. A., Tielens, A. G. G. M., Motylewski, T., and Maier, J. P., 2010, *Astron. & Astrophys.* **511**, L3

Liszt, H., 2003, *Astron. & Astrophys.* **398**, 621

Lodders, K., 2003, *Astrophys. J.* **591**, 1220

Luna, R., Cox, N. L. J., Satorre, M. A., García Hernández, D. A., Suárez, O., and García Lario, P., 2008, *Astron. & Astrophys.* **480**, 133

Maier, J. P., 1994, *Nature* **370**, 423

Maier, J. P., Walker, G. A. H., and Bohlender, D. A., 2004, *Astrophys. J.* **602**, 286

Malloci, G., Mulas, G., and Benvenuti, P., 2003, *Astron. & Astrophys.* **410**, 623

Martins, F. and Plez, B., 2006, *Astron. & Astrophys.* **457**, 637

Mason, B. D., Wycoff, G. L., Hartkopf, W. I., Douglass, G. G., and Worley, C. E., 2001, *Astron. J.* **122**, 3466

Massey, P., 2003, *Ann. Rev. Astron. & Astrophys.* **41**, 15

Massey, P. and Johnson, O., 1998, *Astrophys. J.* **505**, 793

Massey, P., Olsen, K. A. G., Hodge, P. W., Strong, S. B., Jacoby, G. H., Schlingman, W., and Smith, R. C., 2006, *Astron. J.* **131**, 2478

Mauron, N. and Kendall, T. R., 2004, *Astron. & Astrophys.* **428**, 535

McCall, B. J., Drosback, M. M., Thorburn, J. A., York, D. G., Friedman, S. D., Hobbs, L. M., Rachford, B. L., Snow, T. P., Sonnentrucker, P., and Welty, D. E., 2010, *Astrophys. J.* **708**, 1628

McCall, B. J., Thorburn, J., Hobbs, L. M., Oka, T., and York, D. G., 2001, *Astrophys. J. Letters* **559**, L49

McDonald, I., van Loon, J. T., Decin, L., Boyer, M. L., Dupree, A. K., Evans, A., Gehrz, R. D., and Woodward, C. E., 2009, *Mon. Not. Roy. Astron. Soc.* **394**, 831

McKee, C. F. and Ostriker, J. P., 1977, *Astrophys. J.* **218**, 148

Megier, A., Krełowski, J., and Weselak, T., 2005, *Mon. Not. Roy. Astron. Soc.* **358**, 563

Melioli, C., Brighenti, F., D'Ercole, A., and de Gouveia Dal Pino, E. M., 2008, *Mon. Not. Roy. Astron. Soc.* **388**, 573

Merrill, P. W., 1930, *Astrophys. J.* **72**, 98

Merrill, P. W., 1934, *Pub. Astron. Soc. Pacific* **46**, 206

Merrill, P. W., 1936, *Astrophys. J.* **83**, 126

Merrill, P. W. and Wilson, O. C., 1938, *Astrophys. J.* **87**, 9

Meyer, D. M., 1990, *Astrophys. J. Letters* **364**, L5

Meyer, D. M. and Blades, J. C., 1996, *Astrophys. J. Letters* **464**, L179

Meyer, D. M. and Lauroesch, J. T., 1999, *Astrophys. J. Letters* **520**, L103

Misawa, T., Gandhi, P., Hida, A., Tamagawa, T., and Yamaguchi, T., 2009, *Astrophys. J.* **700**, 1988

Morton, D. C., 2003, *Astrophys. J. Supplement* **149**, 205

Morton, D. C., 2004, *Astrophys. J. Supplement* **151**, 403

Moutou, C., Krełowski, J., D'Hendecourt, L., and Jamroszczak, J., 1999, *Astron. & Astrophys.* **351**, 680

Munari, U., Tomasella, L., Fiorucci, M., Bienaymé, O., Binney, J., Bland-Hawthorn, J., Boeche, C., Campbell, R., Freeman, K. C., Gibson, B., Gilmore, G., Grebel, E. K., Helmi, A., Navarro, J. F., Parker, Q. A., Seabroke, G. M., Siebert, A., Siviero, A., Steinmetz, M., Watson, F. G., Williams, M., Wyse, R. F. G., and Zwitter, T., 2008, *Astron. & Astrophys.* **488**, 969

Munari, U. and Zwitter, T., 1997, *Astron. & Astrophys.* **318**, 269

Newton, I., 1687, *Philosophiæ Naturalis Principia Mathematica*, Royal Society of London, English translation by Motte, A., 1729

Pathak, A. and Sarre, P. J., 2008, *Mon. Not. Roy. Astron. Soc.* **391**, L10

Pequignot, D. and Aldrovandi, S. M. V., 1986, *Astron. & Astrophys.* **161**, 169

Pettini, M. and Dodorico, S., 1986, *Astrophys. J.* **310**, 700

Points, S. D., Lauroesch, J. T., and Meyer, D. M., 2004, *Pub. Astron. Soc. Pacific* **116**, 801

Pourbaix, D., Tokovinin, A. A., Batten, A. H., Fekel, F. C., Hartkopf, W. I., Levato, H., Morrell, N. I., Torres, G., and Udry, S., 2004, *Astron. & Astrophys.* **424**, 727

Price, R. J., Crawford, I. A., and Barlow, M. J., 2000, *Mon. Not. Roy. Astron. Soc.* **312**, L43

Rao, N. K. and Lambert, D. L., 1993, *Mon. Not. Roy. Astron. Soc.* **263**, L27

Ray, T. P., 1989, *Nature* **337**, 343

Rich, R. M., 1987, *Astron. J.* **94**, 651

Sana, H., Gosset, E., and Evans, C. J., 2009, *Mon. Not. Roy. Astron. Soc.* **400**, 1479

Sarre, P. J., 1991, *Nature* **351**, 356

Sarre, P. J., 2000, *Mon. Not. Roy. Astron. Soc.* **313**, L14

Sarre, P. J., 2006, *J. Molecular Spectroscopy* **238**, 1

Sarre, P. J., Miles, J. R., Kerr, T. H., Hibbins, R. E., Fossey, S. J., and Somerville, W. B., 1995a, *Mon. Not. Roy. Astron. Soc.* **277**, L41

Sarre, P. J., Miles, J. R., and Scarrott, S. M., 1995b, *Science* **269**, 674

Saunders, W., Bridges, T., Gillingham, P., Haynes, R., Smith, G. A., Whittard, J. D., Churilov, V., Lankshear, A., Croom, S., Jones, D., and Boshuizen, C., 2004, in A. F. M. Moorwood and M. Iye (eds.), *SPIE Conference Series*, Vol. 5492, p. 389

Schlegel, D. J., Finkbeiner, D. P., and Davis, M., 1998, *Astrophys. J.* **500**, 525

Sharp, R., Saunders, W., Smith, G., Churilov, V., Correll, D., Dawson, J., Farrel, T., Frost, G., Haynes, R., Heald, R., Lankshear, A., Mayfield, D., Waller, L., and Whittard, D., 2006, in *SPIE Conference Series*, Vol. 6269

Słyk, K., Galazutdinov, G. A., Musaev, F. A., Bondar, A. V., Schmidt, M. R., and Krełowski, J., 2006, *Astron. & Astrophys.* **448**, 221

Snow, T. P., 2002, in R. Ferlet, M. Lemoine, J.-M. Désert, and B. Raban (eds.), *17th IAP Colloquium: Gaseous Matter in Galaxies and Intergalactic Space*, p. 63

Snow, T. P. and McCall, B. J., 2006, *Ann. Rev. Astron. & Astrophys.* **44**, 367

Sofia, U. J., Cardelli, J. A., Guerin, K. P., and Meyer, D. M., 1997, *Astrophys. J. Letters* **482**, L105+

Sollerman, J., Cox, N., Mattila, S., Ehrenfreund, P., Kaper, L., Leibundgut, B., and Lundqvist, P., 2005, *Astron. & Astrophys.* **429**, 559

Teixeira, R., Ducourant, C., Sartori, M. J., Camargo, J. I. B., Périé, J. P., Lépine, J. R. D., and Benevides-Soares, P., 2000, *Astron. & Astrophys.* **361**, 1143

Thöne, C. C., Michałowski, M. J., Leloudas, G., Cox, N. L. J., Fynbo, J. P. U., Sollerman, J., Hjorth, J., and Vreeswijk, P. M., 2009, *Astrophys. J.* **698**, 1307

Thorburn, J. A., Hobbs, L. M., McCall, B. J., Oka, T., Welty, D. E., Friedman, S. D., Snow, T. P., Sonnentrucker, P., and York, D. G., 2003, *Astrophys. J.* **584**, 339

Tielens, A. G. G. M., 2005, *The Physics and Chemistry of the Interstellar Medium*, Cambridge University Press

Tielens, A. G. G. M., 2008, *Ann. Rev. Astron. & Astrophys.* **46**, 289

Tulej, M., Kirkwood, D. A., Pachkov, M., and Maier, J. P., 1998, *Astrophys. J. Letters* **506**, L69

van de Ven, G., van den Bosch, R. C. E., Verolme, E. K., and de Zeeuw, P. T., 2006, *Astron. & Astrophys.* **445**, 513

van Dishoeck, E. F. and Black, J. H., 1989, *Astrophys. J.* **340**, 273

van Dishoeck, E. F. and de Zeeuw, T., 1984, *Mon. Not. Roy. Astron. Soc.* **206**, 383

van Leeuwen, F., Le Poole, R. S., Reijns, R. A., Freeman, K. C., and de Zeeuw, P. T., 2000, *Astron. & Astrophys.* **360**, 472

van Loon, J. T., Smith, K. T., McDonald, I., Sarre, P. J., Fossey, S. J., and Sharp, R. G., 2009, *Mon. Not. Roy. Astron. Soc.* **399**, 195

van Winckel, H., Cohen, M., and Gull, T. R., 2002, *Astron. & Astrophys.* **390**, 147

Vazquez-Semadeni, E., 2009, in *The Role of Disk-Halo Interaction in Galaxy Evolution: Outflow vs Infall?*, EAS Publication Series, in press, arXiv:0902.0820

Vladilo, G., Crivellari, L., Molaro, P., and Beckman, J. E., 1987, *Astron. & Astrophys.* **182**, L59

Walker, G. A. H., 1963, *Mon. Not. Roy. Astron. Soc.* **125**, 141

Watson, J. K. and Meyer, D. M., 1996, *Astrophys. J. Letters* **473**, L127

Welsh, B. Y. and Shelton, R. L., 2009, *Astrophys. & Space Sci.* **323**, 1

Welty, D. E., 2007, *Astrophys. J.* **668**, 1012

Welty, D. E., Federman, S. R., Gredel, R., Thorburn, J. A., and Lambert, D. L., 2006, *Astrophys. J. Supplement* **165**, 138

Welty, D. E. and Hobbs, L. M., 2001, *Astrophys. J. Supplement* **133**, 345

Welty, D. E., Hobbs, L. M., and Kulkarni, V. P., 1994, *Astrophys. J.* **436**, 152

Welty, D. E., Hobbs, L. M., and Morton, D. C., 2003, *Astrophys. J. Supplement* **147**, 61

Wolfire, M. G., Hollenbach, D., McKee, C. F., Tielens, A. G. G. M., and Bakes, E. L. O., 1995, *Astrophys. J.* **443**, 152

York, B. A., Ellison, S. L., Lawton, B., Churchill, C. W., Snow, T. P., Johnson, R. A., and Ryan, S. G., 2006, *Astrophys. J. Letters* **647**, L29

Zhou, Z., Sfeir, M. Y., Zhang, L., Hybertsen, M. S., Steigerwald, M., and Brus, L., 2006, *Astrophys. J. Letters* **638**, L105

List of Figures

List of Tables

List of Abbreviations

AU	Astronomical unit
CCD	Charge-coupled device
CNM	Cold neutral medium
DIB	Diffuse interstellar band
DEIMOS	Deep Imaging Multi-Object Spectrograph
DLA	Damped Lyman-α
$E_{(B-V)}$	Differential interstellar reddening between the B and V bands
EW	Equivalent width
FWHM	Full width at half maximum
IRAF	Image Reduction and Analysis Facility
ISRF	Interstellar radiation field
LBV	Luminous Blue Variable
LGGS	Local Group Galaxies Survey
LMC	Large Magellanic Cloud
KW group	Krełowski & Walker group, see section 1.2.1
MW	Milky Way
PAH	Polycyclic aromatic hydrocarbon
pc	Parsec
QSO	Quasi-stellar object
RSS	Robert Stobie Spectrograph
SMC	Small Magellanic Cloud
SSS	Small-scale [interstellar] structure
UHRF	Ultra-High Resolution Facility
UIR	Unidentified infrared
UV	Ultraviolet
VPH	Volume-phase holographic